

**Bipolar Electrodeposition of Bimetallic Alloy (Au-Ag) Gradient: Formation,  
Characterization and Application**

by

Apu Mazumder

A thesis submitted to the Graduate Faculty of  
Auburn University  
in partial fulfillment of the  
requirements for the Degree of  
Master of Science

Auburn, Alabama  
December 10, 2016

Keywords: Bipolar electrochemistry, Surface enhanced raman scattering, Alloy gradient

Copyright 2016 by Apu Mazumder

Approved by

Curtis G. Shannon, Chair, Professor of Chemistry and Biochemistry  
Rik Blumenthal, Associate Professor of Chemistry and Biochemistry  
Christopher J. Easley, Associate Professor of Chemistry and Biochemistry

## Abstract

Bipolar electrochemistry is an attention-grabbing conception for high throughput screening practices due to the capability to make gradients in a variety of materials and their properties, such as composition, particle size, or dopant levels, among many others. The main key advantages of the method are the ability to test, create or modify materials without the need for a direct electrical connection. This whole work is based on bipolar electrochemistry.

In this thesis, my first chapter described an introduction of electrodeposition processes. The basic principles of bipolar electrochemistry are also presented in this chapter. The formation of metal gradients and its application also included in this chapter.

Chapter 2 describes the characterization of Au-Ag alloy gradient formed by bipolar electrodeposition on a stainless steel bipolar electrode, using SEM/EDX and its screening for the electrocatalytic activity towards 4-nitrothiophenol (4-NTP) reduction using Raman spectroelectrochemistry.

Chapter 3 contains the synthesis of one and two dimensional Au-Ag alloy gradients using bipolar electrodeposition method. The alloy gradients were characterized using SEM/EDX. Confocal Raman microscopy was employed to determine the optimum alloy composition that resulted in the maximum surface enhanced Raman scattering (SERS) intensity.

Chapter 4 is the summary of my research work.

## Acknowledgments

I would first like to thank my thesis advisor, Dr. Curtis Shannon. The door to Professor Shannon's office was always open whenever I ran into a trouble spot or had a question about my research or writing. He consistently allowed this paper to be my own work, but steered me in the right the direction whenever he thought I needed it. I would also like to express my sincere gratitude to my supervisory committee members, Dr. Rik Blumenthal and Dr. Christopher Easley for the very useful and important suggestions that made my research successful.

I thank to my fellow lab mates in Shannon's group: Songyan Yu, Buhua Wang and MD Akteruzzaman for the stimulating discussions we have had in the last few years. My special thanks to my former lab mates Sanjun Fan, Li Zhang and all my graduate friends in department of chemistry and biochemistry at Auburn university. In particular, I am grateful to Dr. Axline Ndzesse Sanghapi for enlightening me with my first glance of research.

My son, Swapnil Arnab Paul. All of my life's troubles simply disappear when I see his cute smile. I want to thank him for being the reason for my existence. I would like to thank my family: my mom, dad and to my elder brother, Dr. Anupam Mazumder for supporting me spiritually throughout writing this thesis and my life in general.

I must express my very intense gratitude to my dear husband, Dr. Samir Chandra Paul for providing me with unfailing support and continuous encouragement throughout my years of study and through the process of researching and writing this thesis. This accomplishment would not have been possible without him. Thank you.

## Table of Contents

Abstract.....	ii
Acknowledgement.....	iii
List of Tables.....	vii
List of Schemes.....	viii
List of Figures.....	ix
Chapter 1 Introduction and Background.....	1
1.1. Electrodeposition.....	1
1.2. Electrochemically generated gradients.....	2
1.2.1 Applications of Electrochemically Fabricated Gradients.....	7
1.3. Bipolar Electrochemistry .....	8
1.4. Raman Spectroscopy .....	15
1.4.1 Surface Enhanced Raman Scattering (SERS).....	16
1.4.1.1 Electromagnetic Enhancement.....	18
1.4.1.2 Chemical Enhancement.....	18
1.4.2 Substrate related issues of SERS.....	19
1.5 Surface Enhanced Raman Scattering in catalysis.....	21

1.5.1 4-NTP reduction mechanisms.....	22
References.....	28
Chapter 2 Bipolar electrodeposition of Au-Ag alloy gradient and screening of its electrocatalytic property using Surface Enhanced Raman spectroelectrochemistry.....	35
2.1 Introduction.....	36
2.2 Materials and Methods.....	39
2.3 Characterization of the Au-Ag alloy electrodeposit.....	41
2.3.1 Scanning Electron Microscopy (SEM) and Energy Dispersive X-ray spectroscopy (EDX).....	41
2.3.2 Raman spectroscopy.....	41
2.4 Results and Discussion.....	45
2.4.1 Screening the Au-Ag alloy gradients on the bipolar electrode.....	45
2.4.2 Raman and SERS assignments of 4-nitrothiophenol (4-NTP) and 4-aminothiophenol (4-ATP) .....	47
2.4.3 In situ monitoring of catalytic chemical reduction with SERS.....	51
2.4.4 In situ monitoring of electrochemical catalytic reduction with SERS.....	54
2.4.5 Evaluation of Reaction Gradients on Bipolar Electrodes Using SERS.....	56
2.5 Conclusion.....	68
References.....	69
Chapter 3 Bipolar electrodeposition of one and two dimensional Au-Ag alloy gradients and	

characterization by Surface Enhanced Raman Spectroscopy.....	72
3.1 Introduction.....	73
3.2 Experimental.....	77
3.2.1 Materials.....	77
3.2.2 Substrate Preparation.....	77
3.2.3 Bipolar Electrochemistry.....	78
3.2.4 Formation of Benzene Thiol Self-Assembled Monolayers.....	78
3.2.5 Scanning Electron Microscopy (SEM) and Energy Dispersive X-ray spectroscopy (EDX).....	78
3.2.6 Raman spectroscopy.....	78
3.3 Results and Discussion.....	79
3.3.1 Au-Ag alloy gradient by bipolar electrodeposition.....	79
3.3.2 Scanning Electron Microscopy (SEM) and Energy Dispersive X-ray spectroscopy (EDX).....	81
3.3.3. Characterization of Ag-Au alloy gradient using SERS.....	83
3.4 Conclusions.....	86
References.....	88
Chapter 4 Summary of Thesis.....	90

## List of Tables

Table 2.1: The SERS and ordinary Raman shifts of 4-NTP and 4-ATP and their assignments.....46

Table 3.1: SERS assignments of benzene thiol.....84

## List of Schemes

Scheme 2.1: 4-nitrothiophenol (4-NTP), 4-aminothiophenol (4-ATP), 4,4'-dimercaptoazobenzene (4,4'-DMAB) .....	39
---	----

## List of Figures

Figure 1.1: a) Creation of gradients by using a gradient in light intensity. b) Examples of patterned substrates prepared by illuminating NVOC-protected hydroquinone through microfiche gradient mask.....	4
Figure 1.2: a) Creation of electrochemical gradients by the use of an asymmetric electrode configuration, b) Contour plot of the gradient of pore size and c (RGDfK) density.....	6
Figure 1.3: a) Creation, at a bipolar electrodeposition cell, b) Diagram of the geometry used for AES and Raman analysis.....	6
Figure 1.4: Schematic of the bipolar system. E indicates the direction of the applied external electric field.....	10
Figure 1.5: a) Equivalent circuit and b) simplified representations of a bipolar system. c) and d) represent the potential and electric field profiles across the cell, and e) represents a typical current density profile across the bipolar electrode.....	12
Figure 1.6: Photographs of three different conducting polymers that have been doped in a gradient manner using bipolar electrochemistry.....	14
Figure 1.7: Energy-level diagram showing the states involved in Raman signal. Rayleigh scattering (no exchange of energy), Stokes Raman scattering (atom or molecule absorbs energy), Anti-Stokes Raman scattering (atom or molecule loses energy) .....	16
Figure 1.8: Typical energy level diagram for a molecule adsorbed on a metal surface. The occupied and unoccupied molecular orbital are broadened into resonances by their interaction with the metal states; orbital occupancy is determined by the Fermi energy. Possible charge transfer excitations are shown .....	19
Figure 1.9: Chemical reduction of 4-NTP to 4-ATP.....	24
Figure 1.10: Various reduction mechanisms. a) Photo-catalytic reduction through direct photonic excitation of the reactant molecule into the reactive excited state. b) Electrochemical reduction through increase in electrode potential and subsequent charge-transfer into the reactive excited state of the adsorbed reactant. c) Photo-catalytic reduction through optical excitation within a SERS-active material and subsequent charge-transfer into the reactive excited state of the adsorbed reactant.....	25

Figure 2.1: Schematic drawing of the theory of bipolar electrochemistry. A bipolar electrochemical cell consisting containing of two driving electrodes between which a voltage, E is applied and a bipolar electrode (BPE) where faradaic reactions occurs at both ends.....	39
Figure 2.2: Raman spectra of 4-NTP at six different locations along the BE, from (A) closest to the cathodic end to F) closest to the middle towards anode.....	46
Figure 2.3: Signal intensity of the NO <sub>2</sub> symmetrical stretching band (1344 cm <sup>-1</sup> ) versus the distance from the cathodic end. ....	46
Figure 2.4: The surface morphology visualized by using SEM (scale bar=100 nm) of the Au- Ag alloy deposit.....	47
Figure 2.5: Normal Raman spectra of solid 4-aminithiophenol (4-ATP) and 4-nitrothiophenol (4-NTP) .....	48
Figure 2.6: SERS spectra 4-nitrothiophenol (4-NTP) self-assembled monolayer on different surface.....	49
Figure 2.7: SERS spectra 4-aminothiophenol self-assembled monolayer on different surface....	50
Figure 2.8: Mechanism of the chemical reduction of SAM 4-NTP on alloy surface by NaBH <sub>4</sub> to DMAB and finally to 4-ATP catalyzed by Au-Ag alloy.....	50
Figure 2.9: SERS spectra recorded for the period of the reduction of 4-NTP to 4ATP catalyzed by the Au-Ag alloy gradient in the occurrence of NaBH <sub>4</sub> .The R-NO <sub>2</sub> and R-NH <sub>2</sub> represent the 4-NTP and 4-ATP, correspondingly.....	51
Figure 2.10: Cyclic voltammogram of Au-Ag (alloy gradients) electrode modified with 4-nitrothiophenol in 0.1 M NaClO <sub>4</sub> .....	55
Figure 2.11: In situ SERS spectra of 4-NTP SAM on an Ag- Au alloy electrode in 0.1 M NaClO <sub>4</sub> aqueous solution in a three electrode cell. The spectrum was obtained at near the edge of the cathodic pole before (blue) and after (red) application of a voltage of -0.9 V across the electrolyte.....	56
Figure 2.12: In situ SERS spectra of 4 NTP SAM on an Ag- Au alloy bipolar electrode in 0.01 M NaClO <sub>4</sub> aqueous solution at different potential in a bipolar electrode cell. The spectrum was obtained at the edge of the cathodic pole from 0V to 7 V across the electrolyte.....	58
Figure 2.13: In situ SERS spectra of 4 NTP SAM on an Ag- Au alloy bipolar electrode in 0.01 M NaClO <sub>4</sub> aqueous solution at different position in a bipolar electrode cell. The spectrum was obtained at 5 V across the electrolyte.....	60
Figure 2.14: In situ SERS spectra of 4 NTP SAM on an Ag- Au alloy bipolar electrode in 0.01 M NaClO <sub>4</sub> aqueous solution at different position in a bipolar electrode cell. The spectrum was obtained at 7 V across the electrolyte.....	61
Figure 2.15: In situ SERS spectra of 4 NTP SAM on an Ag- Au alloy bipolar electrode in 0.01 M NaClO <sub>4</sub> aqueous solution at different position and different potential in a bipolar electrode cell. The spectrum was obtained at 10 and 11 V across the electrolyte.....	62

Figure 2.16: First order decay measured at silver rich area, away from the cathodic pole on BPE for 1344 $\text{cm}^{-1}$ .....	64
Figure 2.17: Plot of the logarithm of the relative SERS intensity at 1344 $\text{cm}^{-1}$ ( $\ln(I_i/I_0)$ ) versus the reaction time.....	65
Figure 2.18: Calculated apparent rate constant for NTP reduction (1344 $\text{cm}^{-1}$ ) plotted as a function of Ag atomic percentage. 1595 $\text{cm}^{-1}$ peak intensity was considered here.....	65
Figure 2.19: $\text{NH}_2$ peak (1595 $\text{cm}^{-1}$ ) rising measured at different points along the BPE. Each point corresponds to a unique alloy composition. (Top to bottom: Ag at% is 100, 71.15, 51 and 40)...	66
Figure 2.20: Calculated apparent rate constant for NTP reduction plotted as a function of Ag atomic percentage. 1595 $\text{cm}^{-1}$ peak intensity was considered here. ....	67
Figure 3.1: Schematic representation of the principle of bipolar electrochemistry (A). The interfacial potential polarization between the solution and the bipolar electrode (B).....	76
Figure 3.2: Picture of the Au-Ag alloy deposited on stainless steel, both one dimensional and two dimensional.....	79
Figure 3.3: Picture of the home built two dimensional bipolar electrochemical cell.....	80
Figure 3.4: SEM image of the surface of a one dimensional Ag-Au alloy gradient deposited on stainless steel using bipolar electrodeposition.....	82
Figure 3.5: SEM image of the surface of a one dimensional Ag-Au alloy gradient deposited onto stainless steel using bipolar electrodeposition.....	82
Figure 3.6: Contour plot of atomic percentages of a two dimensional Ag-Au alloy gradient deposited onto stainless steel using bipolar electrodeposition.....	83
Figure 3.7: SERS spectrum of a benzene thiol SAM adsorbed on a two dimensional Ag-Au alloy film excited using 514.5 nm radiation.....	85
Figure 3.8: Integrated area under 1574 $\text{cm}^{-1}$ peak of benzene thiol SAM adsorbed on a two dimensional Ag-Au alloy gradient deposited onto stainless steel using bipolar electrodeposition.....	85

## Chapter One

### INTRODUCTION AND BACKGROUND

#### 1.1 Electrodeposition

Electrodeposition is a common word for some methods that developed on electrochemical processes to deposit material on a surface.<sup>1</sup> It is a film growth manner which contains the formation of metallic or semiconducting coatings on conductive surfaces from metal ion sources in a proper solvent and taking place through a charge transfer route.<sup>2-5</sup> This methodology has been broadly using to create coatings for decorative purposes and corrosion protections, in many other applications.<sup>6-8</sup> Electrodeposition of metals is important for a variety of industries including electronics, optics, and sensors, automotive and aerospace. The main metals of interest are Cr, Ni, Cu, Au, Ag, Pd, Zn and Cd together with a number of Cu, Au, Ag, and Zn -based alloys. The electroplating industry, from last 100 years, is based exclusively on aqueous solutions due to the low cost, high solubility of electrolytes and metal salts resulting in highly conducting solutions and high rates of mass transfer. Alloys can be prepared by combining two or more metals or non-metals. An easy example, steel is tougher than iron, its primary element. One easy technique to making alloy is electrodeposition. The theory of co-deposition of two or more than a few metals is of particular attention as the present development in engineering and technology requires the replacement of individual metals by their alloys, which usually have a broader range of properties. Alloy deposition is in principle a more complicated method as contrast to the deposition of pure metals. It involves an additional strict managing of the all parameters involves in the deposition system. Alloys are extensively used for several applications.<sup>9</sup> Here are some examples: Ni-Zn, Ni-

Au, Ni-Cd, Ni-Sn, Au-Cu, Au-Ag, Cu-Sn are used for protection and decoration purposes. Zn-Cd, Zn-Sn, Cr-Ni, Cr-Re are used for corrosion resistant. Pd- Ni, Au-Ni, Au-Co are used in electronics. Ag-Sb, Ag-Pd, Au-Pd, Pd-Ni, Au-Ni, Au-Sb, Pd-In, Rh-In are also used for electrical contact coatings and as catalyst.<sup>10</sup> At present there are more than hundreds of alloys that are synthesized using electrochemical methods. The most common are based on Cu, Au, Ag and noble metals. Electrochemical alloys frequently showed superior properties than single constituents even in contrast to metallurgical alloys.

In most of the situations, electrochemical alloy formation takes place only at the electrode surface level. Such electrochemical surface doping is frequently a suitable way of adjusting the properties of the metal working surface. The composition of alloy can be controlled by varying the applied potential. These routes are of interest both in practice, and from the fundamental standpoint, because of their capability to form exceptional alloys. These surface alloys can also be deposited in gradient manner on a surface with expanding its capacity in new and interesting directions.

## **1.2 Electrochemically generated gradients**

An increase or decrease in the degree of a property (e.g., temperature, pressure, or concentration) detected in moving from one point or moment to another is known as gradient. Gradients of physicochemical properties, their gradual deviation in space or time, are of great value both in solution and on surfaces. Gradients have been successfully engaged in materials science<sup>11</sup> and combinatorial/analytical chemistry<sup>12-13</sup> improving the proficiency of the design and finding of catalysts and drugs, and providing new analytical methods. There are several gradient-fabrication approaches in which electrochemistry plays a role. The properties of gradients produced by electrochemical techniques can be influenced in some ways, such as by the location and

arrangement of electrodes in combination with diffusion or by the variation of the applied potential. Electrochemical gradient creation methods have many additional beneficial properties. Electrochemical techniques are highly versatile, compatible with organic and inorganic systems and many solvents, and harmonious with conducting and nonconducting substrates. They can be integrated with electronics and are compatible with automation. There are several illustrations of gradients (established on bipolar electrodeposition method) that do not require leads, therefore allowing more direct scaling up for high-throughput uses. In some configurations, electrochemistry can be beneficial for quantitative examination of the gradient. One of the most direct methods for creating electrochemical gradients is established on mass transfer. At the working electrode, an electrochemical reaction generates  $\text{H}_3\text{O}^+$ ,  $\text{OH}^-$ , a catalyst, or any other types of interest, which diffuses away from the electrode, thus resulting in a concentration gradient of that classes depending on the distance to the electrode. This concentration gradient can be the anticipated result or, by the use of proper chemical reactions, can be used to achieve a gradient in reactivity, for instance, at a substrate. Nicosia et al reported an electrochemical method for the shape-controlled fabrication of micron-scale surface-bound chemical gradients.<sup>14</sup> They demonstrated that this arrangement lets the assembly of bi-component and biomolecular gradients along with the formation of surface gradients on external substrates once the active substrate is brought in close proximity to the microelectrode array. The method is built on using platinum microelectrode arrays on glass for the formation of a Cu (I) solution gradient through local electrochemical reduction of Cu(II) (cathodic reaction), and oxidation of the produced Cu (I) back to Cu (II) (anodic reaction), under ambient settings. The Cu (I) solution gradient is exploited for the surface-confined gradient creation via the Huisgen 1,3-dipolar cycloaddition (CuAAC). An alkyne in solution and an azide monolayer on the glass surface in among the platinum electrodes is present. Due to the high

sensitivity of the CuAAC on the Cu(I) concentration, they established the control of the shape of the micron-scale surface gradient, in terms of sharpness and surface density, as a function of the reaction conditions.<sup>14</sup> Gradients can be generated by the combination of electrochemistry and light. The intensity of light can be applied in a gradient fashion, for instance, by introducing a photomask with a gradient arrangement, to induce a chemical reaction that deprotects an electroactive layer (figure 1a).<sup>15</sup> Further electrochemical surface functionalization of the deprotected electroactive layer can then provide surface gradients. Dillmore et al developed a method for the immobilization of fluorescein in patterns and gradients.<sup>16</sup> A photo chemically active nitroveratryloxycarbonyl (NVOC)-protected hydroquinone monolayer was deprotected by UV illumination through a photomask to expose the redox-active hydroquinone in shapes and gradients. Following electrochemical oxidation of the hydroquinone formed the quinone, which reacted with a fluorescein-modified cyclopentadiene derivative in a Diels–Alder coupling (figure 1.1b).<sup>16</sup>

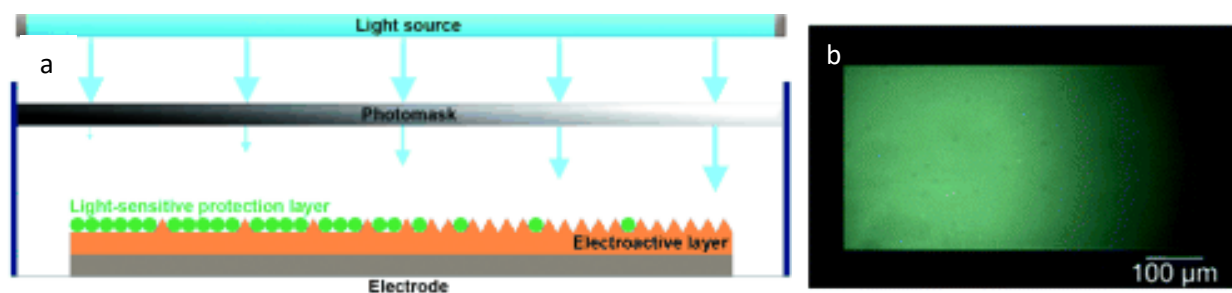


Figure 1.1: a) Creation of gradients by using a gradient in light intensity.<sup>15</sup> b) Examples of patterned substrates prepared by illuminating NVOC-protected hydroquinone through microfiche gradient mask.<sup>16</sup>

(Reprinted with permission from Ref 15. Copyright © 2014 WILEY-VCH Verlag GmbH & Co. KGaA, Weinheim and Ref 16. Copyright © 2004, American Chemical Society)

An asymmetric electrode arrangement in the experimental setup (figure 1.2a) also can be used for the formation of electrochemical gradients by an in-plane potential gradient.<sup>15</sup> The in-plane potential gradient on the working electrode is directed by the location of the counter electrode. At positions further away from the counter electrode, there is a higher component of solution resistance, which pull down the applied potential at those locations, thus leading to a gradient in an electrochemical reaction. Furthermore, two dimensional gradients were recently fabricated by combining a porous-silicon pore-size gradient (figure 1.2b) with an orthogonal density gradient of acyclic RGD peptide ligand.<sup>17</sup> Contour plot of MSC attachment on top of an orthogonal gradient of pore size and  $c(\text{RGDfK})$  density showed in figure 1.2 b. Five (5) different areas are showed, from high  $c(\text{RGDfK})$ /small pore size (1), intermediate  $c(\text{RGDfK})$ /intermediate pore size (2), low  $c(\text{RGDfK})$ /large pore size (3), high  $c(\text{RGDfK})$ /large pore size (4), low  $c(\text{RGDfK})$ /small pore size (5).<sup>17</sup>

An interesting class of electrochemical gradients can be created by an in-plane potential gradient is the bipolar electrochemical gradient. In contrast to the situation in figure 1.3b, there are no conducting leads to either side of the bipolar electrode, and the single bipolar electrode side is both the anode and the cathode. Furthermore, there is a potential gradient in solution, whereas the bipolar electrode has a potential that is (approximately) equal everywhere on its surface. Consequently, a potential difference is created between the surface of the bipolar electrode and the solution, and this potential difference differs in-plane laterally the surface. When sufficient voltage is applied to an electrolyte solution containing a bipolar electrode, the potential difference between the bipolar electrode and the electrolyte solution drives electrochemical reactions, with the highest reaction rates at the edges of the bipolar electrode. Both one dimensional and two dimensional gradients can be fabricated with this method.<sup>18</sup>

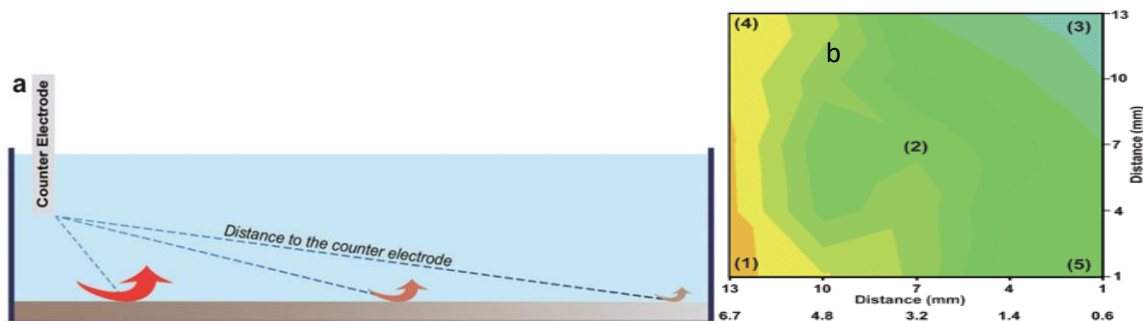


Figure 1.2: a) Creation of electrochemical gradients by the use of an asymmetric electrode-configuration.<sup>15</sup> b) Contour plot of the gradient of pore size and c (RGDFK) density.<sup>17</sup>

(Reprinted with permission from Ref 15. Copyright © 2014 WILEY-VCH Verlag GmbH & Co. KGaA, Weinheim and Ref 17. Copyright © 2012, Royal Society of Chemistry)

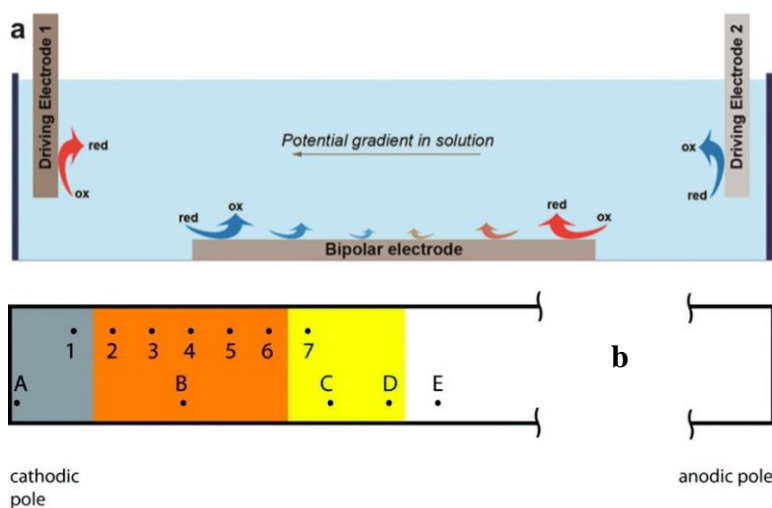


Figure 1.3: a) Creation, at a bipolar electrodeposition cell<sup>15</sup>, b) Diagram of the geometry used for AES and Raman analysis.<sup>20</sup>

(Reprinted with permission from Ref 15. Copyright © 2014 WILEY-VCH Verlag GmbH & Co. KGaA, Weinheim and Ref 20. Copyright © 2010, American Chemical Society).

Bjçrefors and co-workers used bipolar electrochemistry in 2008 for the fabrication of thiol gradients.<sup>19</sup> Additionally, Shannon's research group made-up Cd-S (figure 3b)<sup>20</sup> and Ag-Au<sup>21</sup> alloy gradients by electrodeposition on a stainless steel bipolar electrode.

### 1.2.1 Applications of Electrochemically Fabricated Gradients

Electrochemical gradients have been used for a countless of applications. Here, we listed the application of gradients made-up by only electrochemical methods and by electrochemistry in pairing with other methods.

1. Cell-Migration Studies
2. Driving Motion
3. Towards Devices
4. High-Throughput Deposition
5. High-Throughput Screening

Cell adhesion was studied with electrochemically generated gradients, in carboxylic acid terminated self-assembled monolayers (SAM), after functionalization with fibronectin.<sup>22</sup> In recent times, Malliaras et al reported about the achievement of electrical control over protein conformation by using the in-plane potential-gradient technique, which applied on an ITO/conductive polymer hybrid.<sup>23</sup> Fixed gradients can drive motion, for instance, of liquid droplets. Berggren et al discussed about showed liquid motion on static wettability gradients created by the use of an in-plane potential gradient.<sup>24</sup> Quite a few studies have been done by using the gradients for device improvement. Sailor et al described the electrochemical assembly of a pore-size gradient in Si by using an asymmetric electrode arrangement. It was used as a size-exclusion medium in the determining the proteins sizes.<sup>25</sup> Carreon-Gonzalez et al established a new and inexpensive combined electrodeposition and dip-coating system for the assembly of arrays of nanowires with a linear changeable height profile. This method permits adjusting the key factors of the height gradient outlines, those are maximum wire height and the lateral span of the wire array. This device showed better performance than a device through an asymmetrical

arrangement of nanowire lengths in a stair way like shape.<sup>26</sup> Bimetallic alloy gradient electrodeposition is a very typical method to formulate asymmetric surfaces. In this thesis we showed electrodeposition of Au-Ag alloy in gradient manner by using Bipolar electrochemical method.

### **1.3 Bipolar Electrochemistry:**

In this thesis the thought of bipolar electrochemistry with a view to expanding its capacity in new and interesting directions has been introduced. This is a valuable goal, because the broad implementation of electrochemical methods has underscored a few shortcomings of existing techniques, apparatuses, and theory. These consist of the difficulty of making direct<sup>27</sup> electrical contact to nanoscale electrodes, maintaining control over and reading out very large arrays of electrodes all together, regulatory electrodes that are mobile in solution, sustaining a non-uniform potential difference over the surface of an electrode, and by using electrodes to control local solution potentials. At least to some extent, bipolar electrodes (BPE) are the solution for all of these aspects of electrochemistry. Bipolar electrochemistry has been around for quite a long time, and it has been used since the 1960s. Beginning in the 1960s, Fleischmann, Goodridge, Wright, and co-workers portrayed fluidized bed electrodes, where a voltage applied between two driving electrodes facilitates electrochemical reactions at distinct conductive particles.<sup>28-33</sup> In the present decade, it has achieved significant extra concentration.<sup>34-35</sup> The idea has shown a strong potential for the expansion of integrated circuits,<sup>36</sup> electrical contacts,<sup>37</sup> and electronic devices.<sup>38</sup> It has also been used for analytical purposes such as preconcentration,<sup>39-40</sup> separation,<sup>41-42</sup> electrochemical sensing<sup>43-44</sup> and optical detection.<sup>45-46</sup> Bipolar plate technology is significant for polymeric electrolyte membrane (PEM) fuel cells by forming the plates, a series of BPEs.<sup>47-48</sup> In addition,

neuronal behavior can also be imitated using short-circuited micro bands which perform as a BPE forming logic gates.<sup>49</sup>

The idea of bipolar electrochemistry is very different from the established three-electrode electrochemical cell which operates with a working, counter, and reference electrode. The electric field that powers bipolar electrochemistry is typically applied by two driving electrodes, which can be metallic (e.g., Au, Ag, Pt, or stainless steel), glassy carbon or graphite. The substrate (BPE) can be any kind of material, but its conductivity should be larger than its surrounding medium. Experimentally bipolar electrochemistry has pretty simple set up, but there are many features to study to produce a controlled arrangement. The unique properties of a bipolar electrode arise from the fact that its polarization is controlled on the outside and indirectly through the gradient in the solution potential. The difference with the typical three electrode setup is there all electrodes are in electrical connection to the power source. The bipolar electrode is formed by applying the potential (DC electric fields) difference across two feeder electrodes, generating a gradient in the solution potential. This consequently generates a gradient in the potential difference between the solution and the conducting surface of the bipolar electrode, along its entire length. When this potential difference is adequate, electrochemical reactions can take place, with oxidation reactions taking place at the end of the BPED near the negative electrode (the anodic pole of the now active bipolar electrode), and vice versa for the reduction reaction (figure 1.4). Part of the total cell current ( $i_{tot}$ ) then passes through the bipolar electrode ( $i_{bpe}$ ), with the balance over current passing through the electrolyte ( $i_{electrolyte}$ ). Without the bipolar electrode, the equation is  $i_{tot} = i_{electrolyte}$ , when including the bipolar path, the equation becomes  $i_{tot} = i_{electrolyte} + i_{bpe}$ . This is displayed schematically in figure 1.4. The floating potential of the bipolar electrode, because of the lack of external connection, makes it challenging to define the exact potential difference at a certain point

on the surface of the bipolar electrode. This is also one of the characteristic challenges with this system. A straight method of determining the theoretical highest potential difference diagonally a bipolar electrode,  $\Delta E_{BPE}$ , generally follows equation 1.1.<sup>50</sup> Where  $E_{tot}$  is the applied external potential,  $l_{BPE}$  is the length of the bipolar electrode and  $l_{channel}$  is the distance between the feeder electrodes. From this equation, it is seen that a longer piece, relative to the length of the channel, will become bipolar at lower external field strengths. The external field strength is also straight linked to the conductivity of the electrolyte. Therefore, the composition of the electrolyte is a very important aspect: if its conductivity is too high, the potential drop across the object will not be adequate to drive reactions on the bipolar electrode surface, and the current will pass from side to side the in electrolyte only. This as well suggests that the conductivity of the would-be bipolar electrode is vital, besides how straightforwardly reactions can take place on its surface.

$$\Delta E_{BPE} = E_{tot} \left( \frac{l_{BPE}}{l_{channel}} \right) \quad (1.1)$$

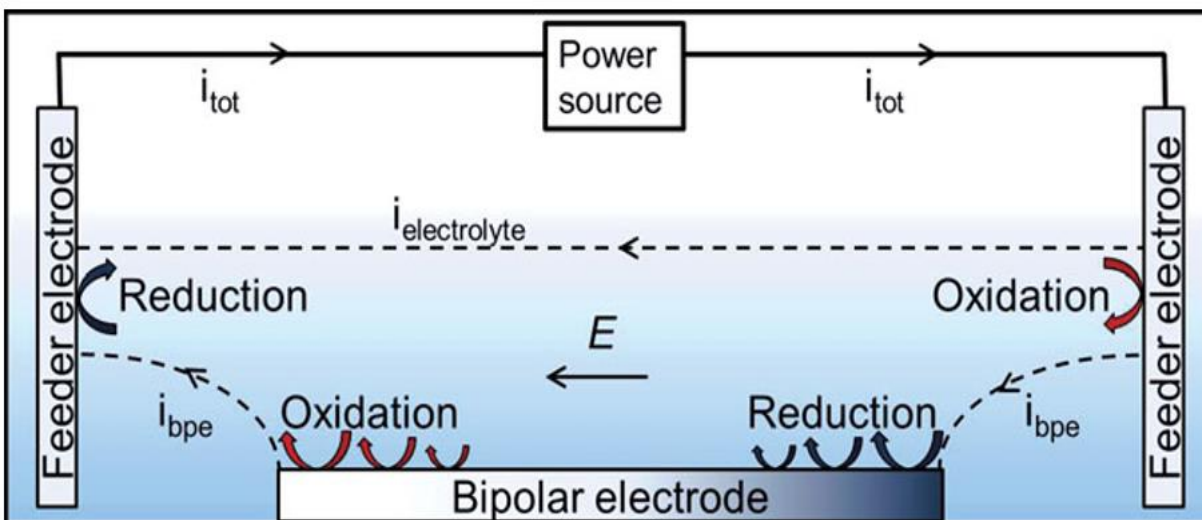


Figure 1.4. Schematic of the bipolar system. E indicates the direction of the applied external electric field.<sup>19</sup>

(Reprinted with permission from Ref 19. Copyright © 2008 WILEY-VCH Verlag GmbH & Co. KGaA, Weinheim)

Similarly, because of the lack of external connection,  $i_{bpe}$  cannot be determined directly in this basic setup. Moreover, the current density at any given point on the surface is even more difficult to determine. The gradient in electrochemical potential on the electrode means there is a corresponding gradient in the over potential for electrochemical reactions taking place on the surface. There is therefore a gradient in the current density profile across the electrode.

Duval and his coworker has proven current density along a bipolar electrode could be modeled by studying dissolution of aluminium wafers performing as bipolar electrodes. The model is based on electric field homogeneity and irreversible electron transfer-limited reactions.<sup>51</sup> Mavré's group did similar research established on determining the electro chemiluminescence of ruthenium bipyridine complexes generated at bipolar electrodes. A graphic diagram of their authenticated model is showed in figure 1.5.<sup>34</sup> Figure 1.5 a and 1.5 b, demonstrates the portion of the current passing through the bipolar electrode be influenced by on relative values of the resistance of the electrolyte ( $R_e$ ) and of the total resistances related to the bipolar electrode ( $R_{bpe}$ ). The variation in potential drop and local drop in electric field close to the bipolar electrode, induced by part of the total current flowing through the bipolar electrode is shown in figure 1.5c and 1.5d, correspondingly. Lastly figure 1.5 e, portrays the current profile diagonally the bipolar electrode.

Bipolar Electrochemistry could be commercially incorporated into and deliver exciting functionality to a broad range of applications. The bipolar electrochemistry offers an appropriate platform for sensing electroactive analytes in micro-devices. For example, high electric fields are essential for capillary electrophoresis, where Klett et al reported a potentiostat-less detection system for amperometric detection of electroactive species in capillary electrophoresis.<sup>52</sup> Two gold micro bands placed 10  $\mu\text{m}$  away from each other, as a split bipolar electrode connected on the exterior to an ammeter. The potential difference and current in the capillary electrophoresis outlet

was examined with varying electric fields and concentrations of a redox couple  $(\text{Fe}(\text{CN})_6^{4-}/\text{Fe}(\text{CN})_6^{3+})$ . The current was proportionate to the concentration of the redox couple at a sufficient electric field. And the detection limit of  $100 \mu\text{M}$  of the analytes.

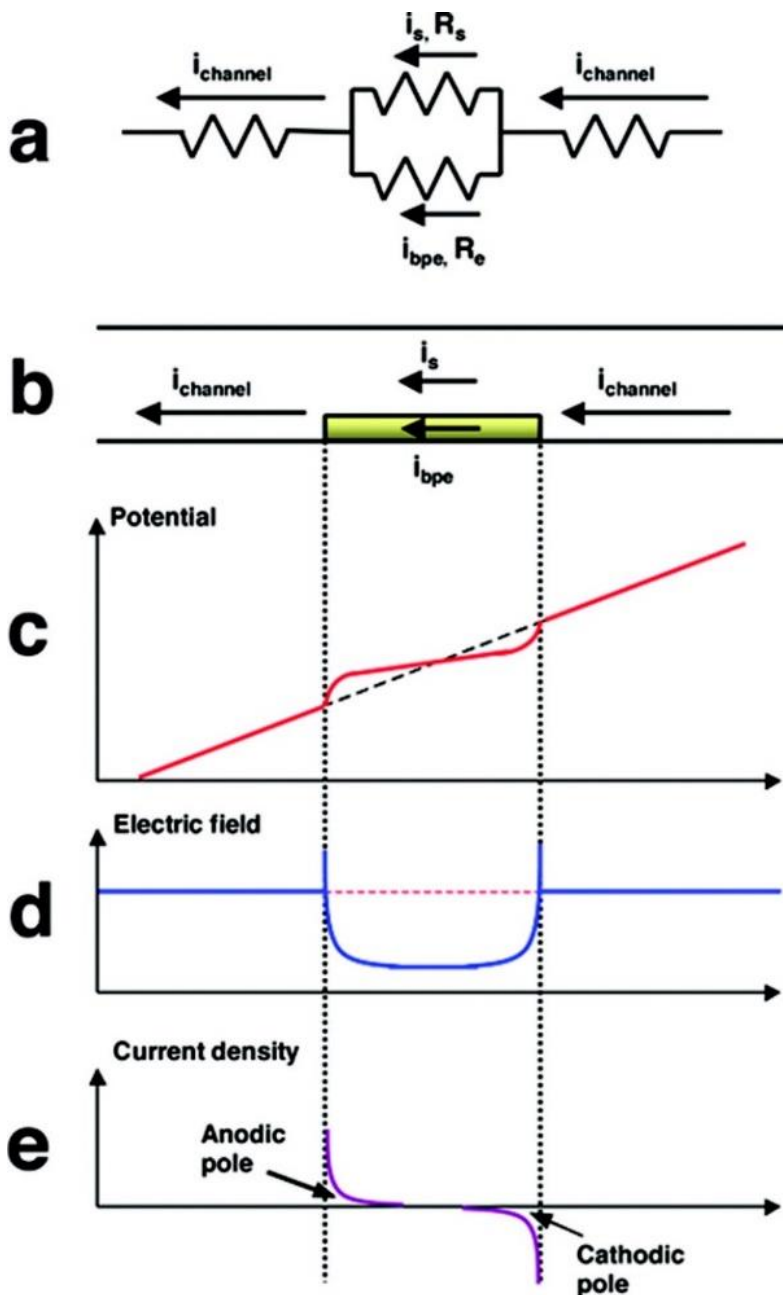


Figure 1.5: a) Equivalent circuit and b) simplified representations of a bipolar system. c) and d) represent the potential and electric field profiles across the cell, and e) represents a typical current density profile across the bipolar electrode.<sup>34</sup>

(Reprinted with permission from Ref 34. Copyright © 2010, American Chemical Society)

Electro generated chemiluminescence (Electrochemiluminescence, ECL) is the release of light as a consequence of an electrochemical reaction, and demonstrated to be very beneficial in analytical uses as an extremely sensitive and selective method.<sup>53-54</sup> By applying potential on the electrode in the luminophore and co-reactant, ECL can be produced. One of the common ECL system uses ruthenium trisbipyridyl  $\text{Ru}(\text{bpy})_3^{2+}$  as the light-emitting compound and an amine, such as tri-n-propylamine (TPrA) as a co-reactant. ECL is useful in the sensing devices constructed on bipolar electrochemical method. Manz first combined ECL with bipolar electrochemistry as a signal reporting technique.<sup>55</sup>

Surface gradient materials can have variable molecular functionalities or chemical properties along the materials. They are highly striking because of their potential sensor and biomimetic uses. Bipolar electrochemistry offers the proper surroundings for creating gradient established on the potential gradient alongside the bipolar electrode. Björefors and his group<sup>19</sup> generate a surface gradient of molecular functionality, by way of the adsorption or desorption of a definite molecule can be controlled through the bipolar-electrode reactions. Shannon et al presented the idea of creating solid-state material libraries along a bipolar electrode.<sup>20-21</sup> The deposition of Cd, CdS and S gradients on a gold wire formed by dipping gold wire in a solution having  $\text{S}_2\text{O}_3^{2-}$  and  $\text{Cd}^{2+}$  ions.<sup>20</sup> The deposition was done by applying an adequate electric field. The deposition potentials of Cd, CdS and S are contradiction hereafter, the deposition of each one happened at a different location along the wire. The resulting film was screened by resonance Raman spectroscopy and Auger electron spectroscopy.<sup>20</sup> The reduction of  $\text{Cd}^{2+}$  into  $\text{Cd}^0$  started at the cathodic pole, trailed by a stoichiometric CdS, and completed with S deposition, when starting from the cathodic pole headed to the center of the BP electrode. In an additional analogous method, they described the synthesis of Ag-Au alloy gradients on stainless steel substrates.<sup>21</sup> This was

confirmed by energy dispersive X-ray spectroscopy (EDX), which exhibited the Ag atomic percentage at the cathodic edge to be approximately 55 to 100, with an approximately linear difference of this percentage as a function of lateral location.<sup>21</sup>

Conducting polymers also can be deposited in gradient manner. Usually they have high conductivity and display significant color changes when reduced or oxidized due to the variation in the polymer band gap. Ishiguro and his group effectively generated the bipolar gradient patterning of poly(3-methylthiophene) (PMT) film which was used as a bipolar electrode.<sup>56</sup> This effort was then prolonged to gradient doping of additional conducting polymers for example, poly(3,4-ethylenedioxythiophene) (PEDOT) and poly(aniline) (PANI).<sup>57</sup> Optical micrographs of the three doped polymer gradient films are shown in figure 1.6.

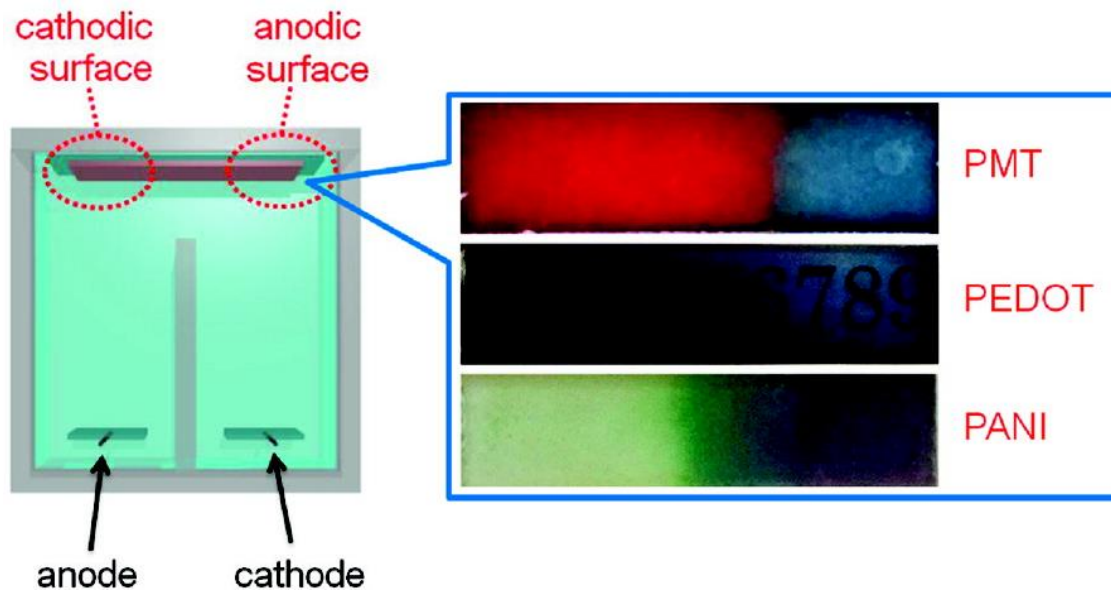


Figure 1.6: Photographs of three different conducting polymers that have been doped in a gradient manner using bipolar electrochemistry.<sup>57</sup>

(Reprinted with permission from Ref 57. Copyright © 2011, American Chemical Society)

#### **1.4 Raman Spectroscopy:**

Inelastic scattering of light was calculated by Adolf Smekal in 1923.<sup>58</sup> It came into practice in 1928 when Raman Effect was discovered. The Raman effect was discovered by an Indian scientist Sir Chandrasekhara Venkata Raman who observed the consequence by means of sunlight (1928, with K. S. Krishnan and individually by Grigory Landsberg and Leonid Mandelstam).<sup>59</sup> Raman earned the Nobel Prize in Physics in 1930 for this innovation accomplished by sunlight, a narrow band photographic filter to create monochromatic light, and a "crossed filter" to block this monochromatic light. He established that a small amount of light had changed its frequency by passing through the "crossed" filter. From the time of the discovery of the Raman effect in 1928, Raman spectroscopy become a field of major progress. In the beginning years, this system was primarily used to study vibrational states of simple molecules. This was because of the unavailability of strong monochromatic light sources and suitable optical components and detectors. Conversely, after the discovery of lasers in 1960s and the progress of high throughput monochromators and responsive detectors, Raman spectroscopy has been increasingly applied to solve problems of both fundamental and technological interest.<sup>60</sup>

A raman spectrum is acquired by exposing a sample to a monochromatic source of exciting photons, and measuring amount of the light intensity on the frequencies of the scattered light. In Rayleigh scattering the energy of the scattered photon are same as incident. But in stokes scattering its lower than the incident and for anti-stokes it is higher. All three states involve in light scattering are showing in figure 1.7. The second are called Raman scattering. The intensity of the Raman scattered light is lower than that of the Rayleigh scattered component. Filters and diffraction gratings are used to suppress the latter constituent. A highly responsive detector is necessary to sense the weakly scattered Raman photons. A number of variations of Raman spectroscopy have

been developed. The typical purpose is to boost the sensitivity (e.g., surface enhanced Raman), improve the spatial resolution (Raman microscopy), or to acquire very precise information (resonance Raman).

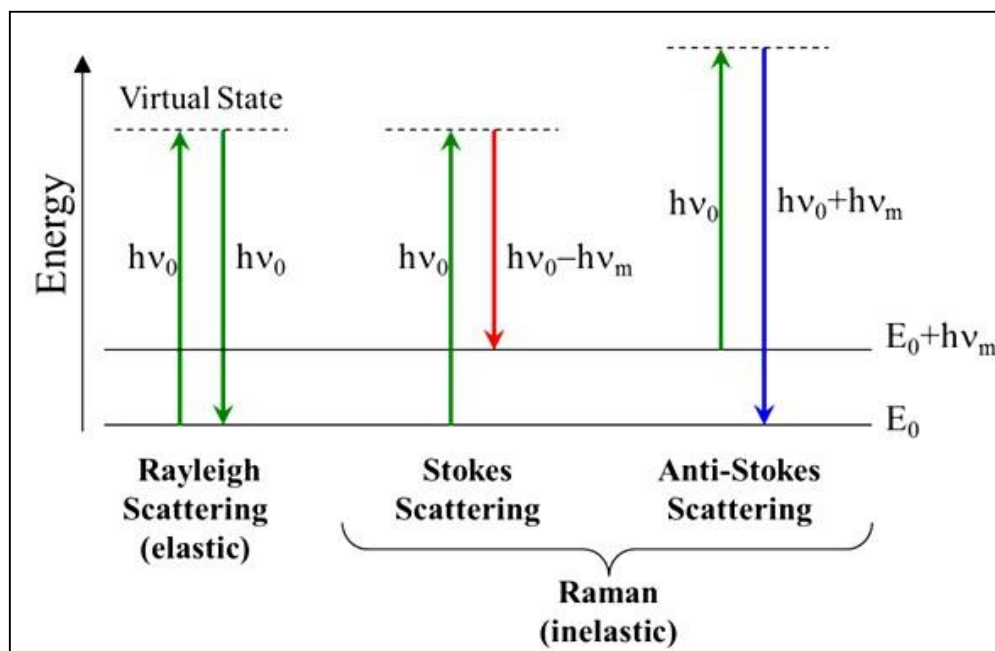


Figure 1.7: Energy-level diagram showing the states involved in Raman signal. Rayleigh scattering (no exchange of energy), Stokes Raman scattering (atom or molecule absorbs energy), Anti-Stokes Raman scattering (atom or molecule loses energy).<sup>61</sup>

### 1.4.1 Surface Enhanced Raman Scattering (SERS)

SERS was accidentally discovered by Fleischmann while trying to do Raman on the electrode in 1974. He observed intense Raman scattering from pyridine adsorbed on a roughed silver electrode surface from aqueous solution. The goal for this work was to build up a chemically specific spectroscopic probe which could be used to study electrochemical processes. Fleischmann's idea was to generate a high surface area on roughen electrode.<sup>62</sup> Jeanmaire and Van Duyne<sup>63</sup> and Albrecht and Creighton<sup>64</sup> recognized separately that the large intensities observed

could not be accounted for simply by the increase in the number of scatterers present and proposed that an enhancement of the scattered intensity occurred in the adsorbed state. Jeanmaire and Van Duyne tentatively proposed an electric field enhancement mechanism whereas Albrecht and Creighton guessed that resonance Raman scattering from molecular electronic states, expanded by their interaction with the metal surface, might be responsible.<sup>64</sup>

SERS research speed up significantly in the near the beginning 1980s with contributions from chemists, physicists and engineers from around the world. By 1985, undoubtedly, the experimental facts were generally agreed upon as were the essential features of the mechanisms. SERS varies from regular Raman spectroscopy of molecules and solids.<sup>65</sup> The intensities of the bands observed usually fall off with increasing vibrational frequency; C–H stretches. Overtones and combination bands are not common. Selection rules are relaxed resulting in the appearance of normally forbidden Raman modes in the surface spectra. The spectra tend to be totally depolarized, in comparison to solution spectra and those taken from molecules adsorbed on even, flat surfaces. Excitation profiles differ from the  $\omega^4$  dependence of nonresonant scattering; the broad resonances observed may be characteristic of the substrate, the adsorbate or the joint system.<sup>66-67</sup> Excitation profiles depend upon electrode potential in electrochemical experiments and may be different for different vibrational modes. The enhancement may be remarkably long ranged, extending tens of nanometers from the surface, depending upon the substrate morphology.<sup>67</sup>

Many mechanisms were proposed in the early days of SERS to explain the experimental facts mentioned above. A number of them have survived and are swiftly sorted into two divisions which were called electromagnetic and chemical enhancement. As their names indicate, the former focus on the enhanced electromagnetic fields which can be supported on metal surfaces with appropriate morphologies and the latter on changes in the electronic structure of molecules which

happen upon adsorption and which can guide to resonance Raman scattering. Brief reviews of the relevant features of these mechanisms are given below.

#### **1.4.1.1 Electromagnetic enhancement**

The collective excitation of the electron gas of a conductor is known as a plasmon; if the excitation is limited to the near surface region it is called a surface plasmon. Electromagnetic enhancement arises from the interaction of light (both incident and scattered) from the substrate. It is a long-range effect. It is independent from the properties of the probe molecules. Localized surface plasmon resonance (LSPR), the lightning rod effect, and the image field effect all have contribution for SERS.<sup>68</sup> Among them, LSPR has the major contribution to the electromagnetic field enhancement and consequently SERS. LSPR can be tuned by controlling the composition, shape, size, and the interparticle spacing of nanoparticles and their assemblies; to obtain the optimized SERS substrate at the preferred wavelength.

#### **1.4.1.2 Chemical Enhancement**

This enhancement can be clarified by a resonance Raman mechanism in which either the electronic states of the adsorbate are shifted and broadened by their interaction with the surface or new electronic states arise from chemisorptions provide as resonant transitional states in Raman scattering. The highest occupied molecular orbital (HOMO) and lowest unoccupied molecular orbital (LUMO) of the adsorbate are symmetrically organized in energy with respect to the Fermi level of the metal (figure 1.8). So that the charge transfers excitations can take place at about half the energy of the intrinsic intra molecular excitations of the adsorbate.<sup>69</sup>

#### **1.4.2 Substrate-related issues of SERS**

After 30 years of improvement, surface enhanced Raman spectroscopy (SERS) is now facing a very crucial stage in its history. The explosive progress of nanoscience and

nanotechnology has helped the development of SERS, especially throughout the last 10 years. Additional expansion of surface-enhanced Raman spectroscopy is mainly limited by the reproducible research of fresh and extremely surface enhanced Raman scattering (SERS) active substrates. Here we discuss with some substrate related topics.

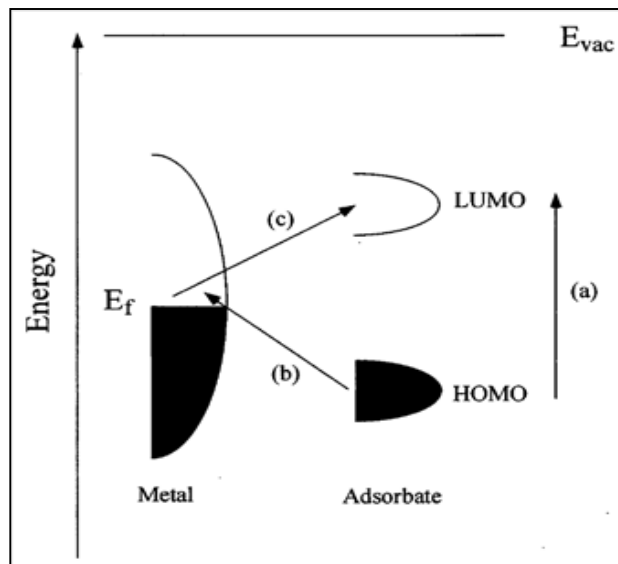


Figure 1.8: Typical energy level diagram for a molecule adsorbed on a metal surface. The occupied and unoccupied molecular orbital are broadened into resonances by their interaction with the metal states; orbital occupancy is determined by the Fermi energy. Possible charge transfer excitations are shown.<sup>65</sup>

(Reprinted with permission from Ref 65. Copyright © 1969, Royal Society of Chemistry)

Combining some literature, we can make some conclusions about the features of an ideal SERS substrate.<sup>70</sup>

1. The substrate should have high SERS activity and consequently offer high sensitivity. By controlling the size (more than 50 nm) and interparticle positioning (less than 10 nm) of nanoparticles, the LSPR frequency of the substrate can be tuned to match the incident laser frequency and the successful coupling among nanoparticles can be induced to maximize the enhancement.

2. The substrate should be consistent so that the divergence in enhancement over the whole surface can remain less than 20%, which requires a relatively ordered array of the nanoparticles on the substrate.
3. The substrate should have excellent stability and reproducibility. The enhancement result needs to still be same after a long shelf time. The difference in the enhancement must be less than 20% for different groups of substrates prepared by the same method.
4. The substrate should clean so that it can be applied to study for both strong and some weak adsorbates and even unknown samples.

At present, it is still not easy to attain SERS substrates that can concurrently meet all of the above requirements. According to the particular application, one has to make some trade-offs. For instance, in quantitative analysis, a consistent and reproducible substrate is enormously important; on the other hand, in trace analysis, the maximized enhancement is the precondition. In bio-related detection, a clean and highly enhanced substrate is usually required owing to the complication in bio systems studied to allow for a reasonable assignment of the detected spectral bands.

Numerous methods to prepare ideal SERS substrates have been established, where metal nanoparticles are used as highly ordered SERS substrates and the advantages and challenges when they are used as SERS substrates. Each method has its advantages and drawbacks. For that reason, we should choose the right method to achieve a SERS-active substrate for a specific application. It is assumed that the rapid expansion of nanoscience and nanotechnology will accelerate the development toward this target, which will ultimately permit a fundamental understanding of the SERS effect and a broad application of SERS in analytical science and biomedical sciences.

## 1.5 Surface Enhanced Raman Scattering in Catalysis

SERS is a great prospective technique in the arena of catalysis, to observe those reactions that take place on catalytic surfaces. Quite a few reviews have addressed this topic.<sup>71-72</sup> The combination of SERS and catalysis in a single experiment has been accomplished in several investigational set-ups. As SERS was initially discovered on Ag electrodes, there is no wonder that the primary reactions studied were electrochemical in nature. These early studies did not use the Ag surface of the electrodes as catalytic surface, but instead thin layers of catalytically active transition metals that were deposited onto the electrode surfaces.<sup>73</sup> Researchers are trying to combine different approaches of combining catalysis and SERS. Nano-roughened transition metal surfaces do also show (weak) SERS-enhancement, and can be used directly as both catalyst and enhancement material. Alternatively, small catalytic particles have been deposited on top of SERS-active substrates.<sup>74-77</sup> Many catalytic routes have been examined with SERS, but over-all no step is taken later observe the product. SERS should be appropriate for reaction elucidation, more quantifiable characterization, and eventually, the study of specific nanoscale dynamic sites. Reaction monitoring on single catalytic particles can be attained via SERS, but needs a supplementary characterization method to classify, confine, and illustrate the morphology features over a surface with catalytic particles.

SERS is a surface-dependent method. As those molecules adsorbed onto a SERS material are measured efficiently, as a reaction takes place on the surface. To show the applicability of nano-scale analysis using SERS, the reaction must be easy to initiate and must show adequate signal to permit time resolved observation of reaction. The best documented chemical reactions studied with surface-enhanced Raman scattering are related to 4-nitrothiophenol (4-NTP) and 4-aminothiophenol (4-ATP). These molecules have huge absorption cross-sections at visible

wavelengths, and are in this manner easily identified at low concentrations. Specially if SERS-active particles are too involved, this can lead to surface-enhanced resonance Raman scattering (SERRS) at definite excitation wavelengths. The reduction of 4-NTP has been studied ever since the 1990's,<sup>78</sup> but in the more general terms of the reduction of nitro-aromatics, literature goes back to 1968.<sup>79</sup> There are various mechanisms to reduce nitro-aromatics, including photo-chemical reduction via ultraviolet (UV) excitation, electro-chemical reduction, and photo-catalytic reduction. Understanding the various reaction pathways is critical for interpretation of experimental condition, as a lot of variables can affect the SERS-observations. The catalytic reduction of 4-NTP is used as a model-reaction in this Thesis, and the SERS studies require in-depth knowledge of this class of reactions. The thiol functionality of 4-NTP assures that the reaction takes place right at the catalyst surface. This makes it perfect for trying unique spectroscopic methods.

### 1.5.1 4-NTP reduction Mechanisms

The reduction of nitro-aromatics can be accomplished in a variant of ways. Most straight is chemical reduction, but alternate pathways have received a great deal of interest. These pathways can be distributed into three main classes: UV photo-chemistry, electrochemistry, and plasmon-mediated photo-chemistry or photo-catalysis.

**Chemical Reduction** The reaction from nitro-aromatics to amino-aromatics is a reduction process, and therefore requires a reductant to occur, e.g.  $\text{NaBH}_4$  or  $\text{H}_2$ . Metal nanoparticles can accelerate this route through electron transfer between reduction agent and reactant.<sup>80</sup> The chemical reduction of 4-NTP (figure 1.9) has been studied by SERS with variation of the catalyst, as well as with Au<sup>81</sup> is achieved with  $\text{NaBH}_4$ , though exceptions are known, in the form of  $\text{KBH}_4$ <sup>83</sup> and  $\text{H}_2/\text{N}_2$ .<sup>85</sup>

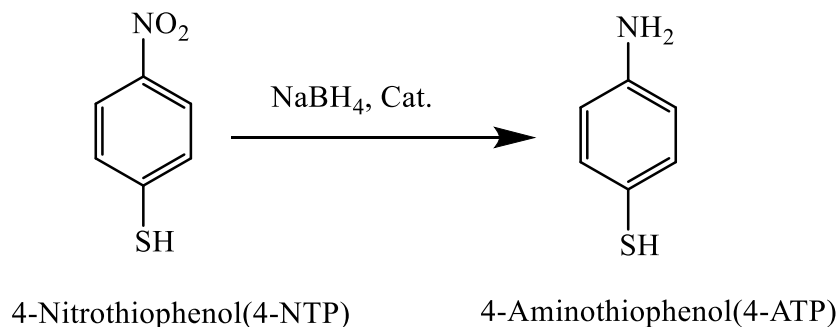


Figure 1.9: Chemical reduction of 4-NTP to 4-ATP

**Photo-Chemical Reduction** - For a molecule in solution, a certain activation energy is required to excite it from the ground state to its electronically excited state. For ‘normal’ photo-chemistry, the excitation wavelength needs to correspond to, or be higher than, the activation energy, as illustrated in figure 1.10a. A photochemical process usually requires high energy excitation, in the UV-wavelength range. This photo-chemical reduction has also been used to photo-pattern SAMs of 4-NTP on Ag island films,<sup>87</sup> but no other studies have been reported. But, the most recent reported reaction mechanisms for electrochemical and photo-catalytic reduction<sup>88</sup> are based on the photo-chemical reaction mechanism as published by Barltrop et al.<sup>79</sup>

**Electrochemical Reduction** - A similar process occurs in electrochemistry. The ground state of an adsorbed molecule on an electrode is not necessarily the same as in solution, but probably similar. Under normal circumstances, the electrode will have an energy level around its Fermi level. Through application of a potential this energy level can be increased. As soon as the bias has reached the level of the reactive excited state of the adsorbed molecule, the electrons will ‘leak’ into that state via the charge-transfer process and start the reaction (figure 1.10b). Matsuda et al described the combination of cyclic voltammetry and in-situ surface-enhanced infrared absorption (SEIRA) for the full electrochemical reduction of 4-NTP to 4-ATP.<sup>78</sup>

**Photo-Catalytic Reduction** - Midway between photo-chemistry and electrochemistry is the photo-catalytic reduction. Specific nanoparticles, usually gold or silver, have a Fermi-level higher than the ground state of the adsorbed molecule. These particles are also capable of coupling to specific wavelengths of light through their plasmon resonance. As illustrated in figure 1.10c, this light effectively heats up the electrons in the metal and increase their energy up to the level of their excited state of the adsorbed molecule. Through a charge transfer process this energy is transferred, so a reaction can be started. The photo-catalytic reduction of 4-NTP mechanism was first reported by Han et al. in 2002,<sup>89</sup> ever since then trailed by many others. The reduction readily occurs when adsorbed onto Ag SERS-active substrates and under excitation of a green laser. The reaction has generally been observed on Ag, but was also found on Cu<sup>90</sup> and Au.<sup>81</sup> The reaction rate was strongly dependent on the excitation wavelength used and the laser power density. On Ag, 532 nm readily excites strong surface plasmons, while the same power density at 633 nm has been shown to yield a much lower reaction rate.<sup>91</sup>

The reaction mechanisms of photo-chemical, electrochemical, and photo-catalytic reductions are very similar in nature, and can easily overlap. In all cases, excitation energies, whether optical or electric, must be coupled to the respective plasmon resonances or exciton energies, and consequent excited electrons should be high enough in energy to allow for charge-transfer to the excited reactive state of 4-NTP, as illustrated in figure 1.10. Most commonly probed is the combination between electro-chemical reduction and photo-catalytic reduction, when SERS is used for in-situ reaction monitoring. The electrode potential can give the metal the right push to increase the energy of electrons excited by laser excitation to the surface plasmon, and thereby reach the charge-transfer level into the adsorbate reactive excited state. The parameters that determine whether a measurement and catalysis are independent, are:

- SERS-active material
- Local SERS near-field intensity
- Excitation wavelength and laser power density
- Electrochemical potential, pH and reaction temperature.
- Surface coverage of reactant
- Concentration of reducing agent
- Reaction temperature.

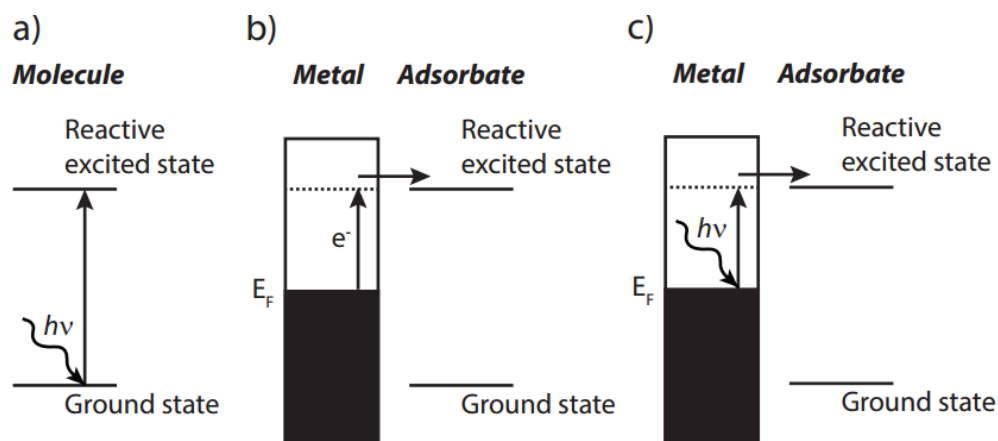


Figure 1.10: Various reduction mechanisms. a) Photo-catalytic reduction through direct photonic excitation of the reactant molecule into the reactive excited state. b) Electrochemical reduction through increase in electrode potential and subsequent charge-transfer into the reactive excited state of the adsorbed reactant. c) Photo-catalytic reduction through optical excitation within a SERS-active material and subsequent charge-transfer into the reactive excited state of the adsorbed reactant.<sup>94</sup>

Apart from the various reaction parameters, it is also important to be aware of the differences in the analytical tools used for reaction monitoring. Electrochemical characterization techniques, like cyclic voltammetry, are bulk techniques: they analyze the full SAM simultaneously. Coupling of electrochemical reactions to SERS measurements can cause convolution of electrochemical and photo-catalytic reduction. However, SERS will only measure at the so-called 'hot-spots' within the laser focus, whereas e.g. cyclic voltammetry will measure the full electrode surface. The variations in measurement volume can and will lead to discrepancies between different characterization techniques, if measurement and catalysis are not separated for the SERS measurement.

**Reduction Product:** SERS spectroscopy is a very informative technique that yields molecule sensitive information. Though, there are many issues that influence the spectrum. Based on the studies described above, reduction of 4-NTP, identification of the reaction product is slowed down by the strong wavelength, pH, and substrate-dependency of the SERS spectrum of 4-ATP. Its SERS spectrum is usually remarkably different from its normal, neat Raman spectrum. This phenomenon has been the subject of many studies,<sup>92</sup> the amino functionality does not result in a characteristic Raman peak, and the most prominent vibrational bands are at 1087 and 1593  $\text{cm}^{-1}$ , respectively belonging C-S stretching and C-C stretching. Adsorbed onto Ag SERS substrates, vibrations at 1140, 1390 and 1435  $\text{cm}^{-1}$  appear, and as shown here, the intensity of these peaks depends on the excitation wavelength. However, since an article by Huang et al<sup>92</sup>, the formation of DMAB on SERS substrates is now a plausible explanation for these intense SERS bands, the normal spectrum of DMAB is shown alongside that of 4-ATP. As azo-functionalities are easily polarized, they result in strong bands in a Raman spectrum, in this case at 1140, 1393 and 1442

$\text{cm}^{-1}$ . It is interesting to note that the spectral features at 1140, 1390 and 1440  $\text{cm}^{-1}$  have only been observed for molecules with nitrogen-functionality<sup>93</sup>.

A highly SERS active Au-Ag alloy gradient was successfully achieved by using bipolar electrodeposition (BPE) technique. Alloy deposited on the cathodic pole of the surface with different composition of silver and gold. This gradient was screened by surface enhancement of raman spectroscopy (SERS). 4-NTP (nitrothiophenol) was used as raman probe here. The reduction of 4 nitrothiophenol (4-NTP) is much described for investigation with SERS. The four reaction mechanisms are: chemical, photo-chemical, electrochemical, and photo-catalytic reduction, which have all been examined for p-nitrothiophenol. However, the use of SERS as a characterization technique for this reduction mechanisms must be done with care, to either avoid or quantify the convolution between reaction and measurement. 4-NTP is the ideal reactant for application in SERS, as it readily adsorbs onto metal surfaces, and thereby places itself directly into the hotspots.

## References

1. Landolt, D. *J. Electrochem. Soc.* **2002**, *149*, S9–S20.
2. Gamburg, Y.D.; Zangari, G. *Springer*: New York, NY, USA, **2011**.
3. Dini, J.W. *Noyes Publications*: Park Ridge, NJ, USA, **1993**.
4. Schlesinger, M.; Paunovic, M. *John Wiley & Sons*: Hoboken, NJ, USA, **2011**.
5. Plieth, W. *Electrochemistry for Materials Science. Elsevier*: Amsterdam, The Netherlands, **2008**.
6. Chen, G. *Sep. Purif. Technol.* **2004**, *38*, 11–41.
7. Stein, A.; Schroden, R. C. *Curr. Opin. Solid State Mater. Sci.* **2001**, *5*, 553–564.
8. Roberts, M. *J. Mater. Chem.* **2011**, *21*, 9876–9890.
9. Zhang, S.; Conrad, Z. *Green Chem* **2002**, *4*, 376–379.
10. Endres, F.; MacFarlane, D.; Abbot, A. *Wiley VCH Verlag GmbH & Co.* **2008**.
11. van Dover, R. B.; Schneemeyer, L. F.; Fleming, R. M. *Nature* **1998**, *392*, 162–164.
12. Genzer, J.; Fischer, D. A.; Efimenko, K. *Appl. Phys. Lett.* **2003**, *82*, 266–268.
13. Julthongpiput, D.; Fasolka, M. J.; Zhang, W.; Nguyen, T.; Amis, E. J. *Nano Lett.* **2005**, *5*, 1535–1540.
14. Nicosia, C.; Krabbenborg, S. O.; Chena, P.; Huskens, J. *J. Mater. Chem. B*, **2013**, *1*, 5417–5428.
15. Krabbenborg, S. O.; Huskens, J. *Angew. Chem. Int. Ed.* **2014**, *53*, 9152–9167.

16. Dillmore, W. S.; Yousaf, M. N.; Mrksich, M. *Langmuir* **2004**, *20*, 7223-7231.
17. Clements, L. R.; Wang, P-Y.; Tsai, W-B.; Thissen, H.; Voelcker, N. H.  
*Lab Chip* **2012**, *12*, 1480-1486.
18. Fosdick, S. E.; Crooks, J. A.; Chang, B-Y.; Crooks, R. M. *J. Am. Chem. Soc.* **2010**, *132*, 9226–9227.
19. Ulrich, C.; Andersson, O.; Nyholm, L.; Björefors, F. *Angew. Chem. Int. Ed.* **2008**, *47*, 3034–3036.
20. Ramakrishnan, S.; Shannon, C. *Langmuir* **2010**, *26*, 4602–4606.
21. Ramaswamy, R.; Shannon, C. *Langmuir* **2011**, *27*, 878–881.
22. Plummer, S. T.; Wang, Q.; Bohn, P. W.; Stockton, R.; Schwartz, M. A. *Langmuir*, **2003**, *19*, 7528–7536.
23. Wan, A. M. D.; Schur, R. M.; Ober, C. K.; Fischbach, C.; Gourdon, D.; Malliaras, G. G. *Adv. Mater.* **2012**, *24*, 2501–2505.
24. Isaksson, J.; Robinson, N. D.; Berggren, M. *Thin solid films* **2006**, *515*, 2003-2008.
25. Collins, B. E.; Dancil, K.-P.S.; Abbi, G.; Sailor, M. J. *Adv. Funct. Mater.* **2002**, *12*, 187-191.
26. Carreon-Gonzalez, C. E.; Medina, J. T.; Piraux, L.; Encinas, A. *Nano Lett.* **2011**, *11*, 2023–2027.
27. Whitehead, J. A.; Lawrence, G. A.; McCluskey, A. *Green Chem.* **2004**, *6*, 313-315.
28. Backhurst, J. R.; Coulson, J. M.; Goodridge, F; Plimley, R. E.; Fleischmann, M. J. *Electrochem. Soc.* **1969**, *116*, 1600 – 1607.

29. Fleischmann, M.; Oldfield, J. W. *J. Electroanal. Chem Inter. Electrochem.* **1971**, *29*, 211 – 230.
30. Goodridge, F.; King, C. J. H.; Wright, A. R. *Electrochim. Acta* **1977**, *22*, 347 – 352.
31. Goodridge, F.; King, C. J. H.; Wright, A. R. *Electrochim Acta* **1977**, *22*, 1087 – 1091.
32. Plimley, R. E.; Wright, A. R. *Chem. Eng. Sci.* **1984**, *39*, 395 – 405.
33. Fleischmann, M; Ghoroghchian, J.; Rolison, D.; Pons, S. *J. Phys. Chem.* 1986, *90*, 6392 – 6400.
34. Mavr, F.; Anand, R. K.; Laws, D. R.; Chow, K.-F.; Chang, B.-Y.; Crooks, J. A.; Crooks, R. M. *Anal. Chem.* **2010**, *82*, 8766–8774.
35. Loget, G.; Kuhn, A. *Anal. Bioanal. Chem.* **2011**, *400*: 1691-1704.
36. Chang, B.-Y.; Crooks, J. A.; Chow, K.-F.; Mavr, F.; Crooks, R. M. *J. Am. Chem Soc.* **2010**, *132*, 15404–15409.
37. Bradley, J.C.; Chen, H. M.; Crawford, J.; Eckert, J.; Ernazarova, K.; Kurzeja, T.; Lin, M.; McGee, M.; Nadler, W.; Stephens, S. G. *Nature* **1997**, *389*, 268–271.
38. Bradley, J.-C.; Ma, Z.; Stephens, S. G. *Adv. Mater.* **1999**, *11*, 374–378.
39. Wei, W.; Xue, G.; Yeung, E. S. *Anal. Chem.* **2002**, *74*, 934–940.
40. Anand, R. K.; Sheridan, E.; Hlushkou, D.; Tallarek, U.; Crooks, R. M. *Lab Chip* **2011**, *11*, 518-527.
41. Laws, D. R.; Hlushkou, D.; Perdue, R. K.; Tallarek, U.; Crooks, R. M. *Anal. Chem.* **2009**, *81*, 8923–8929.

42. Sheridan, E.; Knust, K. N.; Crooks, R. M. *Analyst* **2011**, *136*, 4134–4137.
43. Klett, O.; Nyholm, L. *Anal. Chem.* **2003**, *75*, 1245–1250.
44. Keddam, M.; N\_ova, X. R.; Puga, B.; Vivier, V. *Eur. J. Environ. Civil Eng.* **2011**, *15*, 1097–1103.
45. Fosdick, S. E.; Crooks, R. M. *J. Am. Chem. Soc.* **2012**, *134*, 863–866.
46. Chang, B. Y.; Mavr, F.; Chow, K. F.; Crooks, J. A.; Crooks, R. M. *Anal. Chem.* **2010**, *82*, 5317–5322.
47. Steele, B. C. H.; Heinzl, A. *Nature* **2001**, *414*, 345 – 352.
48. Hermann, A.; Chaudhuri, T.; Spagnol, P. *Int. J. Hydrogen Energy* **2005**, *30*, 1297 – 1302.
49. Amatore, C.; Brown, A. R.; Thouin, L.; Warkocz, J. *Comptes Rendus de l'Academie des Sciences Series IIC Chemistry* **1998**, *1*, 509 – 515.
50. Loget, G.; Kuhn, A. *RSC* **2012**, *11*, 71–103.
51. Duval, J. F. L.; Minor, M.; Cecilia, J.; van Leeuwen, H. P. *J. Phys. Chem. B* **2003**, *107*, 4143-4155.
52. Klett, O.; Nyholm, L. *Anal. Chem.* **2003**, *75*, 1245-1250.
53. Bard, A. J., *Electrogenerated Chemiluminescence*. *CRC Press* **2004**.
54. Richter, M. M. *Chem. Rev.* **2004**, *104*, 3003-3036.
55. Arora, A.; Eijkel, J. C. T.; Morf, W. E.; Manz, A., *Anal. Chem.* **2001**, *73*, 3282- 3288.

56. Inagi, S.; Ishiguro, Y.; Atobe, M.; Fuchigami, T. *Angew. Chem. Int. Ed.* **2010**, *49*, 10136-10139.
57. Ishiguro, Y.; Inagi, S.; Fuchigami, T. *Langmuir* **2011**, *27*, 7158-7162.
58. Smekal, A. *Naturwissenschaften.* **1923**, *11*, 873-875.
59. Lansberg, G.; Mandelstam, L. *Naturwissenschaften.* **1928**, *16*, 257.
60. Raman, C. V. *Indian J. Phys.* **1928**, *2*, 387.
61. Raman scattering processes, illustration, viewed 8 september 2016, <http://bwtek.com/raman-theory-of-raman-scattering/>
62. Fleischmann, M.; Hendra, P. J. and McQuillan, A. J. *Chem. Phys. Lett.* **1974**, *26*, 163-166.
63. Jeanmaire, D. L. Van Duyne, R. P. *J. Electroanal. Chem.* **1977**, *84*, 1-20.
64. Albrecht, M. G. and Creighton, J. A. *J. Am. Chem. Soc.* **1977**, *99*, 5215-5217.
65. Champion, A. and Kambhampati, P. *Chem. Soc. Rev.* **1998**, *27*, 241-250.
66. Moskovits, M. *Rev. Mod. Phys.* **1985**, *57*, 783-826.
67. Natan, M. J. *Faraday Discuss.* 2006, *132*, 321-328.
68. Su, Q.; Ma, X.; Dong, J.; Jiang, C. and Qian, W. *ACS Appl. Mater. Interfaces* **2011**, *3*, 1873-1879.
69. Zheng, J.; Jiao, A.; Yang, R.; Li, H.; Li, J.; Shi, M.; Ma, C.; Jiang, Y.; Deng, L. Tan, W. *J. Am. Chem. Soc.* **2012**, *134*, 19957-19960.
70. Jiang, J.; Bosnick, K.; Maillard, M.; Brus, L. *J. Phys. Chem. B* **2003**, *107*, 9964-9972.

71. Ren, B., Liu, G., Lian, X-B.; Yang, Z-L.; Tian, Z-Q. *Anal Bioanal Chem* **2007**, 388, 29–45.
72. Kim, H.; Kosuda, K. M.; Van Duynea, R. P.; Stair, P. C. *Chem. Soc. Rev.* **2010**, 39, 4820–4844.
73. Leung, L-W. H.; Weaver, M. J. *J. Am. Chem. Soc.* **1987**, 109, 5113-5119.
74. Solla-Gullón, J.; Gómez, R.; Aldaz, A.; Pérez, J. M. *Electrochem. Commun.* **2008**, 10, 319–322.
75. Scheijen, F. J. E.; Beltramo, G. L.; Hoepfener, S.; Housmans, T. H. M.; Koper, M. T. M.; *J. Solid State Electrochem.* **2007**, 12, 483–495.
76. Gómez, R.; Solla-Gullón, J.; Pérez, J. M.; Aldaz, A. *J. Raman Spectrosc.* **2005**, 36, 613–622.
77. Gómez, R.; Pérez, J. M.; Solla-Gullón, J.; Montiel, V.; Aldaz, A. *J. Phys. Chem. B* **2004**, 108, 9943–9949.
78. Matsuda, N.; Yoshii, K.; Ataka, K-I.; Osawa, M.; Matsue, T.; Uchida, I. *Chem. Lett.* **1992**, 1385–1388.
79. Barltrop, J. A.; Bunce, N. J. *J. Chem. Soc. C: Org.* **1968**, 1467–1474.
80. Yang, X. M.; Tryk, D. A.; Ajito, K.; Hashimoto, K.; Fujishima, A. *Langmuir*, **1996**, 12, 5525–5527.
81. Ren, X.; Tan, E.; Lang, X.; You, T-T.; Jiang, L.; Zhang, H.; Yin, P.; Guo, L. *Phys. Chem. Chem. Phys.* **2013**, 15, 14196–14201.
82. Joseph, V.; Engelbrekt, C.; Zhang, J.; Gernert, U.; Ulstrup, J.; Kneipp, J. *Angew. Chem. Int. Ed.* **2012**, 51, 7592–7596.

83. Liu, R.; Liu, J-F.; Zhang, Z-M.; Zhang, L.-Q.; Sun, J-F.; Sun, M-T; Jiang, G-B. *J. Phys. Chem. Lett.* **2014**, *5*, 969–975.\
84. Xie, W.; Herrmann, C.; Kömpe, K.; Haase, M.; Schlücker, S. *J. Am. Chem. Soc.* **2011**, *133*, 19302–19305.
85. Huang, J.; Zhu, Y.; Lin, M.; Wang, Q.; Zhao, L.; Yang, Y.; Yao, K. X.; Han, Y. *J. Am. Chem. Soc.* **2013**, *135*, 8552–8561.
86. Xie, W.; Walkenfort, B.; Schlücker, S. *J. Am. Chem. Soc.* **2013**, *135*, 1657–1660.
87. Yang, X. M.; Tryk, D. A.; Ajito, K.; Hashimoto, K.; Fujishima, A. *Langmuir* **1996**, *12*, 5525–5527.
88. Sun, S.; Birke, R. L.; Lombardi, J. R.; Leung, K. P.; Genack, A. J. *J. Phys. Chem.* **1988**, *92*, 5965–5972.
89. Han, S. W.; Lee, I.; Kim, K. *Langmuir* **2002**, *18*, 182–187.
90. Dong, B.; Fang, Y.; Chen, X.; Xu, H.; Sun, M. *Langmuir* **2011**, *27*, 10677–10682.
91. Kang, L.; Xu, P.; Zhang, B.; Tsai, H.; Han, X.; Wang, H-L. *Chem. Commun.* **2013**, *49*, 3389–3391.
92. Huang, Y-F.; Wu, D-Y.; Zhu, H-P.; Zhao, L-B.; Liu, G-K.; Ren, B.; Tian, Z-Q. *Phys. Chem. Chem. Phys.* **2012**, *14*, 8485–8497.
93. Kim, K.; Shin, D.; Choi, J.-Y.; Kim, K. L.; Shin, K. S. *J. Phys. Chem. C*, **2011**, *115*, 24960–24966.
94. Lantman, E. M. Van S. PhD dissertation, Utrecht University **2014**.

## **Chapter Two**

### **Bipolar Electrodeposition Of Au-Ag Alloy Gradient And Screening Of Its Electrocatalytic Property Using Surface Enhanced Raman Spectroelectrochemistry**

#### **Abstract**

The phenomenon of surface-enhanced Raman spectroscopy (SERS) is ideal for the study of heterogeneous catalysis. The experiments in this chapter show the capability of SERS as a tool to extract information on the reaction kinetics of a photo-electrocatalytic method. The reduction of 4-nitrothiophenol has been selected as a model system using green laser excitation and applying potential on catalytically active Au-Ag alloy gradient. Electrochemical reduction of 4-NTP was done here by using bipolar electrochemical cell and regular unipolar three electrode cell. Reaction kinetics were derived to describe different kinetics on one substrate. An overview is given on the analysis of the reduction of nitro aromatics and their reduction pathways. These reactions have been examined using Raman spectroscopy, and many details about the reactivity and sensitivity to chemical environment have already been reported. First-order reaction kinetics are shown to best fit the trend that the peak areas of both reactant and product follow in time. The 4-NTP signal was clearly observed and the photo-catalytic reduction is confirmed the 4,4'-dimercaptoazobisbenzene (4,4'DMAB) as an intermediate. The photo-electrocatalytic reduction of 4-nitrothiophenol (4-NTP) is easily induced during surface-enhanced Raman scattering (SERS) measurements, while the molecules readily adsorb into the hotspots.

## 2.1 Introduction:

Surface-enhanced Raman scattering (SERS) based on the electromagnetic mechanism of generation of plasmons at the surface of a rough SERS-active metal, leads to a local increase in the electric field and consequently, the Raman signal intensities. Extreme field enhancement occurs at so-called hot spots, which are nanoscale junctions like gaps between nanoparticles or sharp edges between nano structure.<sup>1</sup> Surface plasmon resonance (SPR), which comes from the collective oscillation of transfer electrons, controls the optical spectra of metal nanoparticles, making them useful for many potential applications. Plasmonic metal nanoparticles showed distinctive properties with prospective application in many areas, which consist of catalysis,<sup>2</sup> photovoltaics,<sup>3</sup> sensing,<sup>4</sup> and photo thermal therapy.<sup>5</sup> The plasmonic responses mainly depend on the type, size, configuration and the surroundings of the noble metal nanocrystals.<sup>6-8</sup> In recent times, by incorporating more than one metal into a particular particle, the plasmonic property can be considerably extended due to synergistic effect.<sup>2,9</sup> Various approaches have been investigated, targeting at the preparation of SERS-effective nanostructured metal surfaces,<sup>11</sup> such as nanoparticle dimerization, core-shell nanoparticle, three-dimensional hierarchical integration, and on-wire lithography<sup>17,18</sup> ever since the first thought of SERS 1974.<sup>10</sup> On the other hand, electroless methods<sup>12</sup>, and electrochemical methods, such as chronoamperometry<sup>13</sup> and cyclic voltammetry<sup>14</sup> have been used to achieve plasmonic nanostructures on electrode surfaces. Most of these approaches can produce SERS substrates with high-density of Raman “hot spots”, therefore enabling SERS measurements with huge enhancement factors. Nevertheless, there are some downsides with these methods, containing a multi-step process, preparation time-consuming, low yield, and it is hard to be industrialized. It is difficult to develop a simple, reproducible, and easy method for assembly nanostructures with higher SERS performance. By controlling the

composition, size, and morphology, as well as the arrangement of the metal structures, their plasmonic properties and consequently the enhancement and sensitivity of SERS can be modified.<sup>15</sup>

Le et al deposited Pd and Ag atoms on to the surfaces of Ag nanocubes for the generation of Ag@Pd-Ag nanocubes with integrated SERS and catalytic activities. They control the deposition ratio of Pd to Ag by adjusting the titrated volumes of Pd and Ag salt. They incorporate SERS and catalytic properties into a single nanocube for extremely sensitive monitoring of Pd-catalytic reactions by SERS.<sup>17</sup> Netzer et al found an easy and direct method to construct gold–silver bimetallic porous nanowires with greater SERS enhancement.<sup>18</sup> They compare those results with pristine silver nanowires, and found the SERS enhancement improved for the porous configuration of the bimetallic nanowires. Au nanoparticles have shown good catalytic activity at room temperature comparing to Ag nanoparticles. Less chemical stability and aggregation effects reduce the catalytic activity of silver nanoparticles. Ag nanoparticles have considerable stronger surface plasmon resonance than Au due to its proper electronic structure and dielectric function. Here we try to combine catalytic activity and high plasmonic activity simultaneously in one platform by using the method of bipolar electrochemistry.

Bipolar electrochemistry is a useful experimental method for the formation of compositional or chemical gradients along the surface of a wireless conductive object.<sup>12,15</sup> Oxidation and reduction reactions take place at opposite ends of a bipolar electrode without direct electrical connections to an external power supply. It is sufficient to apply an electric field, that is, a potential gradient, to the solution (low concentration of a supporting electrolyte) through two feeder electrodes connected to a DC power supply (figure 2.1). Basically, metals deposit at different potentials, and bipolar electrodes have a gradient in potential. If the bipolar method is

applied to a solution containing a combination of different metals, these will deposit at different locations along the bipolar electrode surface based on their corresponding redox potential.<sup>12</sup> A voltage,  $E_{appl}$ , is applied between two driving electrodes through the solution. Initially the potential drops exponentially near the driving electrodes and then approximately linearly in the middle of the solution as of the solution's resistance. This suggests that the potential difference between a point on the substrate and the solution will vary laterally along the surface. When the applied voltage  $E_{appl}$  is sufficiently high, faradaic reactions will be initiated at both ends of the bipolar electrode. There is a single point on the BPE where its potential equals that of the solution. This point divides the BPE into two poles; the cathodic and anodic poles. No reactions occur at this point. The potential at this point,

$$\Delta E_e = V l_e = \frac{E_{appl}}{l} l_e \quad (2.1)$$

where  $V$  is the electric field in solution and  $l$  is the distance between the driving electrodes.  $l_e$  is the length of the bipolar electrode.  $\Delta E_e$  signifies the total potential difference between the bipolar electrode and the solution over potential needed to drive two faradaic reactions occurring simultaneously on opposite poles of the bipolar electrode i.e.  $\Delta E_e = \eta_c - \eta_a$ . Note that the symbol  $\eta$  denotes a potential difference and can also be referred to as an over potential. Note that it is necessary that the reactions at both pole to occur simultaneously to maintain electro neutrality on the electrode surface. That is the electrons generated at the anodic pole due to an oxidation reaction must be consumed in a reduction process at the cathode.

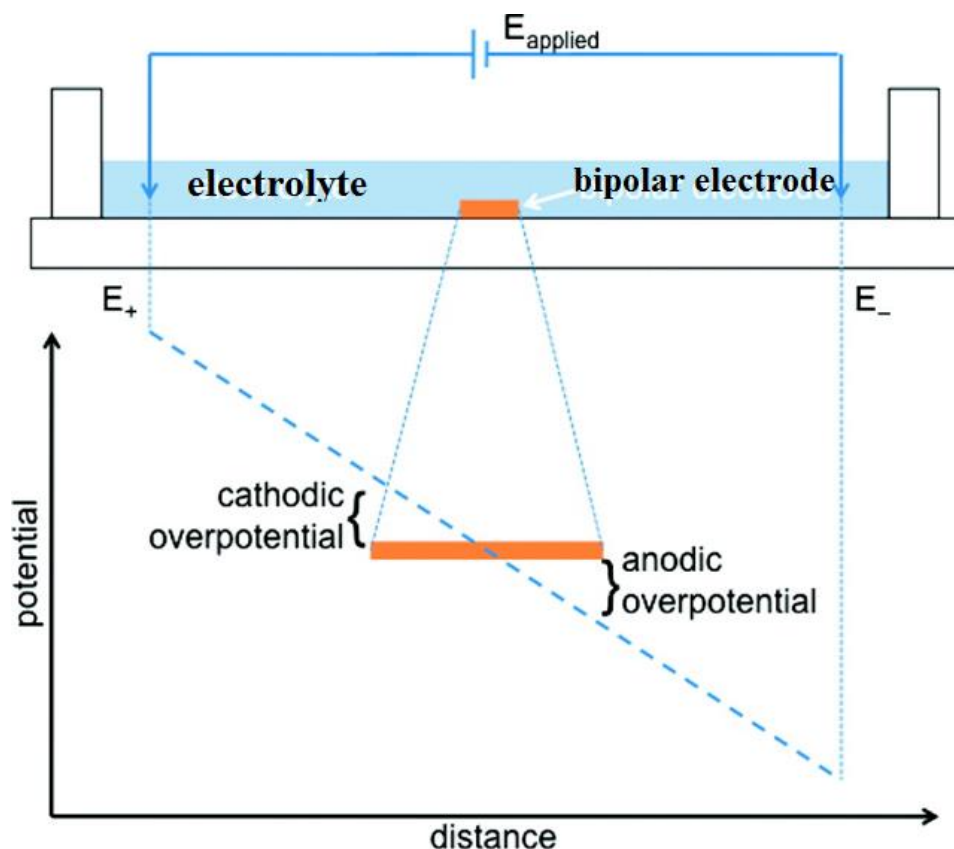
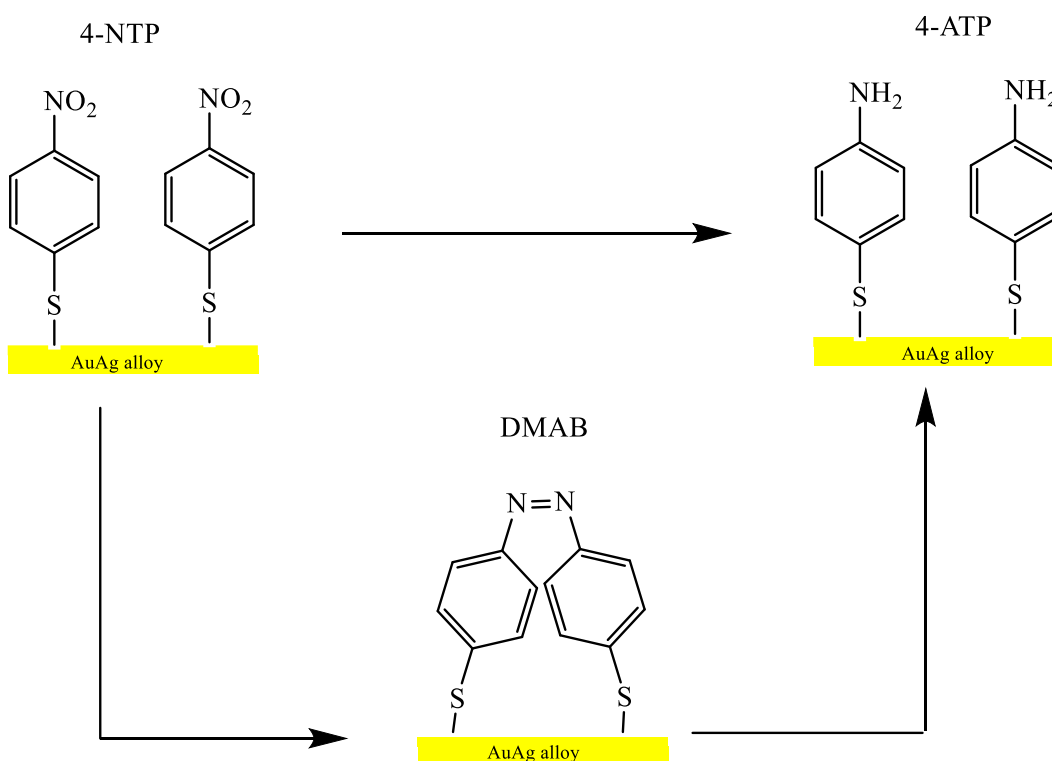


Figure 2.1: Schematic drawing of the theory of bipolar electrochemistry. A bipolar electrochemical cell consisting of two driving electrodes between which a voltage,  $E_{\text{applied}}$  is applied and a bipolar electrode (BPE) where faradaic reactions occur at both ends.<sup>20</sup>

(Reprinted with permission from Ref 20. Copyright © 2010, American Chemical Society).

In this thesis, this concept was initially explored by depositing SERS-active Au – Ag alloy gradient on a stainless steel foil from controlled mixtures of metal salts by a simple and rapid bipolar electrodeposition method. The effect of their atomic percentage on the alloy on Raman enhancement is investigated with dependence on the position along the bipolar electrode by using as a catalyst for chemisorbed 4-nitrothiophenol (4-NTP) reduction reaction as a model (scheme 2.1). This reaction was selected as a model scheme for instance 4-NTP and 4-ATP are involved in a number of reactions such as metal-catalyzed hydrogenation and surface plasmon resonance

(SPR) prompted, photo catalyzed oxidation reduction reaction (ORR). These reactions have been studied exhaustively in the past few years, and there is still a continuing argument about the principal reaction mechanisms, in particular the role of photo catalysis.<sup>19</sup> In the present study on this model reaction, plasmonic silver and gold nanostructures show excellent ability for catalytic reduction of 4-NTP. The reduction pathway for 4-NTP to 4-ATP is showing in scheme 2.1. First route is fully reduction. The second is followed by forming an intermediate azo compound and then finally reduced to 4-ATP. The reason for is aromatic nitro compounds can be selectively transformed to the corresponding aromatic azo compounds and then amino compound during SERS with applying potential.



Scheme 2.1: Reduction of 4-nitrothiophenol (4-NTP) to 4-aminothiophenol (4-ATP) and 4,4'-dimercaptoazobenzene (4,4'-DMAB)

The typical Raman band of 4-NTP is invariant over time with an excitation wavelength of 514.5 nm, indicating that 4-NTP itself is not involved in any direct photochemical reactions. However, unlike the NR spectrum, the surface-enhanced Raman scattering (SERS) spectrum was shown to be subject to change with time.<sup>20</sup> The SERS peaks of 4-NTP slowly lose their intensities, combined with the appearance of a new set of peaks. The intensity of the new peaks promptly increases, as a function of the laser-illumination time. The plasmonically generated hot electrons from the Ag substrate are the origin of this reaction.<sup>21</sup> Final products of this reaction is 4-ATP, which is an unusual molecule because its SERS spectrum depends on the type of SERS substrate and on the measurement conditions.<sup>19</sup> The electrochemical reduction of self-assembled monolayer of para nitrothiophenol on silver electrode was reported by Matsuda et al. They showed the in situ SERS spectra of this reaction.<sup>22</sup>

## 2.2 Materials and Methods:

**Chemicals:** Potassium dicyanoaurate (I)  $\text{KAu}(\text{CN})_2$  (98% ACS reagent, Aldrich Chemical Co.), Potassium dicyanoargentate  $\text{KAg}(\text{CN})_2$  (98% ACS reagent, Aldrich Chemical Co.), KCN (99.5% ACS reagent, Fisher Scientific Company), and KOH (87.1%, Fisher Scientific Company), Sodium borohydride ( $\text{NaBH}_4$ ) (99%, Fluka), 4-Nitrothiophenol (80%, Alfa Aesar), 4-Aminothiophenol (97%, Alfa Aesar), Sodium perchlorate ( $\text{NaClO}_4$ ) (100%, Sigma) were used as it was. Type 304 Stainless Steel foil used for driver electrode and bipolar electrode in bipolar electrochemical cell. Millipore-Q purified deionized (DI) water ( $18.2\text{M}\Omega/\text{cm}^3$ ) was used to make all solutions and to clean electrodes.

**Substrate Preparation:** Type 304 Stainless Steel foil, 0.25mm (0.01in) thick used for driver electrode and type 304 Stainless Steel foil, 0.1mm thick used as bipolar electrode in bipolar electrochemical cell. 25 mm long and 5mm wide stainless steel (0.1 mm) substrates were

mechanically polished with 800 grit SiC paper. Then they were cleaned by rinsing consecutively with DI water and absolute ethanol. Finally sonicated in water- Ethanol mixture for 5min. After being dried in a stream of flowing nitrogen, the clean stainless steel bipolar electrode was placed into the bipolar electrochemical cell. Driver electrodes were prepared by rinsing sequentially with distilled water, absolute ethanol, and distilled water, and were dried in a stream of flowing nitrogen.

**Electrochemistry:** All conventional (unipolar) electrochemistry measurements were performed using a standard three electrode configuration in a home-built glass cell. In all cases, we used a stainless steel working electrode (Ag-Au alloy), a Pt wire as counter electrode, and a Ag|AgCl (sat) (Bioanalytical Systems, Inc.) reference electrode. The electrochemical cell was controlled by an Epsilon electrochemistry workstation (Bioanalytical Systems, 92, Inc.).

All bipolar electrochemistry experiments were performed in a home-built single compartment glass cell using a Hewlett-Packard model 6010 regulated DC power supply to control the potential applied between two stainless steel driver electrodes separated by 3.5 cm. The electrically floating stainless steel BPE was placed symmetrically between the two stainless steel driver electrodes, as previously reported.<sup>23</sup> The three electrodes were immersed in an electrodeposition solution containing 5 mM  $\text{KAu}(\text{CN})_2$ , 5 mM  $\text{KAg}(\text{CN})_2$ , 200 mM KCN, and pH of the electrolyte adjusted by KOH (pH 12). Ag-Au alloy films were deposited by applying a voltage of 9.9 V across the driver electrodes for 1 min at room temperature. The BPE was then rinsed with DI water, dried in a stream of flowing nitrogen, and stored in a closed vial before analyzing in SEM and EDX.

**Formation of 4 nitrothiophenol (4-NTP) Self-Assembled Monolayers:** A freshly deposited Au-Ag alloy gradient was immediately immersed in a 5 mM ethanolic solution of 4-nitrothiophenol

for 15 h after washing by DI water and dried by N<sub>2</sub>. After monolayer formation, the specimen was rinsed with ethanol and dried in N<sub>2</sub> prior to analysis by confocal Raman microscopy.

### **2.3 Characterization of the Au-Ag alloy electrodeposit:**

#### **2.3.1 Scanning Electron Microscopy (SEM) and Energy Dispersive X-ray spectroscopy**

**(EDX):** SEM images of the electrodeposited Ag-Au alloy on a stainless steel bipolar electrode were acquired from a JEOL JSM- 7000F field- emission scanning electron microscope and analyzed using the EOS 7000F software package. EDX data were acquired using the Oxford X-Max energy dispersive X-ray spectrometer and were analyzed using the INCA software package.

**2.3.2 Raman spectroscopy:** Raman scattering was excited using the 514.5 nm output (ca. 20 mW) from an air-cooled argon ion laser (model 163-C42, Spectra-Physics Lasers, Inc.) and the 785 nm (300 mW) output from a wavelength-stabilized high power laser diode system (model SDL-8530, SDL Inc.). Raman measurements were acquired as a function of position along the length of the bipolar electrode and analyzed using a Renishaw inVia Raman microscope system. Raman signals were accumulated for each spectrum was 10 seconds and only a single scan was made. A 1200 lines mm<sup>-1</sup> grating was used for all measurements providing a resolution of  $\pm 1\text{ cm}^{-1}$ . The instrument was calibrated for the Raman shift by referencing to that of silicon.

After deposition of Au-Ag alloy gradient thin film it was connected as the working electrode in a conventional 3-electrode electrochemical circuit. A Pt wire was used as the counter electrode and Ag/AgCl (sat) was used as the reference electrode. All potentials given in this chapter are referred against Ag/AgCl (sat). The cell was designed to permit the coinciding collection of electrochemical and Raman spectroscopic information. The catalytic conversion of 4-NTP to 4-ATP under basic conditions was observed at a fixed applied potential using a Raman microscope

to interrogate the small area of the electrocatalyst surface. To attain this, we focused the Raman laser different position on the electrode surface. The kinetics of the catalyzed reactions was measured in situ with real-time observing SERS in 0.01M NaClO<sub>4</sub> aqueous solution.

## **2.4 Results and Discussion:**

**2.4.1 Screening the Au-Ag alloy gradients on the bipolar electrode:** To proof the existence of gradient of Au-Ag deposition, SERS spectra were recorded along the length of the bipolar electrode. As an example, the SERS intensities of chemisorbed 4-NTP were evaluated (800–1700 cm<sup>-1</sup>, figure 2.2). However, a change of intensity with a change of the Raman-active molecule is anticipated, so that this determination of the most efficient SERS active structure may have to be repeated for each specific application. SERS spectra of five regions along the bipolar electrode are shown. The intensity of the most salient Raman peak of 4-NTP at 1344 cm<sup>-1</sup>, which belongs to the NO<sub>2</sub> stretching band, is evaluated along the entire length from the cathodic end to the middle of the BE (figure 2.3). A potential gradient was applied to deposit Au-Ag alloy gradient on cathodic pole of bipolar electrode. After forming the 4-NTP self-assembled mono layer on the alloy, SERS spectra was collected. Those data plotted in figure 2.2. Six different spectra are showing there from six different region of the Au-Ag alloy gradient. A is the nearest point on cathodic edge and F is the end of the gradient. Gold deposited more than silver in cathodic area. Silver has the stronger surface plasmon resonance than gold. From 5 mm 8 mm this area is Ag rich region (D, E). That is why the highest intensity of NO<sub>2</sub> band were observed. In cathodic area deposited Au has higher thickness and roughness decrease with lower potential differences, and hence slower Au deposition rates, towards the middle of the BE (figure 2.3. B, C), which leads to a parallel decrease in the SERS intensity.

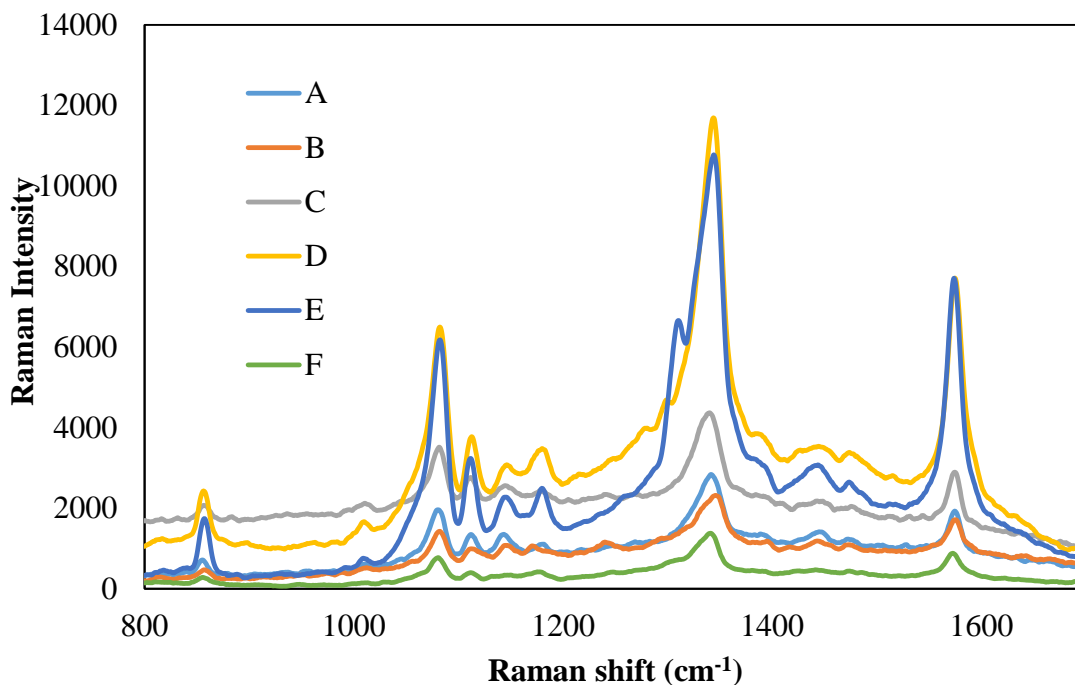


Figure 2.2: Surface enhanced raman spectra of 4-NTP at six different locations along the BE, from (A) closest to the cathodic end to F) closest to the middle towards anode.

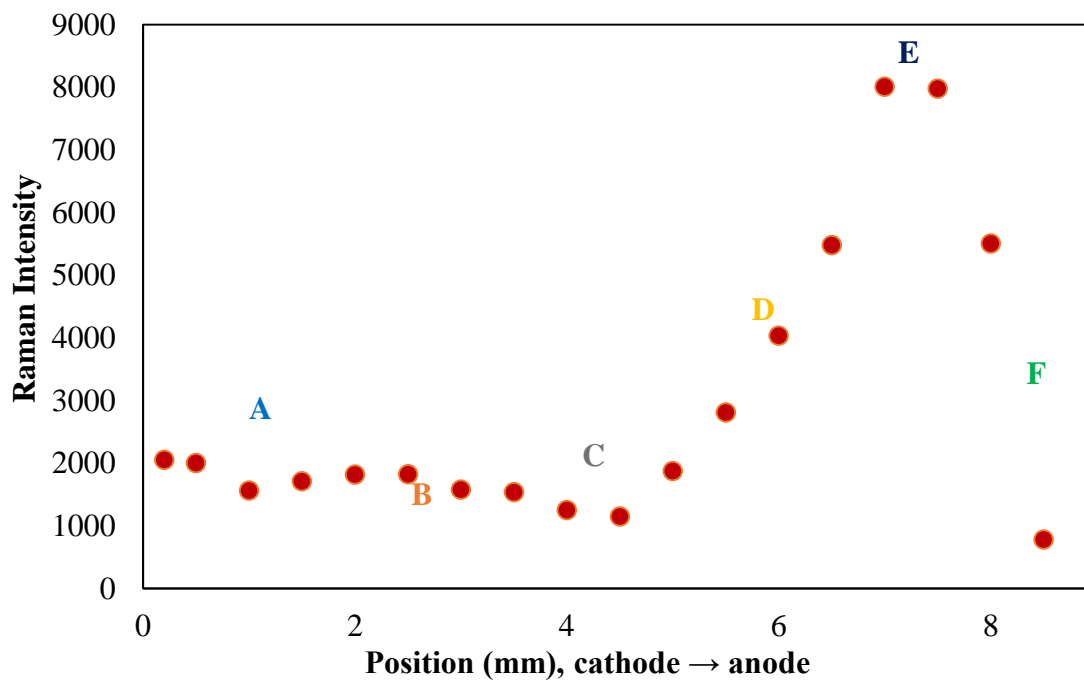


Figure 2.3: Signal intensity of the  $\text{NO}_2$  symmetrical stretching band (1344  $\text{cm}^{-1}$ ) versus the distance from the cathodic end.

Very low intensity observed near to the middle of the deposition, at a distance of more than 8 mm from the cathodic end (F) of the BE. Kayran et al deposit Au nanovoid gradient by bipolar electrodeposition. Our NO<sub>2</sub> band intensity trend ties with their results.<sup>24</sup> Figure 2.4 shows the typical SEM image of the Au-Ag alloy deposit. From EDX measurement we calculated the maximum atomic percentage of the alloy is 30% Au and 70% Ag in D area in figure 2.3. Nanoparticles size also measured by SEM, which is more than 100 nm in diameter.

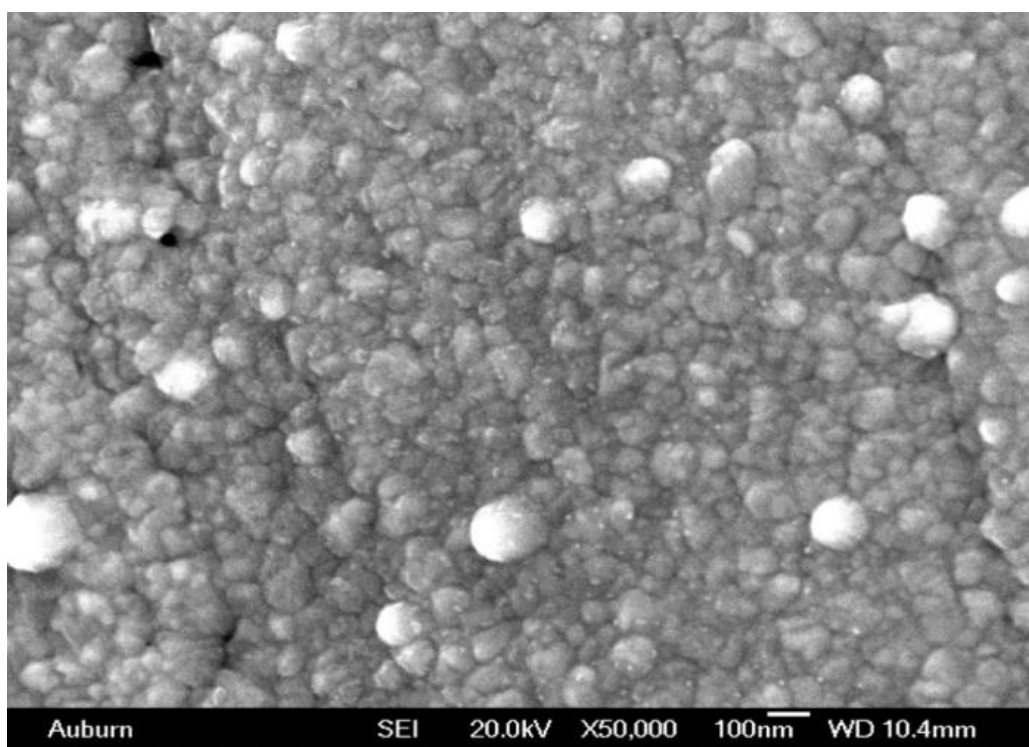


Figure 2.4: The surface morphology visualized by using SEM (scale bar=100 nm) of the Au- Ag alloy deposit.

**2.4.2 Raman and SERS assignments of 4-nitrothiophenol and 4-nitrothiophenol:** Normal Raman spectra of solid 4-aminithiophenol and 4-nitrothiophenol (from a commercial grade, not

the product from catalytic reduction of 4-NTP) showed in figure 2.5. All bands are listed in table 2.1.

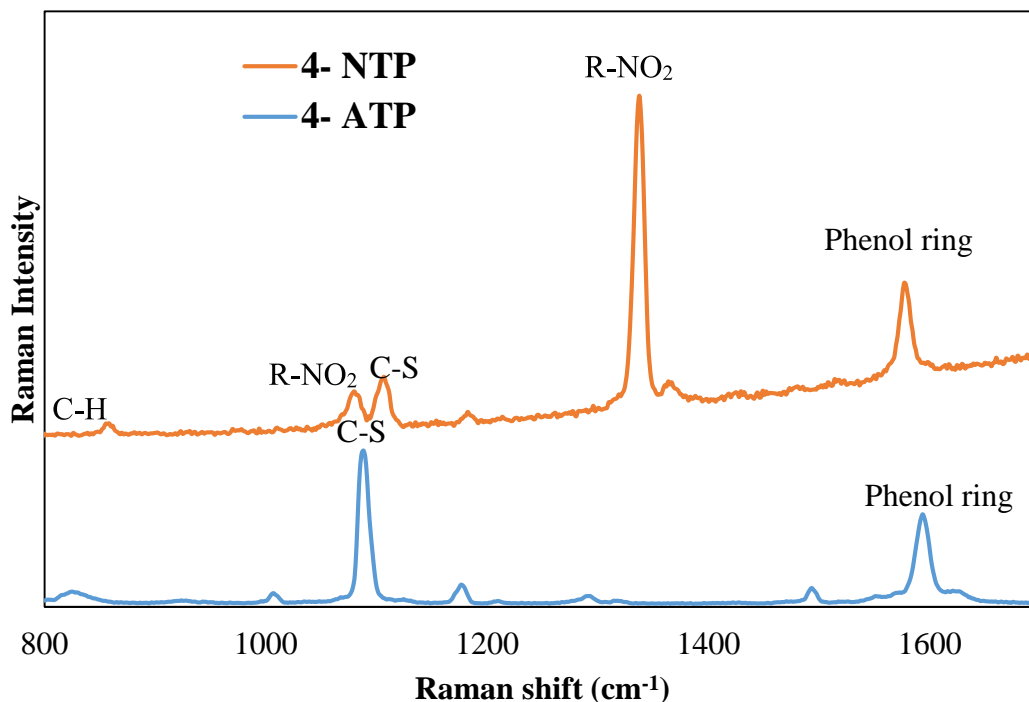


Figure 2.5: Normal Raman spectra of solid 4-aminithiophenol (4-ATP) and 4-nitrothiophenol (4-NTP).

4-NTP		4-ATP		4,4'-DMAB	Assignment
Ordinary Raman	SERS	Ordinary Raman	SERS	SERS	
cm <sup>-1</sup>					
854	859				C-H wagging
1107	1112	1080	1078		C-S stretching
1080	1108				O-N-O stretching
		1178	1182		C-H plane bending
1336	1345				O-N-O stretching
1578	1571	1594	1591		Phenol ring mode
				1390	-N=N-
				1440	C-H bending mode (in plane)
			1494	1145	C-N symmetric stretching

Table 2.1: The SERS and ordinary Raman shifts of 4-NTP and 4-ATP and their assignments.<sup>8,25</sup>

SERS spectra of 4-NTP and 4-ATP adsorbed on the Ag-Ag alloy gradients, Au foil and Ag foil substrate (figure 2.6 and 2.7). The spectra were taken under the same experimental conditions. 4-NTP is more Raman active than 4-ATP. For that reason, the intensity of the band at  $1571\text{ cm}^{-1}$  for 4-NTP is higher than the band at  $1589\text{ cm}^{-1}$  for 4-ATP.

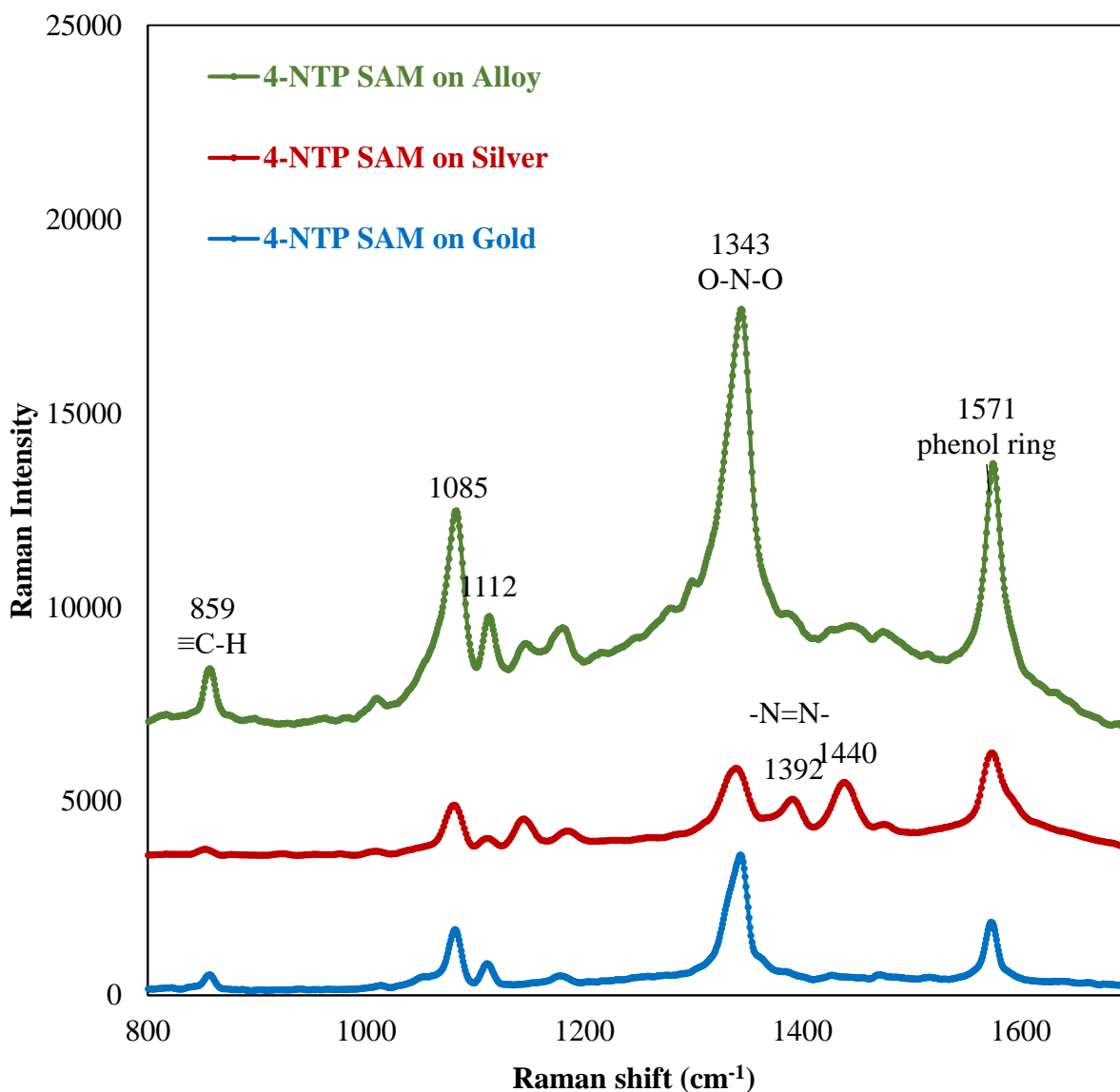


Figure 2.6: SERS spectra 4-nitrothiophenol (4-NTP) self-assembled monolayer on different surface.

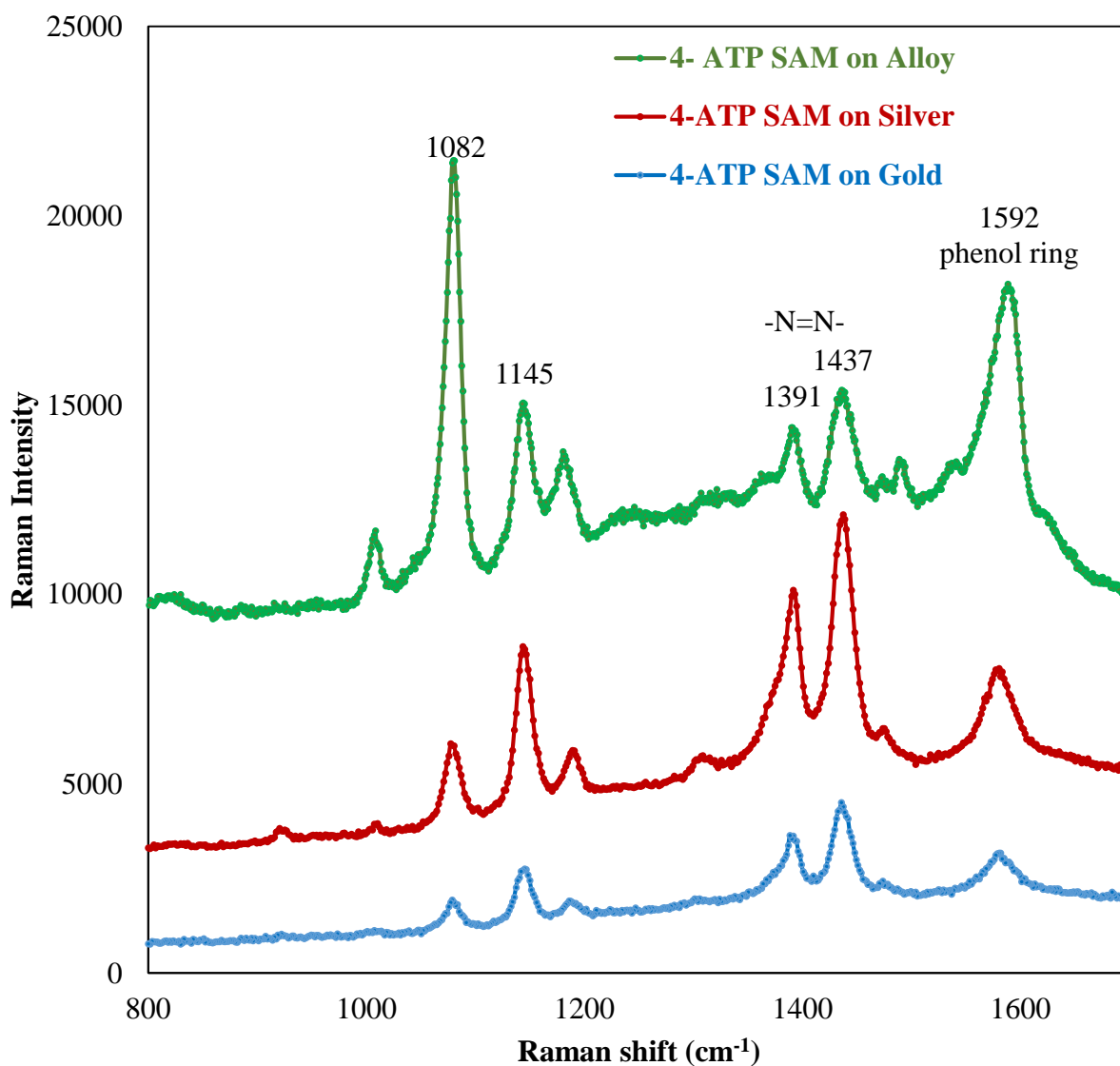


Figure 2.7: SERS spectra 4-aminothiophenol self-assembled monolayer on different surface.

SERS spectra of 4-NTP and 4-ATP self-assembled monolayer depends on many factors. Substrate and the laser type are two of them. For silver substrate both 4-NTP and 4-ATP is showing -N=N- stretching mode at  $1390 \text{ cm}^{-1}$  and C-H bending mode (in plane) at  $1440 \text{ cm}^{-1}$ . These are both in 4,4'-DMAB SERS spectrum.<sup>26</sup>

**2.4.3 In situ monitoring of catalytic chemical reduction with SERS:** Since the synchronized deposition of Ag and Au have been established by (EDS and SEM), it is essential to inspect the in situ real-time monitoring surface enhanced raman scattering of catalytic reaction with Au-Ag alloy gradient. Due to the collaborations of the metal components, the plasmonic activity of Ag increases however catalytically active Au is present at the same time. In comparison, no catalytic activity is detected without the introduction of Ag. To reveal the catalytic and SERS activity of Au-Ag alloy gradients, a proper platform for this proof of thought study and practical applications is essential. Here, we investigate the reduction of aromatic nitro compounds (R-NO<sub>2</sub>) to the amino compounds (R-NH<sub>2</sub>) at room temperature which would be useful for environment control and other application.

A 4-NTP (5mM) molecular self-assembled monolayer (SAM) was formed on the surface of Au-Ag alloy gradient by immersing at room 4-NTP ethanolic solution at room temperature. Then the BPE (Au-Ag alloy) was washed for 2 times with ethanol and water. After drying the BPE with a flow of N<sub>2</sub>, 100  $\mu$ l of 0.1 M NaBH<sub>4</sub> was added on to the BPE in a glass Petri dish at room temperature. The kinetics of the catalyzed reactions was measured in situ with real-time monitoring SERS. The time-resolved SERS observing can increase quantitative awareness into the kinetics and mechanism learning of alloy-catalyzed reaction. Au-Ag alloy gradient deposit-catalyzed reaction through the reduction of 4-NTP by NaBH<sub>4</sub> was chosen as a model reaction, which will be compared to the catalytic activity of Ag and Au.<sup>25</sup> Intrinsic reaction mechanism and kinetics can be calculated in real time by detecting SERS signals from the monolayer molecule pre adsorbed on the surface of alloy. Thus, the identification of temporary intermediates during the reaction processes became possible. To prepare the samples for SERS measurement, alloy film was immersed in ethanolic solution of 4-NTP at room temperature for 15 hours which formed a 4-

NTP molecular SAM on the surface of gradients. The SAM of 4-NTP on the surface of alloy gradients go through a two-step reduction route upon the adding of NaBH<sub>4</sub> at room temperature. The final product is 4-aminothiophenol. The SERS spectrum of 4-NTP monolayer shows four characteristic vibrational bands at 854, 1081, 1344, and 1571 cm<sup>-1</sup>, which correspond to C–H wagging, C–S stretching, O–N–O stretching, and the phenyl ring modes, respectively.<sup>26</sup> As the reaction proceeded, strong Raman signal at 1343 cm<sup>-1</sup> decreased gradually, and new vibrational Raman signals of the intermediate at 1145, 1391, and 1433 cm<sup>-1</sup> appeared, which were due to C–N symmetric stretching, N=N stretching, and C–H in-plane bending modes of 4, 4'-dimercaptoazobenzene (4, 4'-DMAB), respectively.<sup>27</sup> With a further increase of reaction time (from bottom to top in figure 2.9), the intensity of SERS signal from 4, 4'-DMAB in the beginning increases and then decreases, indicating that NO<sub>2</sub> groups start to be reduced. The band arising from C–H wagging and phenyl ring modes of 4-NTP at 854 and 1571 cm<sup>-1</sup> also decreases progressively, associated with the intensity of a fresh band at 1595 cm<sup>-1</sup> increases and trace of a supplementary characteristic signal of 4-ATP at 1489 cm<sup>-1</sup> appears. After 15 minutes only two band exist, that is 1087 cm<sup>-1</sup> for C-S stretching and 1597 cm<sup>-1</sup> for Phenyl ring mode. Which is Thus, we can generate that the final reaction product is 4-ATP for the reduction of 4-NTP by NaBH<sub>4</sub>, which demonstrates the catalytic activity of Au-Ag alloy gradient for in situ chemical reduction monitoring. On the other hand, different results were detected from reaction system that enclosed Au or Ag NPs. For SAM of 4-NTP on Au nanoparticles, the SERS spectrum with no noticeable change was observed under the similar conditions with the catalytic reaction of Au-Ag alloy nanoparticles.<sup>25</sup> Clearly, the catalytic activity of Au-Ag alloy NPs is superior than the regular monometallic Au or Ag NPs. This may be caused by the intense increase of the catalytic activity when alloying of silver with gold. The electromagnetic enhancements in the junction between a Ag nanoparticle and the Ag

film at an incident wavelength of 514.5 nm is very strong than gold film at 514.5 nm. For this reason, the stronger electromagnetic field enhancement delivered by the local surface plasmon can significantly reduce the reaction time. Au NPs are a minor and promising catalyst for reduction of 4-nitrobenzethiol.

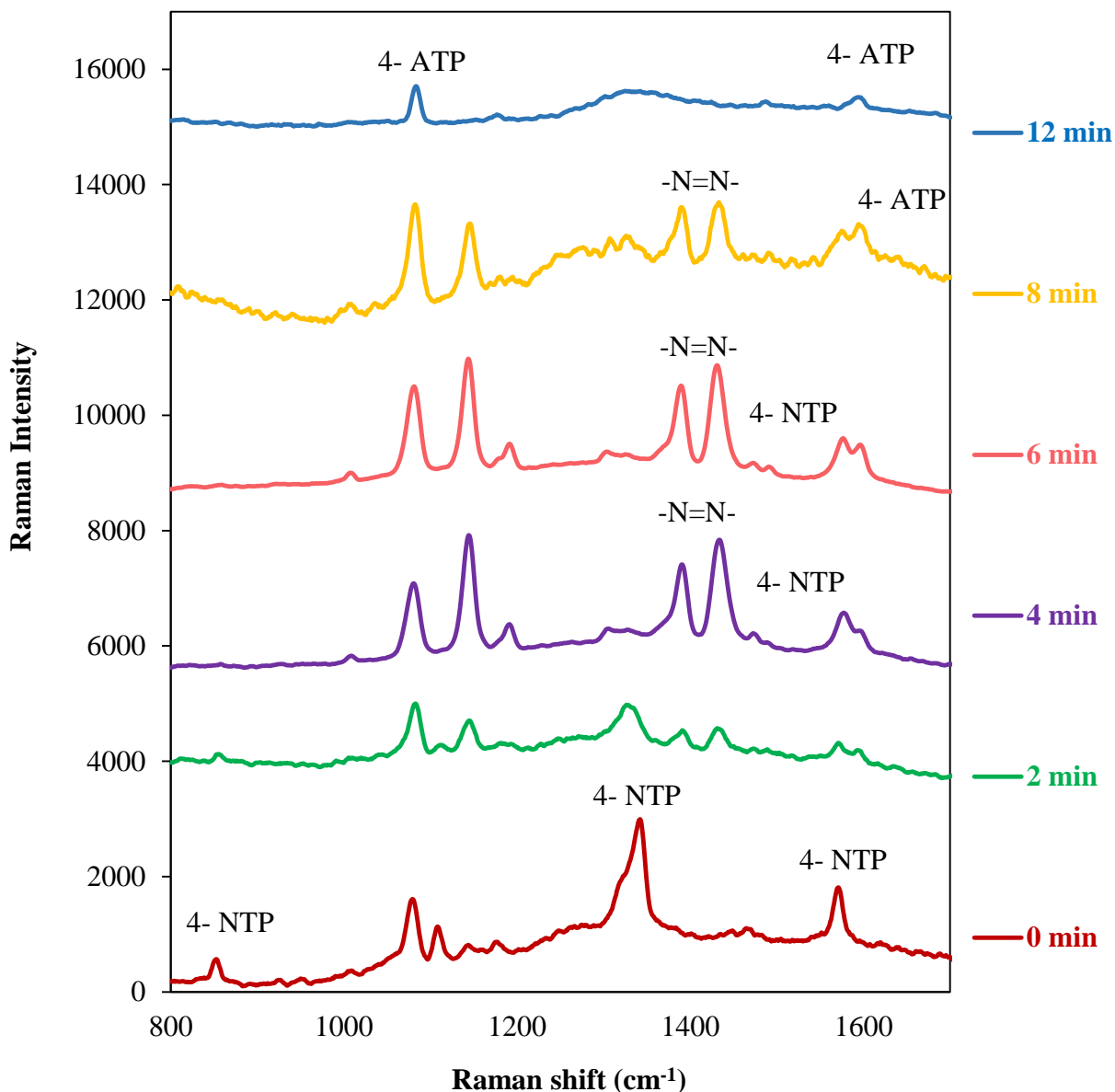


Figure 2.9: SERS spectra recorded for the period of the reduction of 4-NTP to 4ATP catalyzed by the Au-Ag alloy gradient in the occurrence of NaBH<sub>4</sub>. The R-NO<sub>2</sub> and R-NH<sub>2</sub> represent the 4-NTP and 4-ATP, correspondingly.

**2.4.4 In situ monitoring of electrochemical catalytic reduction with SERS:** 4-NTP (5mM) molecular self-assembled monolayer (SAM) was formed on the surface of Au-Ag alloy gradient by immersing at room 4-NTP ethanolic solution at room temperature. Then the BPE (Au-Ag alloy) was washed for 2 times with ethanol and water. After drying the BPE with a flow of N<sub>2</sub>, it was placed in a home built three electrode cell (unipolar) as working electrode and bipolar cell set up as a bipolar electrode between two driver electrode separated by 35 mm in a glass Petri dish at room temperature. The kinetics of the catalyzed reactions was measured in situ with real-time monitoring SERS.

Figure 2.10 shows a typical cyclic voltammogram of 4-nitrothiophenol adsorbed on alloy in 0.1 M NaClO<sub>4</sub> aqueous solution, at 50 mV/s scan rate to find the characteristic CV peak. Au-Ag alloy gradient was used as working electrode here with platinum counter electrode and Ag|AgCl (sat) reference electrode. A reduction wave (blue) is observed around -0.87 V for the cathodic scan. Corresponding oxidation peak is not observed for anodic scan. Next, a second scan was carried out to ensure an adequate supply of H<sup>+</sup> ions for the complete electrochemical reduction of the NO<sub>2</sub> to NH<sub>2</sub> groups. No peaks are observed for the second (red) and additional scan (not showing) as in the figure. This value is equivalent with the self-assembled monolayer of 4-nitrothiophenol on silver electrode.<sup>22-28</sup> Supposed that NO<sub>2</sub> group is reduced to NH<sub>2</sub> by a six electron reduction method, the quantity of adsorbed 4-NTP is calculated  $1.59 \times 10^{-8} \text{ M cm}^{-2}$ . Figure 2.11 shows the SERS spectra of Au-Ag electrode modified with 4-nitrothiophenol. The spectra were obtained by synchronizing the controlled potential electrolysis. Three electrode cell was placing under the raman microscope and focused in to alloy area. Same set up used to obtain data for figure 2.10 and 2.11.

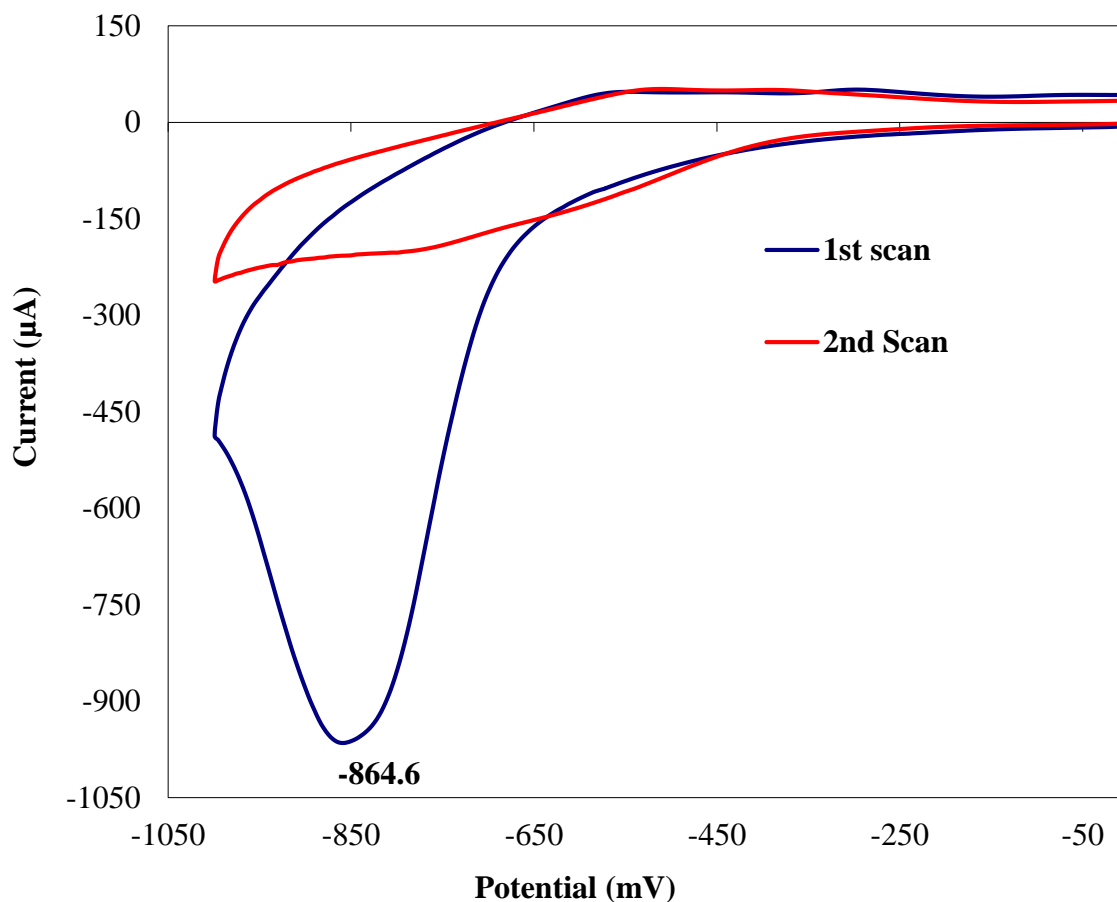


Figure 2.10: Cyclic voltammogram of Au-Ag (alloy gradients) electrode modified with 4-nitrothiophenol in 0.1 M NaClO<sub>4</sub>.

At 0.0 V SERS spectra is showing all main 4 bands which represent the nitrothiophenol. Those are 855 cm<sup>-1</sup> (O–N–O stretching), 1081 cm<sup>-1</sup> (C–S stretching), 1344 cm<sup>-1</sup> (O–N–O stretching), and 1574 cm<sup>-1</sup> (phenol-ring mode). After increasing the potential to -0.9V, 1574 cm<sup>-1</sup>, 1344 cm<sup>-1</sup> and 855 cm<sup>-1</sup> peak disappeared. A new peak arise for phenol-ring mode at 1595 cm<sup>-1</sup>. This is the characteristics band for 4- ATP. Perchlorate band appeared at 1124 cm<sup>-1</sup>. Two extra peak observed for 0.0 V at 1390 cm<sup>-1</sup> and 1440 cm<sup>-1</sup>. These are the intermediate product 4,4'- DMAB. Which indicates the green laser initiated the photo reduction of 4- NTP on silver particles of the gradients.

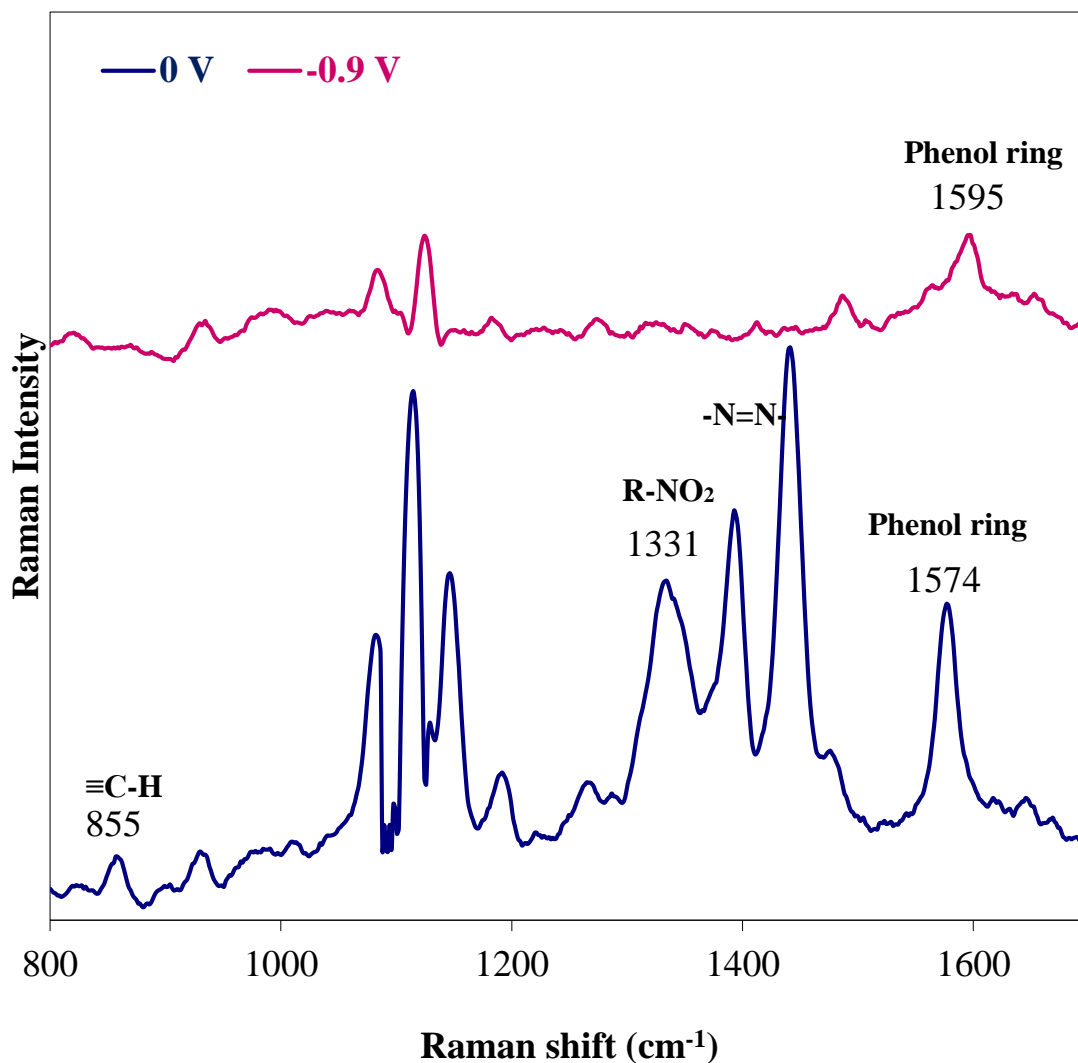


Figure 2.11: In situ SERS spectra of 4 NTP SAM on an Ag- Au alloy electrode in 0.1 M NaClO<sub>4</sub> aqueous solution in a three electrode cell. The spectrum was obtained at alloy area of the cathodic pole before (blue) and after (pink) application of a voltage of -0.9 V across the electrolyte.

**2.4.5 Evaluation of Reaction Gradients on Bipolar Electrodes Using SERS:** The use of SERS to visualize reaction gradients on bipolar electrodes was demonstrated for Au-Ag substrates. Figure 2.12 shows in situ surface enhanced raman spectra collected at the cathodic edge of an Au bipolar electrode, previously modified with a 4 NTP SAM, before and after applying the voltage across a 0.01M NaClO<sub>4</sub> containing the bipolar electrode. Figure 2.12 showed the different SERS

spectra of Au- Ag alloy (BPE) modified with self-assembled monolayer 4-NTP at different potential. The spectra were obtained with a DC power supply. Potential applied across the two driver electrode starts from 0.0 V up to 7 V. Excitation source 514.5 nm laser was used. Data collection time was 30 second for one scan. The collection of SERS spectra at different potential at  $V = 0$ , figure 5 shows the SERS spectrum of 4-NTP with four representative vibrational bands at  $857\text{ cm}^{-1}$  (O–N–O stretching),  $1081\text{ cm}^{-1}$ (C-S stretching).  $1344\text{ cm}^{-1}$  (O–N–O stretching), and  $1574\text{ cm}^{-1}$  (phenol-ring mode).<sup>12</sup> By observing the SERS peak at  $1344\text{ cm}^{-1}$  (the benzene ring mode of 4-NTP), we found that its intensity remains unchanged up to 4 V and gradually decreased with increasing potential. This is most likely due to the reduction of 4-NTP was initiated only when the electrochemical potential was stepped to the appropriate value (each spectrum was taken when the cell current decayed to zero).  $1574\text{ cm}^{-1}$  peak start decreasing from 5 V and completely disappear with applying 7 V across the driver electrode. As the potential increased the intensities of other  $\text{NO}_2$  bands 857 and 1087 decreased progressively with the concomitant emergence of a new band corresponding to the phenol-ring mode of 4-ATP at  $1596\text{ cm}^{-1}$ . It is better noting that the other vibrational modes shown in the SERS spectra can also be assigned to those shown in the Raman spectra of 4-NTP and 4-ATP (Table 2.1). New vibrational Raman signals of the intermediates are at  $1147\text{ cm}^{-1}$ ,  $1394\text{ cm}^{-1}$ , and  $1444\text{ cm}^{-1}$ . They disappear from 5 V. All three peaks  $857\text{ cm}^{-1}$ ,  $1344\text{ cm}^{-1}$ ,  $1574\text{ cm}^{-1}$  completely disappear at 7 V. That means reduction of nitrothiophenol has been done completely. It is well established that SERS originates from several mechanisms. Enhancement of Raman Intensity associated with the charge transfer between metal and molecule is one of the most important mechanism.

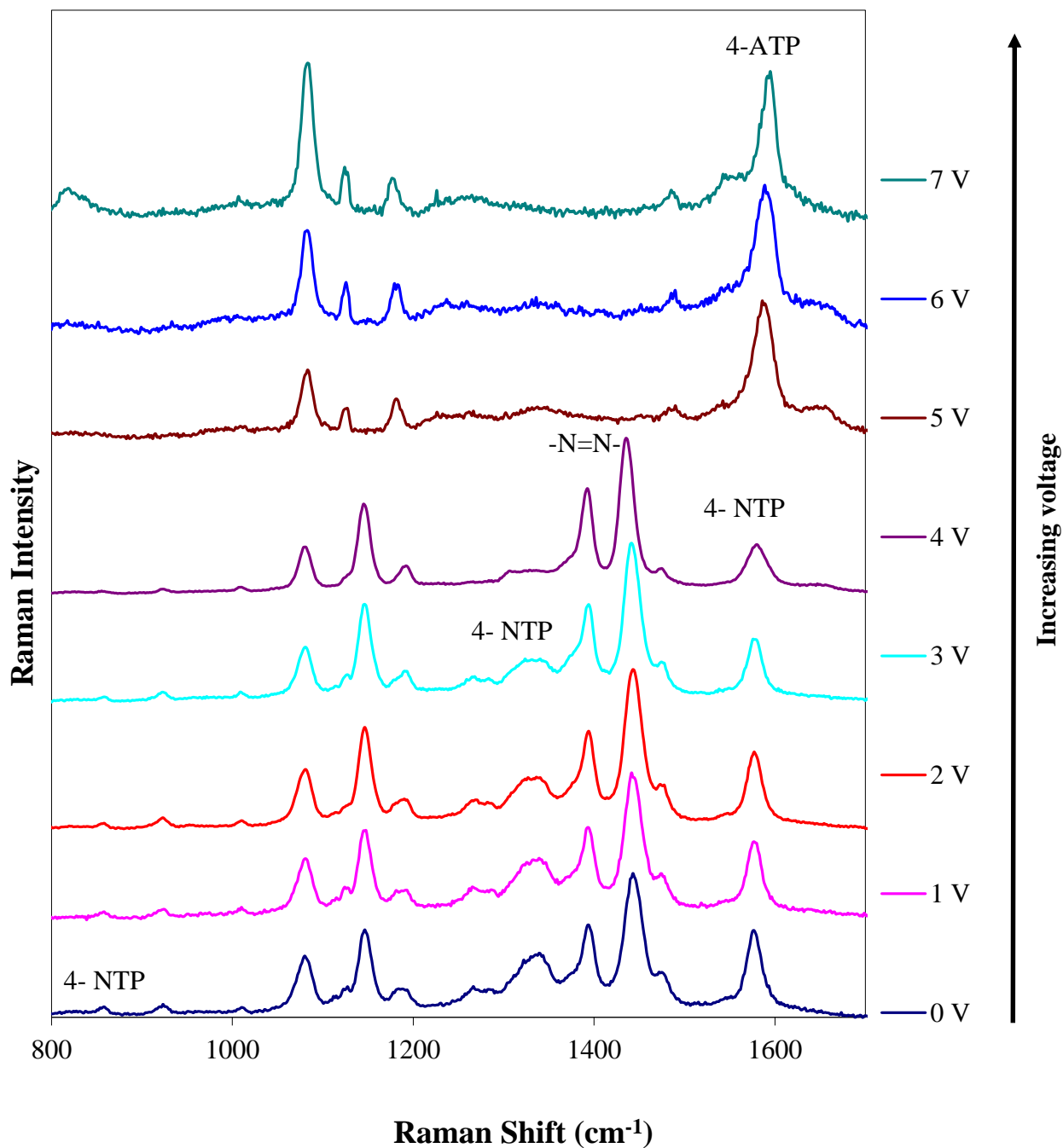


Figure 2.12: In situ SERS spectra of 4 NTP SAM on an Ag- Au alloy bipolar electrode in 0.01 M  $\text{NaClO}_4$  aqueous solution at different potential in a bipolar electrode cell. The spectrum was obtained at the edge of the cathodic pole from 0V to 7 V across the electrolyte.

Since SERS by the charge transfer is a kind of resonance effect, there is a possibility to arise some special raman bands are selectively enhanced. The difference between normal raman and SERS spectra of 4-nitrothiophenol arises from charge transfer mechanism. From this data we conclude that reduction start when 5 V applied across two driver electrode. Then we fixed the potential difference at 5 V (figure 2.13) for evaluating the gradient of Au- Ag alloy gradients. After applying the potential reduction start at 1mm of cathodic edge of bipolar electrode. In bipolar setup the reduction rate is faster than chemical reduction. It takes less time compared to chemical reduction on alloy gradient and unipolar setup also. We can see that there was no 1574  $\text{cm}^{-1}$  peak and 1344  $\text{cm}^{-1}$  peak also diminishes at 4 mm. But two intermediate peak arose at 4 mm distance from the cathodic edge on the gradient, 1394  $\text{cm}^{-1}$  and 1435  $\text{cm}^{-1}$  which were due to N=N stretching, and C-H in-plane bending modes of 4, 4'-dimercapto-azobenzene (4, 4'-DMAB). But these two peaks also diminish at 6 mm. The reason for that is there was two variables from cathodic pole to anodic pole. One is the composition of Au and Ag, because Au-Ag alloy deposited in a gradient manner here. Other one is the applied potential. Potential is getting lower with the increasing distance from the edge. That's why we noticed intermediate point at 5 V and the  $\text{NO}_2$  peak was observed again. At 8 mm it was only 4-NTP. There was no reduction occur at that point. Because the electrochemical potential was insufficient at 8 mm. This is the clear indication of Au -Ag gradient deposition and potential gradient. From 6 to 7 mm from cathodic pole, that area is silver rich (71 at%, from EDS result) area. Reduction occur this area very fast and completely. That is why we saw the gradually increase of  $\text{NO}_2$  peak here with having the borderline potential<sup>25</sup>. There was no deposition in 9 mm area.

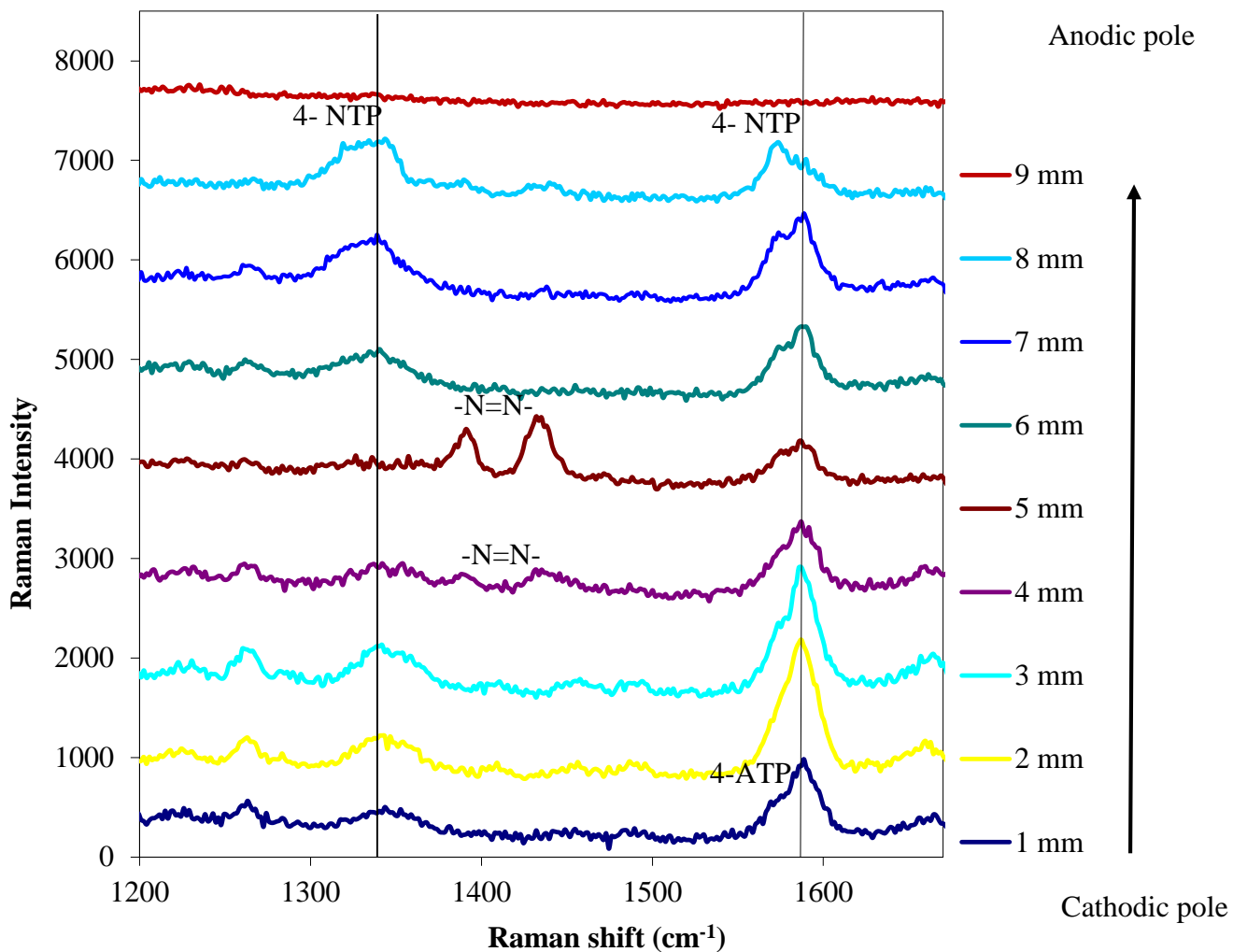


Figure 2.13: In situ SERS spectra of 4 NTP SAM on an Ag- Au alloy bipolar electrode in 0.01 M NaClO<sub>4</sub> aqueous solution at different position in a bipolar electrode cell. The spectrum was obtained at 5 V across the electrolyte

Then we fixed the potential difference at 7 V (figure 2.14) for evaluating the gradient of Au- Ag alloy in a bipolar cell. Reduction start immediately from first scan (less than 30 second) at 1mm of cathodic edge of bipolar electrode. We noticed there were no NO<sub>2</sub> peak, no intermediate peak in each and every spectrum. Only we have the product aminothiophenol peak at 1592 cm<sup>-1</sup>. Figure 2.15 showed that After completely reduction the NTP monolayer destroyed when we apply 11 V

at. But in alloy area SAM was in better condition which is far from cathodic area. This is because of potential gradient between two driver electrode.

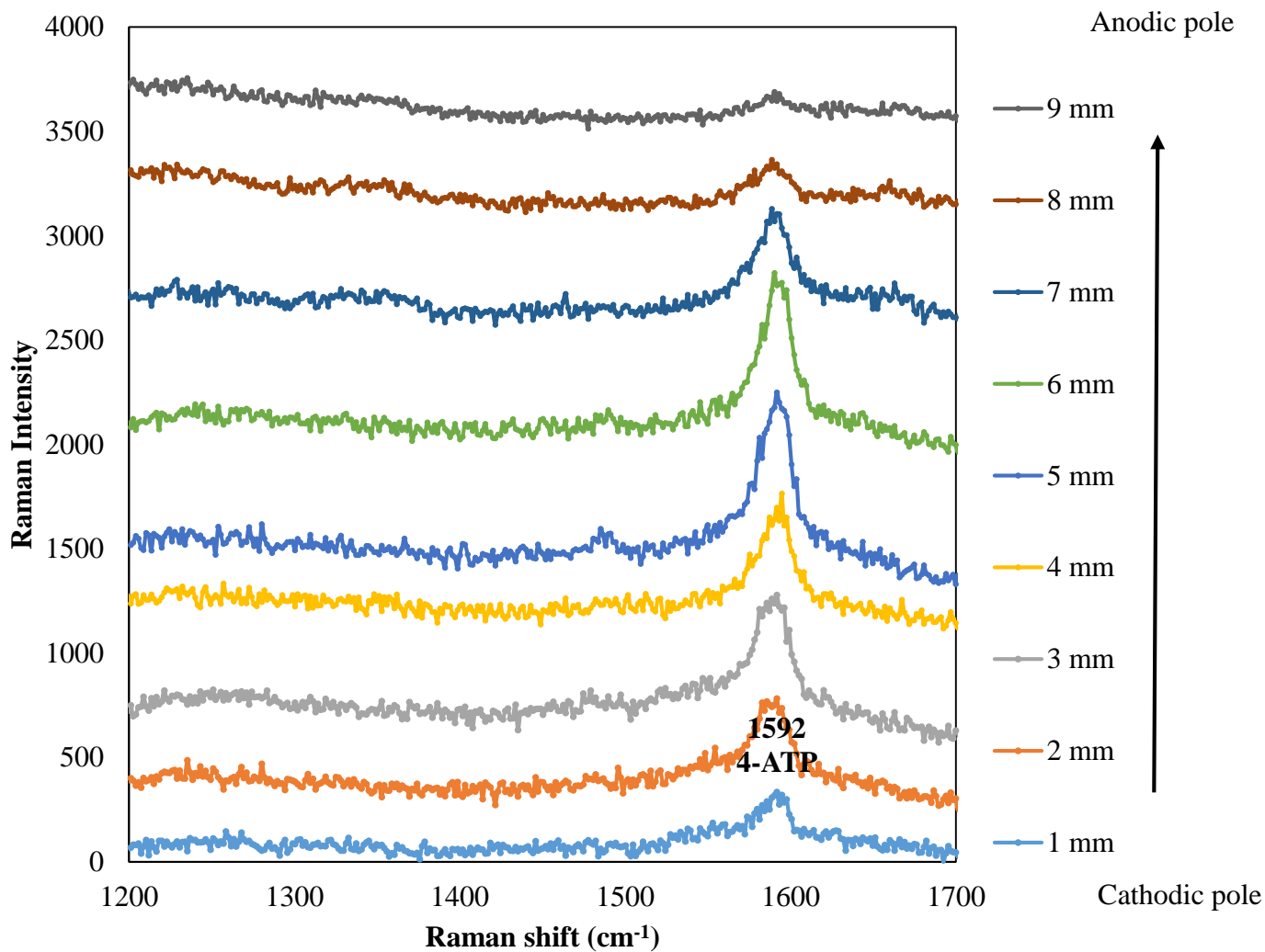


Figure 2.14: In situ SERS spectra of 4 NTP SAM on an Ag- Au alloy bipolar electrode in 0.01 M NaClO<sub>4</sub> aqueous solution at different position in a bipolar electrode cell. The spectrum was obtained at 7 V across the electrolyte.

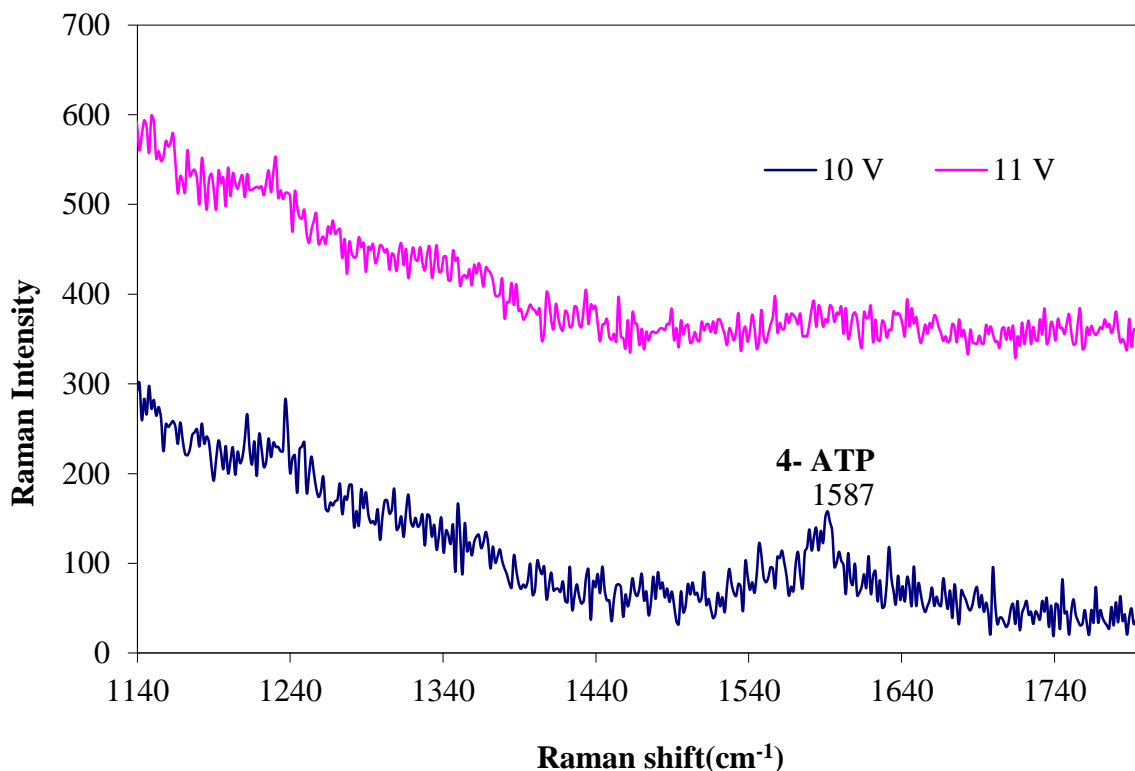


Figure 2.15: In situ SERS spectra of 4 NTP SAM on an Ag- Au alloy bipolar electrode in 0.01 M NaClO<sub>4</sub> aqueous solution at different potential.

The kinetics of this reduction reaction, 4-nitrothiophenol to 4-aminithiophenol with NaBH<sub>4</sub> as an ideal reaction has been investigated often on mixed-nanoparticle surfaces.<sup>29-30</sup> In order to investigate a metal-catalyzed reaction with SERS or other plasmon-supported approaches,<sup>31</sup> multifunctional metal structures are required which have plasmonic properties and also catalytically active.<sup>27</sup> Catalytically active complex nanoparticles have been reported to increase the Raman signals in dye molecules,<sup>22</sup> and SERS has been used to observe the structural growth of bimetallic catalytically active Au-Pt nanoparticles.<sup>32</sup> However, direct observations of a catalytic process by SERS have been rare as they require bifunctional nanomaterials.<sup>33</sup> Our method is different from those previously stated based on composite nanostructures with plasmonic and catalytic properties. We investigated the catalytic activity of the Au-Ag alloy gradient by the reduction of 4-

nitrothiophenol to 4-aminithiophenol by applying potential. The efficiency of heterogeneous catalysis of electron-transfer reactions on the surface of gold nano shells can be changed by adding an inner platinum or palladium nano shell in the double-shell nanocatalysts.<sup>34</sup> Reaction takes place on the gold nanoparticle catalyst surface.<sup>35</sup> But plasmon resonance is weak due to the small scattering cross section. The catalytic activity of bimetallic Au-Ag alloy nanoparticles is superior than the regular Au or Ag nanoparticles.<sup>25</sup> This possibly caused by the intense rise of the catalytic activity after alloying of silver with gold. Our plan is to do kinetics study in bipolar electrochemical method. Before doing that we conduct the experiment in unipolar system, because there are two types of gradient present in bipolar setup. One is potential gradient and another is compositional gradient along the length. In three electrode system we can fixed the potential and screened the compositional gradient effect on the Au-Ag gradient. Here kinetics study was done in three electrode cell with controlled potential electrolysis. For that we use Au-Ag gradient as working electrode and fixed the potential at -0.6 V. From cyclic voltammogram we can find that is the minimum potential to initiate the reduction of 4-NTP.

We observed an apparent first order decay of the 4-NTP ( $1344\text{ cm}^{-1}$ ,  $\text{NO}_2$ ) and increase of 4-ATP band ( $1595\text{ cm}^{-1}$ ,  $\text{NH}_2$ ) Raman peak intensity. Kinetic data were measured from six spots along the bipolar electrode-each corresponding to a unique Au-Ag alloy composition. Representative data are shown in figure 2.16. The large excess of  $0.1\text{M NaClO}_4$  (aqueous solution) used for in situ kinetic study means the reaction order of  $\text{NaClO}_4$  could be considered as zero, and the reduction route could be supposed to follow pseudo-first-order kinetics. This was similar to the reduction of nitrothiophenol catalyzed by metal NPs.<sup>30</sup> We fit all of the kinetic data using a simple first order decay model

$$[A]/[A]_0 = e^{-kt}$$

where  $[A]$  = concentration of reactant at time  $t$ ,  $[A]_0$  = initial concentration of reactant,  $k$  = apparent first order rate constant and calculated the apparent first order rate constants. The reaction rate constant,  $k = 4.9 \times 10^{-3} \text{ s}^{-1}$  was obtained (figure 2.17) from the slope of the linear relationship between  $\ln(I_t/I_0)$  and  $t$ . Calculated apparent rate constant for 4-NTP reduction (4-ATP formation) at different position of the gradient is plotted as a function of Ag atomic percentage.  $1344 \text{ cm}^{-1}$  peak intensity was considered for the 4-NTP reduction. From the figure we can see that silver area has the better kinetics from gold rich region. Error bar is showing the standard deviation is 2%. So we achieve the different kinetics in one single substrate.

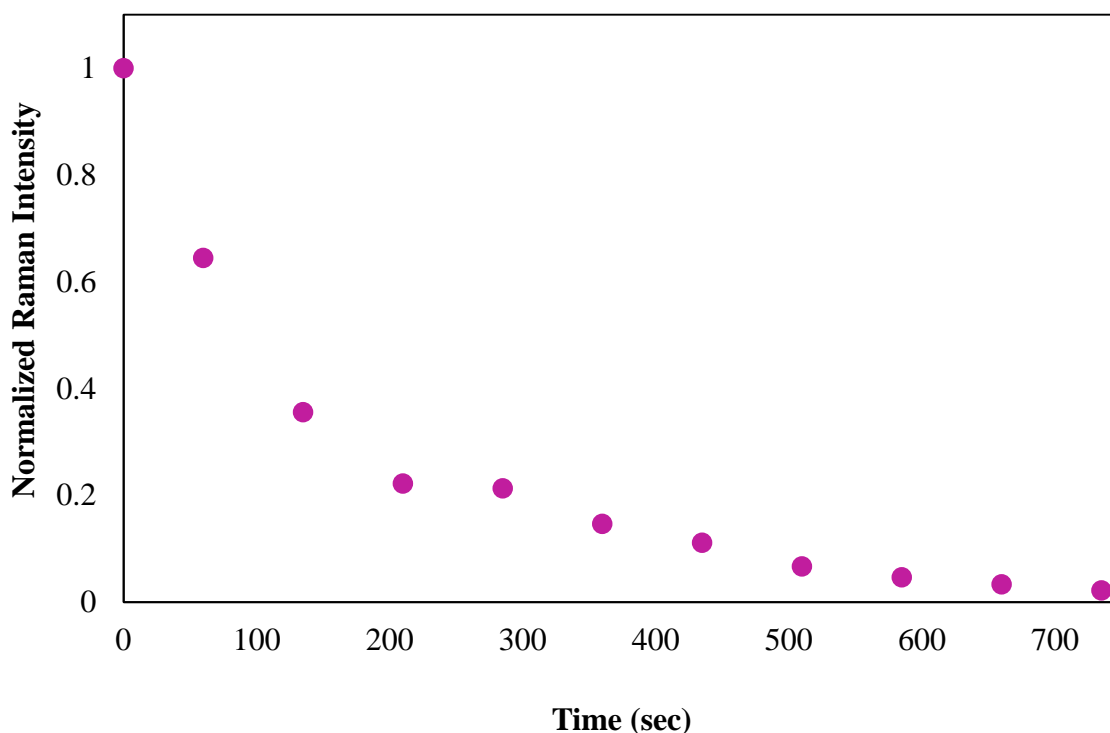


Figure 2.16: 4-NTP decay measured at silver rich area with time, away from the cathodic pole on BPE for  $1344 \text{ cm}^{-1}$ .

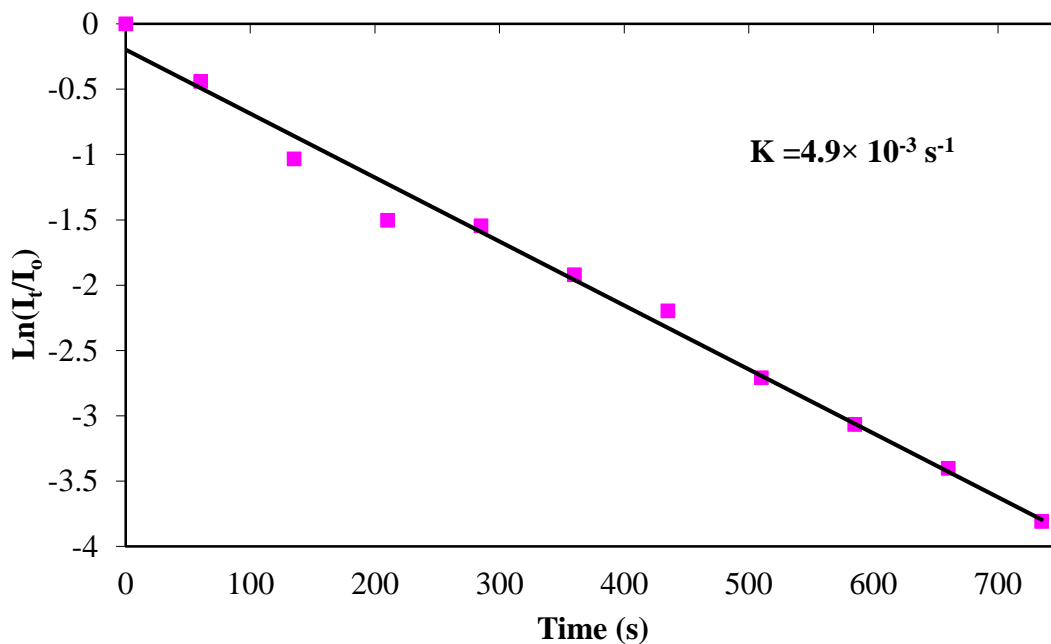


Figure 2.17: Plot of the logarithm of the relative SERS intensity at  $1344 \text{ cm}^{-1}$  ( $\ln(I_t/I_0)$ ) versus the reaction time.

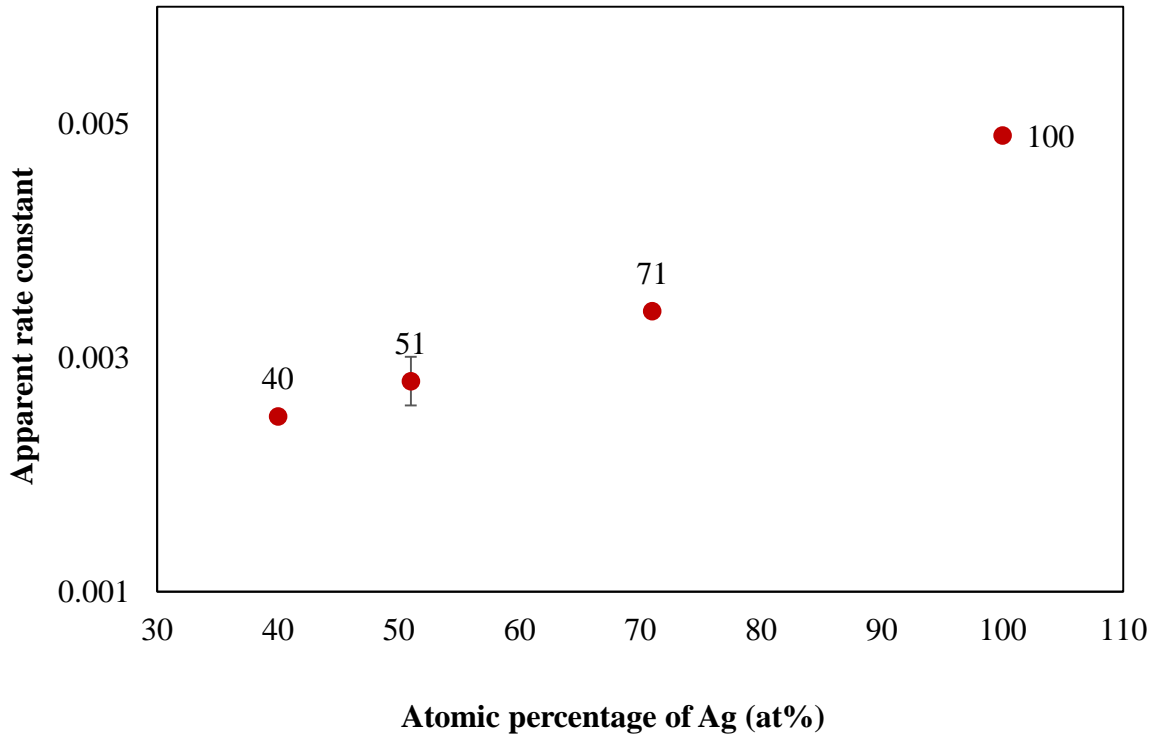


Figure 2.18: Calculated apparent rate constant for NTP reduction ( $1344 \text{ cm}^{-1}$ ) plotted as a function of Ag atomic percentage.  $1595 \text{ cm}^{-1}$  peak intensity was considered here.

Normalized Raman Intensity for 4-ATP formation peak,  $1595\text{cm}^{-1}$  also plotted as a function of time for different alloy constant in figure 2.19. From starting the reduction (applying the  $-0.6\text{ V}$ ) up to 750 seconds spectra was collected. Interval between each spectrum was 15 seconds. 4-ATP formation also following pseudo first order kinetics (figure 2.19). It is also showing higher kinetics for 100 at% of silver. 70% silver also showing almost same formation rate for 4-ATP. 50% and 40% has the lower formation rate. But we can see from figure 2.19 that after 90 second of starting reaction all 4 composition has the same rate trend. That's means first 90 is Photo chemical reduction is taking place.

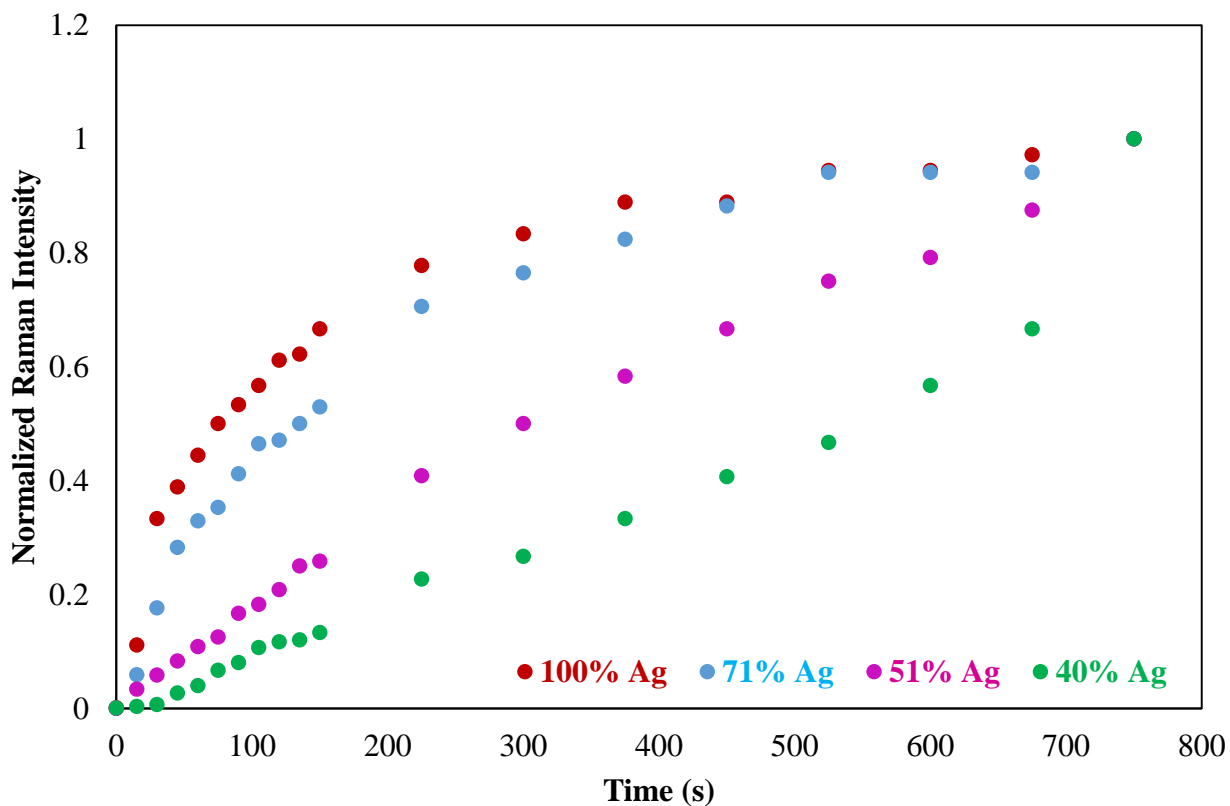


Figure 2.19:  $\text{NH}_2$  peak ( $1595\text{ cm}^{-1}$ ) rising measured at different points along the BPE. Each point corresponds to a unique alloy composition. (Top to bottom: Ag atomic% is 100, 71, 51 and 40).

After that reduction complete electrochemically. And photo reduction depends on silver composition, because silver has better surface plasmon resonance than gold. From figure 2.19 we

can ensure that. First 7 spectra which is up to 90 second, fit in the first order rate law equation. Apparent rate constant was calculated and plotted against the atomic percentages. This also following the similar trend like figure 2.18. For 100% silver we have the faster kinetics. The main reason for this is localized surface plasmon of silver. Green laser initiated the reduction of 4-NTP on silver quickly and reaches to the intermediate product which is 4,4'-DMAB. These spectral fluctuations are very interesting in the study of this heterogeneous catalytic reactions, as reaction intermediates have short life-spans and might only be observed in the most intense hotspots.

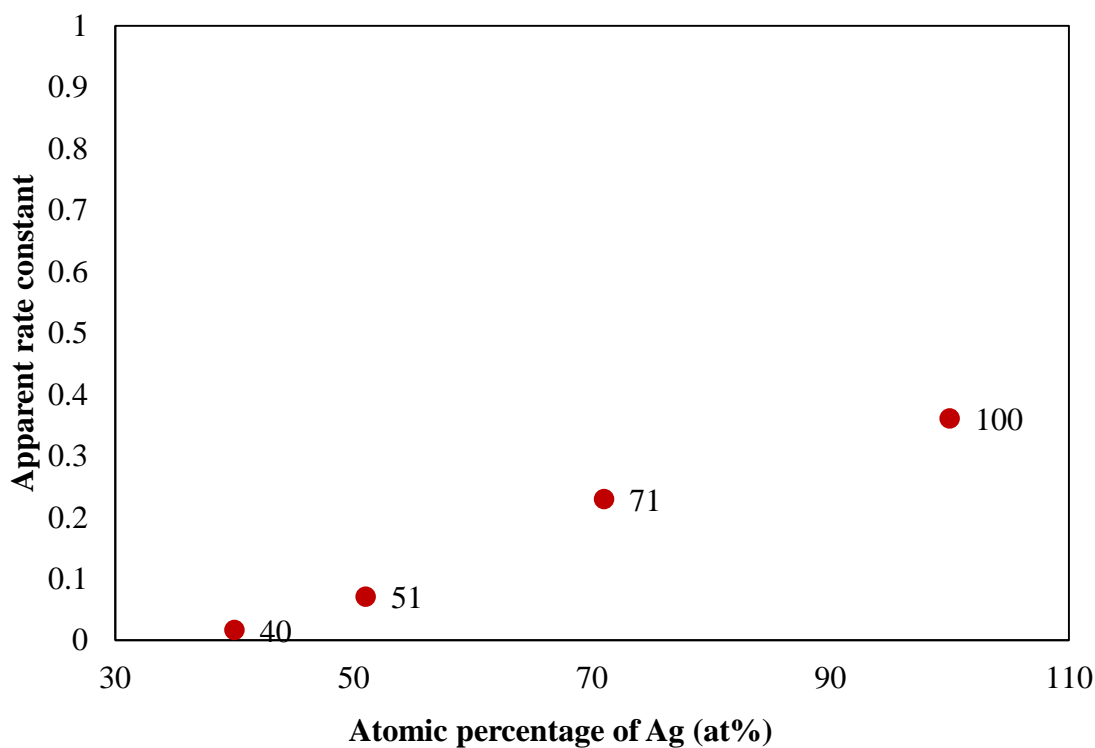


Figure 2.20: Calculated apparent rate constant for ATP formation (initial, up to 90 sec) plotted as a function of Ag atomic percentage.  $1595\text{ cm}^{-1}$  peak intensity was considered here.

The apparent rate constant ( $k$ ) for each alloy composition is plotted in figure 2.20. Highest oxidation rate was observed at 100% of Ag area (figure 2.19). Han et al also showed that catalytic activity of gold in this reaction increased with introducing silver.<sup>25</sup>

## **2.5 Conclusion:**

Use of bipolar electrodeposition for generating size gradients in gold–silver alloy nanoparticles on stainless steel surfaces was also explored. A highly SERS active Au-Ag alloy gradient was successfully achieved by using bipolar electrodeposition (BPE) technique. Alloy deposited on the cathodic pole of the surface with different composition of silver and gold. The kinetics of the gradient was screened by surface enhancement of raman spectroscopy (SERS). 4-NTP (nitrothiophenol) was used as raman probe here. EDS data showed that the alloy percentage was 70 at% Ag and 30 at% Au (maximum). Also from variation of SERS intensity of corresponding  $\text{NO}_2$  peak also confirmed the existence of gradient. Then we use this Au-Ag silver alloy gradient as a catalyst for 4 nitrothiophenol reduction reaction. We also monitored the SERS in real time for chemical reduction on this alloy gradient with  $\text{NaBH}_4$ . By comparing all results, we can conclude that the rate of the reaction depends on the alloy composition. Because gold is catalytically active than silver and silver has stronger surface plasmon resonance from gold. By introducing gold and silver together we can complete the reduction fast comparing to chemical method. The alloy is better than monometallic nanoparticles for this reaction. The capability to build substrates with metal gradients is highly beneficial for sensor screening applications<sup>36</sup> and catalytic application.<sup>37</sup> This method could bring us a new multimetallic gradient system with better catalytic activity.

## References

1. Stiles P.L.; Dieringer, J.A.; Shah, N.C.; Van Duyne, R.P. *Annu. Rev. Anal. Chem.* **2008**, *1*, 601–626.
2. Christopher, P.; Xin, H.; Linic, S. *Nat. Chem.* **2011**, *3*, 467–472.
3. Geshev, P. I.; Fischer, U.; Fuchs, H. *Phys. Rev. B* **2010**, *81*, 125441-1-16.
4. Homola, J.; Yee, S. S.; Gauglitz, G. *Sensors and Actuators B* **1999**, *54*, 3–15.
5. Kim, J-W.; Galanzha, E. I.; Shashkov, E. V.; Moon, H-M.; Zharov, V. P. *Nat. Nanotech.* **2009**, *4*, 688 – 694.
6. Donga, J; Qua, S.; Zhenga, H.; Zhanga, Z.; Li, J.; Huoa, Y.; Li, G.; *Sensors and Actuators B* **2014**, *191*, 595–599.
7. Vassalini, I.; Rotunno, E.; Lazzarini, L.; Alessandri, I. *ACS Appl. Mater. Interfaces*, **2015**, *7*, 18794–18802.
8. Li, J. N.; Liu, T. Z.; Zheng, H. R., Gao, F.; Dong, J.; Zhang, Z. L.; Zhang, Z. Y. *Opt. Express*, **2013**, *21*, 17176–17185.
9. Ye, X.; Chen, J.; Diroll, B.T.; Murray, C. B. *Nano Lett.* **2013**, *13*, 1291–1297.
10. Fleischmann, M.; Hendra, P. J.; Mcquillan, A. J. *Chem. Phys. Lett.* **1974**, *26*, 163–166.
11. Luo, S.-C.; Sivashanmugan, K.; Liao, J.-D.; Yao, C.-K.; Peng, H.-C. *Biosens. Bioelectron.* **2014**, *61*, 232–240.
12. Ramaswamy, R.; Shannon, C. *Langmuir* **2011**, *27*, 878-881.
13. Abdelsalam, M.; Bartlett, P. N.; Russell, A. E.; Baumberg, J. J.; Calvo, E. J.; Tognalli, N. G.; Fainstein, A. *Langmuir* **2008**, *24*, 7018–7023.
14. Orinakova, R.; Skantarova, L.; Orinak, A.; Demko, J.; Kupkova, M. Andersson, J. T. *Int. J. Electrochem. Sci.* **2013**, *8*, 80–99.

15. Kelf, T. A.; Sugawara, Y.; Cole, R. M.; Baumberg, J. J. Abdelsalam, M. E.; Cintra, S.; Mahajan, S.; Russell, E. A.; Bartlett, P. B. *Phys. Rev.B* **2006**, *74*,1– 12.
16. Ishiguro, Y.; Inagi, S.; Fuchigami, T. *Langmuir*, **2011**, *27*, 7158–7162.
17. Chen, G.; Wang, Y.; Yang, M.; Xu, J.; Goh, S. J.; Pan, M.; Chen, H. *J. Am. Chem. Soc.* **2010**, *132*, 3644–3645.
18. Netzer, N. L.; Qiu, C.; Zhang, Y.; Lin, C.; Zhang, L.; Fong, H.; Jiang, C. *Chem. Commun.* **2011**, *47*, 9606-9608.
19. Xie, W.; Walkenfort, B.; Schlücker, S. *J. Am. Chem. Soc.* **2013**, *135*, 1657–1660.
20. Kim, K.; Lee, Y. M.; Lee, H. B.; Park, Y.; Bae, T. Y. Jung, Y. M.; Choic, C. H.; Shind, K. *S. J. Raman Spectrosc.* **2010**, *41*, 187–192.
21. Fang, Z.; Wang, Y.; Liu, Z.; Schlather, A.; Ajayan, P. M.;Koppens, F. H.; Nordlander, P.; Halas, N. *J. ACS Nano* **2012**, *6*, 10222–10228.
22. Matsuda, N.; Yoshii, K. *Chem lett.* **1992**. 1385-1388.
23. Ramakrishnan, S.; Shannon, C. *Langmuir* **2010**, *26*, 4602–4606.
24. Kayran, Y. U.; Eßmann, V.; Grützke, S.; Schuhmann, W. *Chem Electro Chem* **2016**, *3*,399–403.
25. Han, Q.; Zhang, C.; Gao, W.; Han, Z.; Liu, T.; Li, C.; Wang, Z.; He, E.; Zheng, H. *Sensors and Actuators B* **2016**, *231*, 609–614.
26. Huang, J.; Zhu, Y.; Lin,M.; Wang, Q.; Zhao, L.;Yang, Y.; Yao, X.; Han, Y. *J. Am. Chem. Soc.* **2013**, *135*, 8552–8561.
27. Bin Dong, B.; Fang, Y.; Chen, X.; Xu, H.; Sun, M. *Langmuir* **2011**, *27*, 10677–10682.
28. Matsuda, T.; Sugawara, T. *Chem. Lett.* 1995. 145-146.
29. Kneipp, J. *Angew. Chem., Int. Ed.* **2012**, *51*, 7592.

30. Zhang, K.; Zhao, J.; Ji, J.; Li, Y.; Liu, B. *Anal. Chem.* **2015**, *87*, 8702–8708.
31. Jing, H.; Zhang, Q.; Large, N.; Yu, C.; Blom, D. A.; Nordlander, P.; Wang, H. *Nano Lett.* **2014**, *14*, 3674–3682.
32. Luis. M.; MarzBn, L. ;Philipse, A. P. J. *Phys. Chem.*, Vol. 99, No. 31, **1995**
33. Ren, X.; Tan, E.; Lang, X.; You, T.; Jiang, L.; Zhang, H.; Yin, P.; Guo, L. *Phys. Chem. Chem. Phys.* **2013**, *15*, 14196-141201.
34. Mahmoud, A. M.; Garlyyev, B.; El-Sayed, M. A. J. *Phys. Chem. Lett.* **2014**, *5*, 4088–4094
35. Saha, S.; Pal, A.; Kundu, S.; Basu, S.; Pal, T. *Langmuir* **2010**, *26*, 2885–2893.
36. Maier, W. F.; Klaus Stöwe, K.; Sieg, S. *Angew. Chem. Int. Ed.* **2007**, *46*, 6016 – 6067.
37. Jayaraman, S.; Hillier, A. C. *Meas. Sci. Technol.* **2005** *16*, 5–13.

## Chapter Three

### Deposition And Characterization Of One And Two Dimensional Au-Ag Alloy Gradients By Bipolar Electrodeposition

#### Abstract

Bipolar electrochemistry is an unconventional technique that currently encounters a renewal of interest due to modern applications in the fields of analytical chemistry or materials science. The approach is particularly relevant for the preparation of asymmetric objects or surfaces such as *Janus* particles for example. Bipolar electrochemistry allows spatially controlled deposition of various layers from electroactive precursors, selectively at one side of a bipolar electrode. We report here the concomitant cathodic deposition of two different metals at the same time in a single experimental setup. By using the bipolar electrodeposition for creating Au-Ag alloy gradients nanoparticles was formed on stainless steel substrate. The deposits were characterized by optical and electron microscopy imaging as well as energy dispersive X-ray spectroscopy. As a result, the deposited layer is composed with a composition gradient. Such a variation directly modifies the optical and electronic properties alongside the surface and gives access to the design of composite surfaces exhibiting a visual gradient feature. Finally, two-dimensional Au-Ag alloy gradients were achieved by placing samples in a two dimensional bipolar electrochemical cell. Self-assembled monolayers were formed on top of the substrates pre-deposited with Au-Ag alloy gradients. This surface was screened by Surface enhanced raman spectroscopy (SERS). The ability to create substrates with gradients of alloy is highly beneficial for sensor screening applications.

#### 1.1 Introduction

Electrodeposition is a common method for depositing material on a conductive surface. This deposition takes place in a film growth manner. This approach has been broadly used in decorative purposes, corrosion protection, and in many other applications.<sup>1-3</sup> Electrodeposition of metals is important for a variety of industries including electronics, optics, and sensors, automotive and aerospace. Electrodeposition is a well-known method for growth of bimetallic alloys for over more than 60 years. At present there are more than hundreds of alloys are synthesized using electrochemical methods. Most common are based on Cu, Au, Ag and noble metals. Electrochemical alloys frequently show better properties and arrangement than single constituents even in contrast to metallurgical alloys.

An escalation or decrease in the degree of a property (e.g., temperature, pressure, or concentration) detected in moving from one point or moment to another is known as gradient. Gradients of physicochemical properties, their gradual change in space or time, are of great value both in solution and on surfaces. Gradients have been successfully engaged in materials science<sup>4</sup> and combinatorial/analytical chemistry<sup>5-6</sup> improving the proficiency of the design and finding of catalysts and drugs, and providing fresh analytical methods. There are several gradient-fabrication approaches in which electrochemistry plays a role. The properties of gradients produced by electrochemical techniques can be influenced in some ways, such as by the locating and arrangement of electrodes in combination with diffusion or by spatioemporal variation of the applied potential. Electrochemical gradient creation methods have many additional beneficial properties.

Metal electrodeposition by bipolar electrodeposition is an exciting approach to generate asymmetric surfaces. Ag- Au alloys deposited from bipolar electrodeposition was done by Shannon's group.<sup>7</sup> They characterized that bimetallic gradient by surface enhanced Raman

spectroscopy (SERS). They also deposited CdS on gold surfaces by the same way.<sup>8</sup> Dorri et al showed the electrodeposition of Cu gradient from bipolar electrochemistry.<sup>9</sup> Gradients depend on three parameters for instance time, potential, and concentration of precursors. Loget et al built a new model of development of self-assembled TiO<sub>2</sub> nanotubes layers that contains highly defined and controllable gradients in nanotube length and diameter.<sup>10</sup> They used the bipolar electrodeposition method for this system. They demonstrated that these gradient arrangements can be used in dye-sensitized solar cells.<sup>10</sup>

Bipolar electrochemistry is a useful experimental technique for the formation of compositional or chemical gradients along the surface on a wireless conductive object.<sup>8,9,11</sup> The idea of bipolar electrochemistry is very different from the established three-electrode electrochemical cell which operates with a working, counter, and reference electrode. The electric field that controls bipolar electrochemistry is typically applied between two driving electrodes, which can be metallic (e.g., Au, Ag, Pt, or stainless steel), glassy carbon or graphite. The substrate (BPE) can be any type of material, but its conductivity must be higher than that of the surrounding medium. Oxidation and reduction reactions take place at opposite ends of a bipolar electrode without direct electrical connections to an external power supply.

A Schematic representation of the principle of bipolar electrochemistry is shown in figure 3.1. The electric field is applied across the solution by two feeder electrodes connected to an external power supply (fig. 3.1A). The driving force ( $\Delta V_{max}$ ) is directly proportional to the electric field ( $E_{tot}$ ) and the length of the bipolar electrode ( $l$ ) according to the following equation (3.1).

$$\Delta V_{max} = E_{tot} \times l \quad (3.1)$$

This means that the promotion of electrochemical reactions at the two opposite ends of a conducting object needs a  $\Delta V_{max}$  value which is at least equal to the difference between the formal standard potentials of the two reactions. As a significance, the size of the bipolar electrode is an intrinsic limitation because the smaller the electrode is, the higher the electric field has to be. Virtually, the value of  $E_{tot}$  can vary from a couple of volts per centimeter in the case of macroscopic bipolar electrodes, up to a few kV/cm for microscale objects. It is also important to mention that the polarization varies alongside the bipolar electrode, meaning that the highest over potentials ( $\eta_{max}$ ) are generated at the outermost extremities, or in other words a potential gradient is established along the bipolar electrode.<sup>13</sup> In the simplified symmetric case presented in figure 3.1B, the maximum anodic and cathodic polarization potentials are equal and, as a matter of fact, a decrease of the polarization potential is observed when moving from the edge towards the middle of the bipolar electrode ( $\eta_{max} > \eta_i > \eta_j$ ). This is a major advantage of BPE when compared to conventional electrochemistry, for example in the situation of electrodeposition studies. Instead of studying the electrochemical reactivity at a single potential value, BPE allows screening a range of different thermodynamic conditions along the bipolar electrode in one single experiment.<sup>13</sup> There are no conducting leads to either side of the bipolar electrode, and the single bipolar electrode side is both the anode and the cathode. Furthermore, there is a potential gradient generates in solution, whereas the bipolar electrode has a potential that is (approximately) equal everywhere on its surface. Consequently, a potential difference is created between the surface of the bipolar electrode and the solution, and this potential difference differs in-plane laterally the surface. When adequate voltage is applied to an electrolyte solution containing a bipolar electrode, the potential difference among the bipolar electrode and the electrolyte solution drives electrochemical reactions, with the highest reaction rates at the edges of the bipolar electrode. Both

one dimensional and two dimensional gradients can be fabricated with this method.<sup>12</sup> Basically, metals deposit at different potentials, and bipolar electrodes have a gradient in potential. If the bipolar method is applied to a solution containing a combination of different metals, these will deposit at different locations along the bipolar electrode surface based on their corresponding redox potential.<sup>8</sup> Ag-Au bimetallic alloys gradient can be deposited from bipolar electrochemistry. Ag deposition is thermodynamically favored (i.e.,  $E^0_{Ag} > E^0_{Au}$ ) and Au deposition is kinetically favored. So that the chemical composition of electrodeposited Ag-Au alloys is dependent on the applied potential.

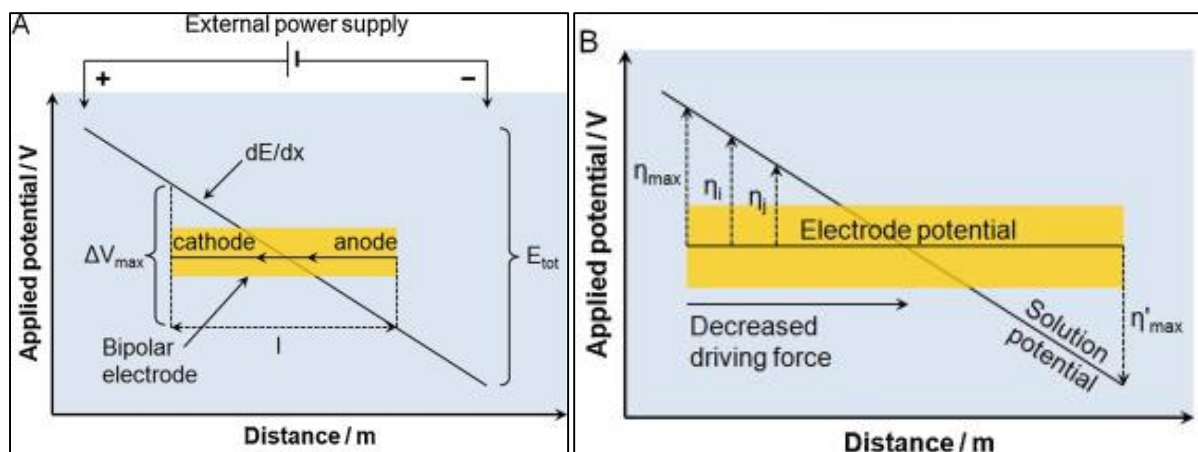


Figure 3.1: Schematic representation of the principle of bipolar electrochemistry (A). The interfacial potential polarization between the solution and the bipolar electrode (B).

(Reprinted with permission from Ref 13, Copyright © 2016 Elsevier B.V)

In this thesis, we reported bipolar electrodeposition of Au-Ag alloy on stainless steel surfaces. The interfacial potential varies along the length of the bipolar electrode, which causes the chemical concentration gradients and control the rates of electrodeposition of Au and Ag on the bipolar electrode. Here we deposited Au-Ag alloy in both one and two dimensional manners.

These alloys are characterized by using scanning electron microscopy (SEM) and energy dispersive X-ray spectroscopy (EDX) and self-assembled monolayers of a Raman-active probe molecule (benzene thiol) were formed on the surface of the alloy gradient and confocal Raman microscopy was used to find the alloy composition from the maximum surface enhanced Raman scattering (SERS) intensity. Variations of SERS intensity could be explained on the basis of the optical properties of the electrodeposited alloy.

### **3.2 Experimental:**

**3.2.1 Materials:** Potassium dicyanoaurate  $\text{KAu}(\text{CN})_2$  (98% ACS reagent, Aldrich Chemical Co.), Potassium dicyanoargentate  $\text{KAg}(\text{CN})_2$  (98% ACS reagent, Aldrich Chemical Co.), KCN (99.5% ACS reagent, Fisher Scientific Company), and KOH (87.1%, Fisher Scientific Company), Benzene thiol were used as purchased. Type 304 Stainless Steel foil, 0.25mm (0.01in) thick used for driver electrode and type 304 Stainless Steel foil, 0.1mm thick used as bipolar electrode in bipolar electrochemical cell. Millipore-Q purified deionized (DI) water ( $18.2\text{M}\Omega/\text{cm}^3$ ) was used to make all solutions and to clean electrodes.

**3.2.2 Substrate Preparation:** 18 mm long and 4mm wide stainless steel (0.1 mm) substrates were mechanically polished with 800 grit SiC paper. Then they were cleaned by rinsing consecutively with DI water and absolute ethanol. Finally, the substrate was sonicated in water- Ethanol mixture for 5min. After being dried in a stream of flowing nitrogen, the clean stainless steel bipolar electrode was placed into the bipolar electrochemical cell. Driver electrodes were prepared by rinsing sequentially with distilled water, absolute ethanol, and distilled water, and were dried in a stream of flowing nitrogen.

**3.2.3 Bipolar Electrochemistry:** All bipolar electrochemistry experiments were performed in a home-built single compartment glass cell (ca. 15mL total volume) using a Hewlett-Packard model 6010 regulated DC power supply to control the potential applied between two stainless steel driver electrodes separated by 2 cm. The electrically floating stainless steel bipolar electrode was located symmetrically between the two stainless steel driver electrodes, as previously reported.<sup>9</sup> The two dimensional bipolar electrode was 1 cm long and 1 cm wide. These three electrodes were immersed in an electrodeposition solution containing 5 mM  $\text{KAu}(\text{CN})_2$ , 5 mM  $\text{KAg}(\text{CN})_2$ , 200 mM KCN, and pH of the electrolyte adjusted by KOH (pH=12). Ag-Au alloy films were deposited by applying a voltage of 10.0 V across the driver electrodes for 1 min at room temperature. The BPE was then rinsed with DI water, dried in a stream of flowing nitrogen, and stored in a closed vial prior to analysis using SEM and EDX.

**3.2.4 Formation of Benzene Thiol Self-Assembled Monolayers:** A freshly deposited Au-Ag alloy gradient was immediately immersed in a 5 mM ethanolic solution of benzene thiol for 15 h after washing by DI water and dried by  $\text{N}_2$ . After monolayer formation, the specimen was rinsed with ethanol and dried in  $\text{N}_2$  prior to analysis by confocal Raman microscopy.

**3.2.5 Scanning Electron Microscopy (SEM) and Energy Dispersive X-ray spectroscopy (EDX):** SEM images of the electrodeposited Ag-Au alloy on a gold bipolar electrode were acquired from a JEOL JSM- 7000F field- emission scanning electron microscope and analyzed using the EOS 7000F software package. EDX data were acquired using the Oxford X-Max energy dispersive X-ray spectrometer and were analyzed using the INCA software package.

**3.2.6 Raman spectroscopy:** Raman scattering was excited using the 514.5 nm output (ca. 20 mW) from an air-cooled argon ion laser (model 163-C42, Spectra-Physics Lasers, Inc. Raman measurements were acquired as a function of position along the length of the bipolar electrode and

analyzed using a Renishaw inVia Raman microscope system. Raman signals were accumulated for each spectrum was 10 seconds and only a single scan was made. A 1200 lines  $\text{mm}^{-1}$  grating was used for all measurements providing a resolution of  $\pm 1\text{cm}^{-1}$ . The instrument was calibrated for the Raman shift by referencing to that of silicon.

### 3.3 Results and Discussion

**3.3.1 Au-Ag alloy gradient by bipolar electrodeposition:** Here we demonstrated the one and two dimensional Au-Ag alloy gradient deposition from the same electrolyte bath. Figure 3.2 is the picture of the Au-Ag alloy gradient deposited on stainless steel, both one dimensional and two dimensional. Two different region are indicating by arrow sign. Au-Ag alloy gradient and Ag rich area. Figure 3.4 is the picture of home built one and two dimensional bipolar electrochemical cell. Two dimensional deposition cell was made by glass. One dimensional deposition was done in a glass petri dish (15 ml).

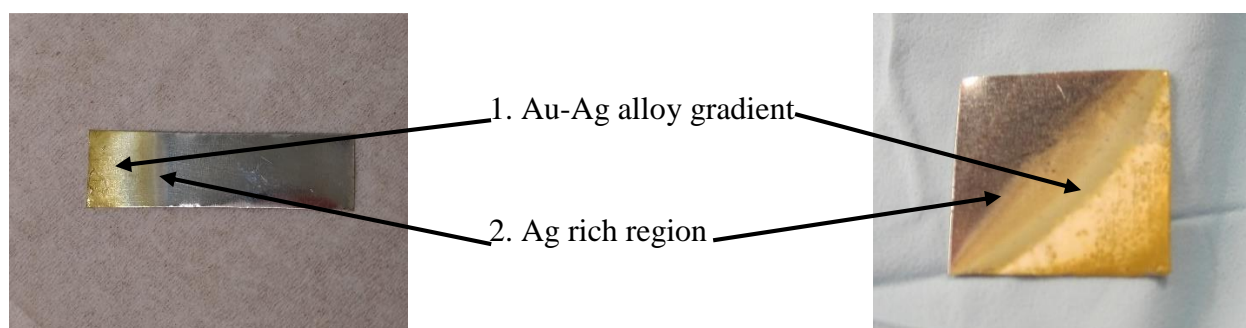


Figure 3.2: Picture of the Au-Ag alloy deposited on stainless steel. a) one dimensional b) two dimensional Au-Ag gradients.

We deposited Au-Ag alloy gradients on the cathodic pole of stainless steel bipolar electrodes by applying of 9.9 V between the driver electrodes for 1 minute. This driving voltage was determined by Ramaswamy et al from linear sweep voltammetry (LSV) using a stainless steel working

electrode dipped in the deposition solution.<sup>8</sup> The cathodic limit of Ag-Au alloy deposition was estimated theoretically -1.400 V, but open circuit potential of the stainless steel was -0.168 V vs Ag|AgCl (sat). They calculated a value of 2.464 V (twice the difference between the cathodic limit and the OCP) as the potential difference required between the two poles of the BPE in order to access the full range of Ag-Au alloy deposition potentials.

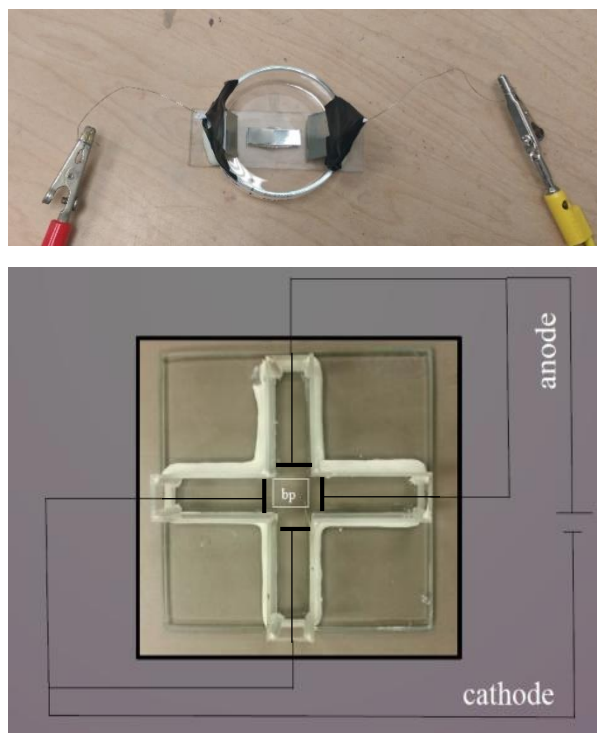


Figure 3.4: Picture of the home built one dimensional and two dimensional bipolar electrochemical cell.

An applied voltage of 9.9 V between the driver electrodes was required to achieve this potential difference. The anodic half-reaction corresponds to the generation of molecular oxygen from dissolved hydroxide ions. The electrodeposition of the alloys formed on the basis of the reduction potential of the  $\text{Ag}(\text{CN})_2^-$  and  $\text{Au}(\text{CN})_2^-$  species in solution.<sup>14-15</sup>



### 3.3.2 Scanning Electron Microscopy (SEM) and Energy Dispersive X-ray spectroscopy

**(EDX):** The surface morphology of the Au-Ag alloy films produced using BP-ED was studied using SEM. All characterization data discussed here was collected at 5 mm from the cathodic pole. The region of interest shown in figure 3.5 (one dimensional) is approximately 3  $\mu\text{m}$  in height and 3  $\mu\text{m}$  wide, corresponding to a surface area of ca. 9  $\mu\text{m}^2$ . This image is typical of what we observed across the alloy gradient and reveals a uniform coverage of electrodeposited material composed of a broad distribution of roughly spheroidal surface asperities with an average diameter of 100 nm (measured in the surface plane).

The region of interest shown in Figure 3.6 (two dimensional) is approximately 6.1  $\mu\text{m}$  in height and 6.8  $\mu\text{m}$  wide, corresponding to a surface area of ca. 41.5  $\mu\text{m}^2$ . This image is typical of what we observed across the alloy gradient and reveals a uniform coverage of electrodeposited material composed of a broad distribution of roughly spheroidal surface asperities with an average diameter of 100 nm (measured in the surface plane).

Atomic percentages of a two dimensional Ag-Au alloy gradient deposited onto stainless steel using bipolar electrodeposition was measured by EDX is showing in figure 3.7. Contour plot was made by measuring atomic% of Au in 3 points in every 1 mm along the length. From different color, we can see the gradients. From figure 3.7 we can see average maximum composition of two dimensional alloy is 50 -55 atomic% Au and 45-50 atomic% Ag.

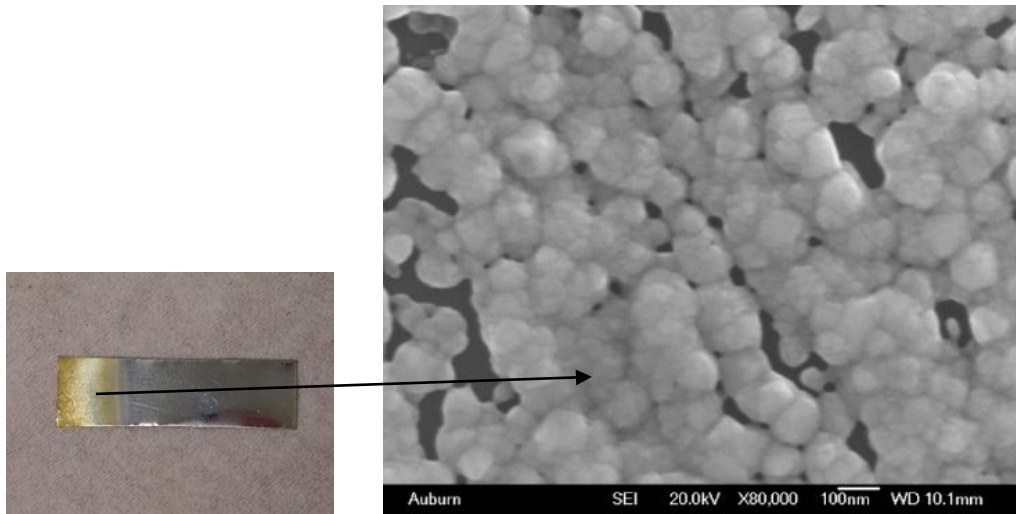


Figure 3.5: SEM image of the surface of a one dimensional Ag-Au alloy gradient deposited on stainless steel using bipolar electrodeposition.

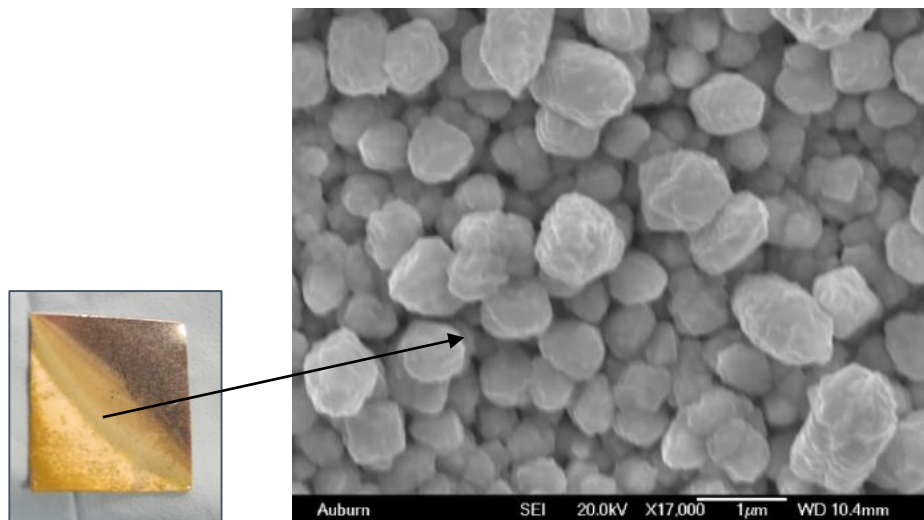


Figure 3.6: SEM image of the surface of a one dimensional Ag-Au alloy gradient deposited onto stainless steel using bipolar electrodeposition.

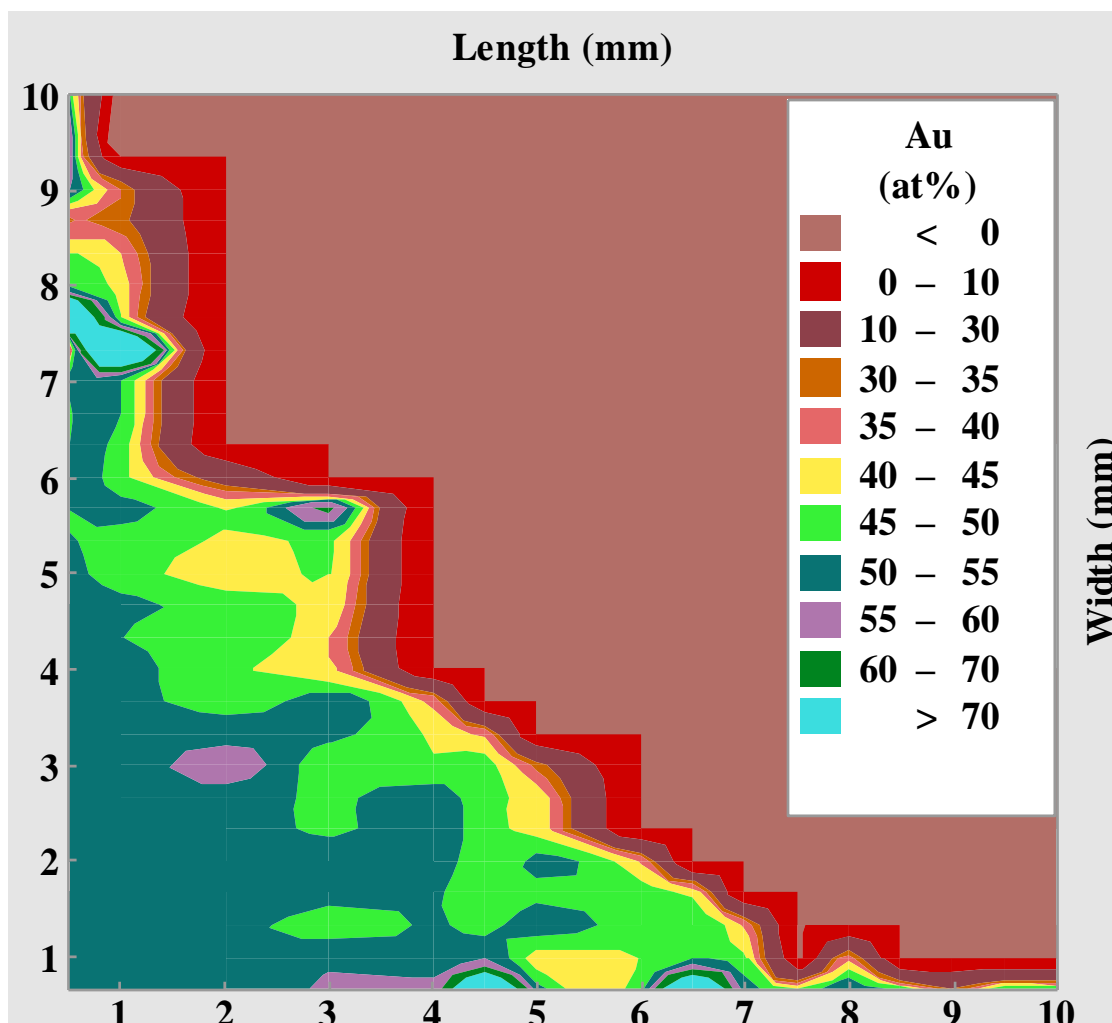


Figure 3.7: Contour plot of atomic percentages of Au in a two dimensional Ag-Au alloy gradient deposited onto stainless steel using bipolar electrodeposition.

### 3.3.3. Characterization of Ag-Au alloy gradient using SERS:

We characterize this two dimensional Au-Ag alloy gradient thin films using SERS spectroscopy to the gradients. Immediately after the BP-ED step, the samples were rinsed in pure water and dried in a stream of flowing  $N_2$ . Then a self-assembled monolayer (SAM) of 5 mM benzene thiol (ethanolic solution) was allowed to form on the alloy surface by immersed the chemically modified BPE in a 5 mM benzene thiol solution in ethanol for 15 h. A representative SERS spectrum of a benzene thiol SAM excited using 514.5 nm is shown in figure 3.8. The SERS peak frequencies

and relative intensities are in excellent agreement with previously published SERS spectra of benzene thiol.<sup>16</sup> All SERS bands for benzene thiol is listed in table 3.1.

Functional Group	Region (cm <sup>-1</sup> )
$\nu(\text{C-C-C})$ aromatic ring chain	996
$\nu(\text{C-S})$ aromatic	1072
$\nu(\text{C-C-C})$ aromatic ring chain	1573
$\nu(=\text{C-H})$	3059
$\nu(\text{O-H})$	3140

Table 3.1: SERS assignments of benzene thiol.

A confocal Raman microscope was used to obtain surface enhanced spectra at alloy area (SEM image also in same area). The excitation wavelengths used was 514.5 nm. Here only showing the 514.5 nm (figure 3.8). Figure 3.8 showed the integrated area of the 1574 cm<sup>-1</sup> benzene thiol SERS band plotted as a function of the alloy composition. The integrated intensity of the 1574 cm<sup>-1</sup> benzene thiol SERS band is assigned as the a<sub>1</sub> symmetric  $\nu(\text{C-C-C})$  band.<sup>16</sup> The rise in SERS intensity depends on the composition of alloy gradient. It reflects the electromagnetic enhancement of benzene thiol. Raman scattering depends on the optical extinction of the alloy substrate.<sup>8</sup>

Confocal Raman microscope was used to obtain enhanced Raman spectra at several points on two dimensional bipolar electrode using 514.5 nm excitation wavelengths. The integrated intensity of the 1574 cm<sup>-1</sup> benzene thiol SERS band (assigned as the a<sub>1</sub> symmetric  $\nu(\text{C-C-C})$  band)<sup>16</sup> is plotted as a function of the alloy composition.

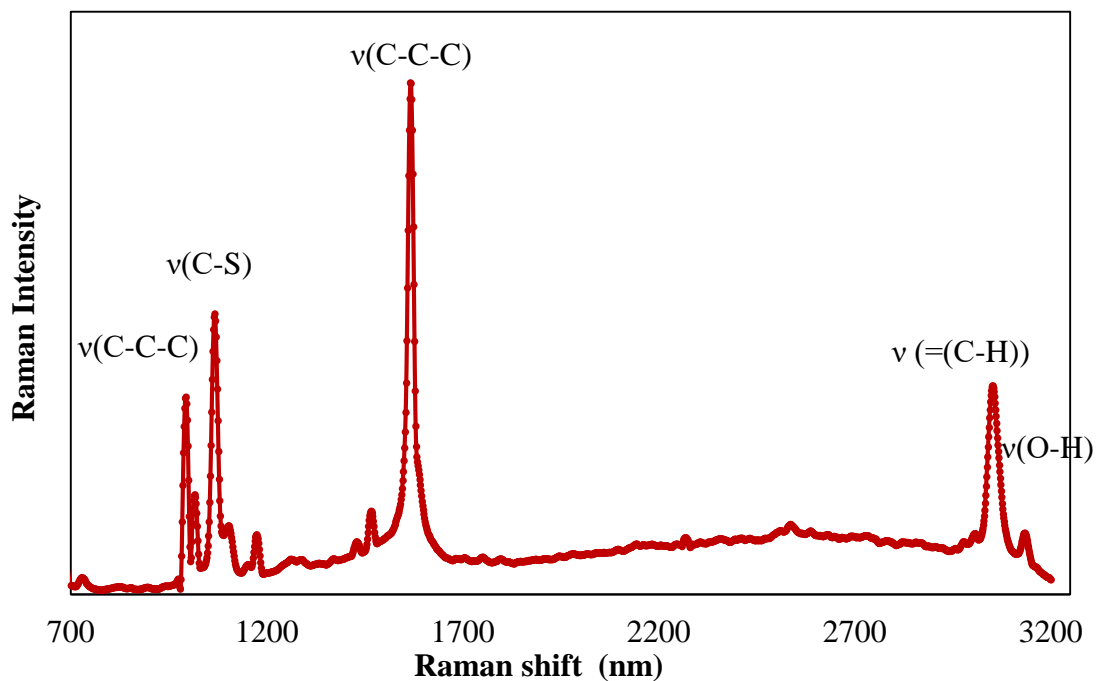


Figure 3.8: SERS spectrum of a benzene thiol SAM adsorbed on a two dimensional Ag-Au alloy film excited using 514.5 nm radiation

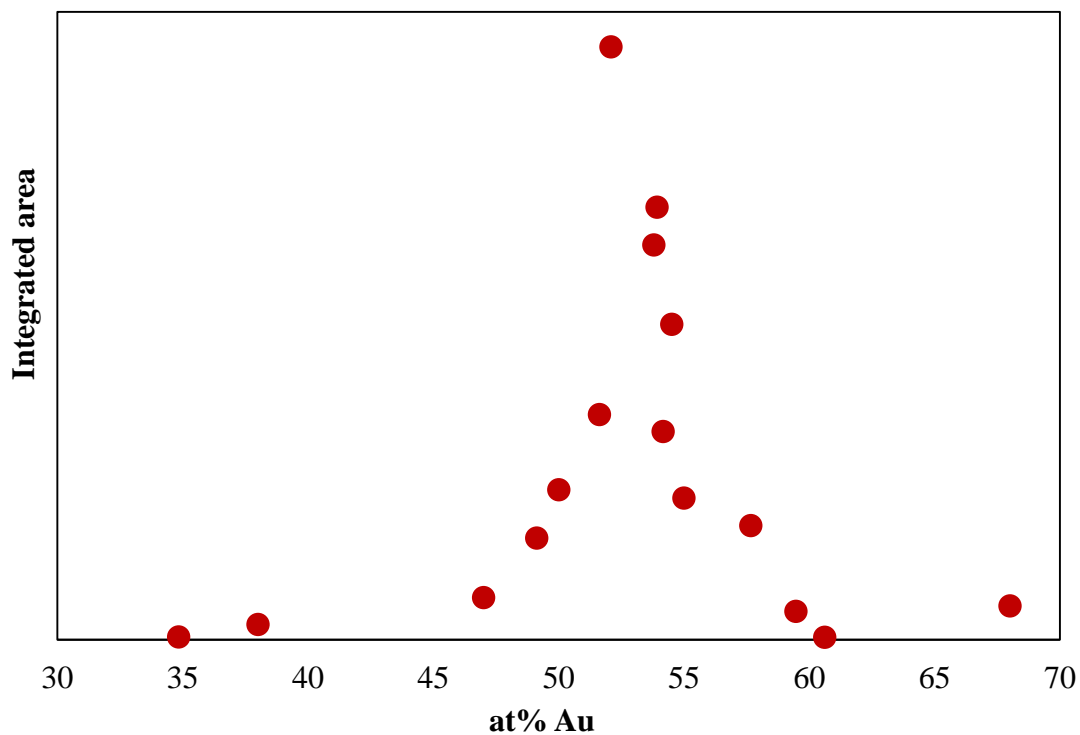


Figure 3.9: Integrated area under  $1574\text{ cm}^{-1}$  peak of benzene thiol SAM adsorbed on a two dimensional Ag-Au alloy gradient deposited onto stainless steel using bipolar electrodeposition.

Optical extinction of Ag-Au alloy gradient increase with the atomic percentage of silver. The data showed in Figure 3.9 prove an optimum SERS enhancement for alloy composition of about 48% Ag by SERS excited using 514.5 nm radiation. The presence of an optimal alloy composition for SERS excited using 514.5 nm light is probably based on the optical properties of Ag-Au alloy nanoparticles, for which the visible local surface plasmon resonance (LSPR) is well-known to blue shift with increasing Ag atomic percentage.<sup>7</sup> As bipolar electrodeposition method implies the formation of a potential gradient along the electrode, the metal deposition rate and, hence and composition and size are always changing along the length of the bipolar electrode. By changing the distance between the driver electrode one can formed gradients with smaller sized nanoparticles.

### **3.4 Conclusions:**

Electrochemically induced metal deposition is a relatively easy technique for the controlled assembly of metal gradients. We have shown here that bipolar electrochemistry is a useful tool for the deposition of one and two dimensional solid-state chemical compositions (Au-Ag alloy) gradients. These alloy gradients can be screened using various conventional surface analysis methods. Self-assembled monolayers were formed on top of the substrates pre-modified with gold and silver alloy gradients. This surface was screened by Surface enhanced raman spectroscopy and energy dispersive X-ray spectroscopy. The two dimensional Au-Ag alloy gradient screened by using SERS displayed an optimum composition of 50 atomic% Au/ 50 atomic% Ag with 514.5 nm excitation laser. By controlling the of Au-Ag alloy compositional gradient can be used several analytical applications such as catalysis, medical diagnostics, drug discovery, and chemical progress. The ability to create substrates with gradients of alloy is highly beneficial for sensor screening applications.

References:

1. Chen, G.; *Separation and Purification Technology*. **2004**,38, 11–41.
2. Stein, A.; Schroden, R. C. *Curr. Opin. Solid State Mater. Sci.* **2001**, 5, 553–564.
3. Roberts, M.; Johns, P.; Owen, J.; Brandell, D.; Edstrom, K.; Enany, G.; Guery, C.; Golodnitsky, D.; Lacey, M.; Lecoeur, C.; Mazor, H.; Peled, E.; Perre, E.; Shaijumon, M.; Simon, P and Taberna, P. *Journal of Materials Chemistry*. **2011**, 21, 9876.
4. Dover, R. B.; Schneemeyer, L. F.; Fleming, R. M. *Nature*. **1998**. 392, 162.
5. Genzer, J.; Fischer, D. A.; Efimenko, K.; *App. Phys. Letter*. **2003**. 82(2), 266.
6. Julthongpiput, D.; Faselka, M.; Zhang, W.; Nguyen, T.; Amis, J. *Nano Lett.* **2005**. 5(8), 1535.
7. Ramaswamy, R.; Shannon. *Langmuir* **2011**, 27(3), 878.
8. Ramakrishnan, S.; Shannon, C. *Langmuir* **2010**, 26(7), 4602–4606
9. Dorri, N.; Shahbazi, P.; Kiani, A. *Langmuir* **2014**, 30, 1376–1382
10. Loget, G.; So, S.; Hahn, R.; and Schmuki, P.; *J. Mater. Chem. A*, **2014**, 2, 17740–17745
11. Kelf, T. A.; Sugawara, Y.; Cole, R. M.; Baumberg, J. J.; Abdelsalam, M. E.; Cintra, S.; Mahajan, S.; Russell, A. E.; Bartlett, P. N. *Phys. Rev.B*. **2006**, 74,1– 12.
12. Fosdick, S. E.; Crooks, J. A.; Chang, B. Y.; Crooks, R. M. *J. Am. Chem. Soc.*, **2010**, 132 (27), 9226–9227.
13. Tisserant, G.; Fattah, Z.; Ayela, C.; Roche, J.; Plano, B.; Zigah, D.; Goudeau, B.; Kuhn, A.; Bouffier, L.; *Electrochimica Acta*. **2015**.179,276–281
14. Jose, M.; Munoz, L.; Aguado, J.; Grieken, R.; Maruga, J.; *App. Cat. B: Environmental*. **2008**. 86,53-62.
15. Kirk, D. W.; Foulkes, F. R.; Graydon, W. F.; *J. Electrochem. Soc.* **1978**. 125(9),1436-1443

16. Abdelsalam, M. E.; Bartlett, P. N.; Baumberg, J. J.; Cintra, S; Kelf, T. A.; Russell, A. E.  
*Electrochem. Commun.* **2005**, *7*, 740–744.

## **Chapter Four**

### **Summary Of Thesis**

In this Thesis we reported the deposition of metal gradients by bipolar electrochemistry. Compositional gradients can be readily obtained from reference solutions. The use of bipolar electrodeposition for creating size gradients in gold and silver nanoparticles tied to surfaces was also explored. Substrates were pre-modified with an Au and Ag precursors containing solution to obtain gradients in particle size by electrodeposition. The capability to create substrates with bimetallic alloy gradients is highly beneficial for sensor screening or materials synthesis applications.

A chemical reaction between molecules requires a definite amount of energy to take place. A catalyst can lower this activation energy, so a lesser amount of energy is necessary for the reaction, consequential in a greener and more ecological process. Heterogeneous catalysts are usually made up of small metal nanoparticles, surrounded in the larger structure of a porous support material. The surface of the metal nanoparticles is active catalytic material, where reactions take place. Preferably, to monitor a reaction over a single catalytic nanoparticle, to completely understand the dynamics involved in a reaction for expansion of even more efficient catalysts. Imaging at such a high resolution typically requires high-energy sources, and yields no molecular information. On the other hand, optical spectroscopy techniques are well-capable of following reactions occurring over catalysts, and they are especially suitable for monitoring the state of molecules during a reaction. Due to diffraction limitations, however, these techniques are limited in spatial resolution to hundreds of nanometers. Raman spectroscopy is one of these techniques,

and is selective, highly informative and easily incorporated under catalytic working conditions. This makes it worthwhile to tackle the last challenges in Raman spectroscopy that hamper analysis on the scale of single nanoparticles - being the spatial resolution, the low scattering intensity and interference by fluorescence.

In this Thesis it is displayed that the key lies in the use of the nano photonic properties of metal nanoparticles. At specific excitation wavelengths, electrons in metal nanoparticles can be excited to a higher energy level, called the surface plasmon resonance. The local electromagnetic field linked to this resonance can be extremely intense at the close contact between two nanoparticles, and when the resonances of the single particles combine, they form a gap-mode plasmon. This near-field is localized within a nano-scale volume and is used to create a nanometer-range spatial resolution for Raman spectroscopy. In gold or silver nanoparticles, this high intensity near-field also creates a large enhancement of the Raman scattering for molecules present within this field. This effect is called surface-enhanced Raman scattering (SERS), and can be used to overcome the low scattering intensity of normal Raman spectroscopy. Lastly, the SERS-effect inherently minimizes the interference by fluorescence, deal with the final challenge for Raman spectroscopy as a nano-scale analytic tool for in-situ reaction monitoring. Here, SERS is optimized for the investigation of heterogeneous catalytic reactions on a nano-scale.

As a model reaction, the electrochemical catalytic reduction of 4-nitrothiophenol (4-NTP) is selected. The reduction of nitro-aromatics is a class of well-studied reactions in literature. For application with SERS, 4-NTP is the most ideal reactant. Its thiol-functionality confirms the self-assembly onto gold and silver surfaces. The photo-catalytic reduction of 4-NTP is easily prompted via the combination of green laser excitation and a silver SERS substrate, but is influenced by many parameters. The kinetics for this reduction of 4-NTP are analyzed via monitoring over a

different catalytic active sites. The reduction is performed within a self-assembled monolayer. It also proves that 4,4-dimercaptoazobenzene is the reaction intermediate product in this reaction. But it is the final product in the photo-catalytic reduction of 4-NTP.

From the work presented in this thesis, covering a range of electrochemical processes, we can conclude some general characteristics of bipolar electrochemical experiments. Mainly, this approach was found to be highly sensitive to parameters such as electrolyte surface of the substrate, alloy composition and the electrochemistry of the substrate, in strong agreement with the above-mentioned literature. The different concepts investigated here demonstrate the flexibility of the bipolar method. In particular, the two-dimensional gradient concepts are fascinating directions for future research into high-throughput materials and sensor screening techniques.